A NOVEL THREE-FINGER IPMC GRIPPER FOR MICROSCALE APPLICATIONS

A Dissertation

by

KWAN SOO YUN

Submitted to the Office of Graduate Studies of
Texas A&M University
in partial fulfillment of the requirements for the degree of

DOCTOR OF PHILOSOPHY

May 2006

Major Subject: Mechanical Engineering

A NOVEL THREE-FINGER IPMC GRIPPER FOR MICROSCALE APPLICATIONS

A Dissertation

by

KWAN SOO YUN

Submitted to the Office of Graduate Studies of
Texas A&M University
in partial fulfillment of the requirements for the degree of

DOCTOR OF PHILOSOPHY

Approved by:

Chair of Committee, Won-jong Kim
Committee Members, Reza Langari
James G. Boyd
Wayne N. P. Hung
Head of Department, Dennis O'Neal

May 2006

Major Subject: Mechanical Engineering

ABSTRACT

A Novel Three-Finger IPMC Gripper for Microscale Applications.

(May 2006)

Kwan Soo Yun,

B.S., A-jou University, Suwon, Korea;

M.S., Texas A&M University

Chair of Advisory Committee: Dr. Won-jong Kim

Smart materials have been widely used for control actuation. A robotic hand can be equipped with artificial tendons and sensors for the operation of its various joints mimicking human-hand motions. The motors in the robotic hand could be replaced with novel electroactive-polymer (EAP) actuators. In the three-finger gripper proposed in this paper, each finger can be actuated individually so that dexterous handling is possible, allowing precise manipulation.

In this dissertation, a microscale position-control system using a novel EAP is presented. A third-order model was developed based on the system identification of the EAP actuator with an AutoRegresive Moving Average with eXogenous input (ARMAX) method using a chirp signal input from 0.01 Hz to 1 Hz limited to ±7 V. With the developed plant model, a digital PID (proportional-integral-derivative) controller was designed with an integrator anti-windup scheme. Test results on macro (0.8-mm) and micro (50-μm) step responses of the EAP actuator are provided in this dissertation and its position tracking capability is demonstrated. The overshoot decreased from 79.7% to

37.1%, and the control effort decreased by 16.3%. The settling time decreased from 1.79 s to 1.61 s. The controller with the anti-windup scheme effectively reduced the degradation in the system performance due to actuator saturation. EAP microgrippers based on the control scheme presented in this paper will have significant applications including picking-and-placing micro-sized objects or as medical instruments.

To develop model-based control laws, we introduced an approximated linear model that represents the electromechanical behavior of the gripper fingers. Several chirp voltage signal inputs were applied to excite the IPMC (ionic polymer metal composite) fingers in the interesting frequency range of [0.01 Hz, 5 Hz] for 40 s at a sampling frequency of 250 Hz. The approximated linear Box-Jenkins (BJ) model was well matched with the model obtained using a stochastic power-spectral method. With feedback control, the large overshoot, rise time, and settling time associated with the inherent material properties were reduced. The motions of the IPMC fingers in the microgripper were coordinated to pick, move, and release a macro- or micro-part. The precise manipulation of this three-finger gripper was successfully demonstrated with experimental closed-loop responses.

To my parents, Young-gil Yun and Myoung-ja Lee,

my wife, Jeong-ok Kim,

and my daughter, Jenny Yun

ACKNOWLEDGMENTS

I would like to thank Dr. Won-jong Kim, my advisor, for invaluable advice as well as providing inspiration and motivation whenever it was desperately needed. The technical communication with him over the past 3 years was my great asset in all aspects of my research.

I wish to thank Drs. Reza Langari, James G. Boyd, and Wayne N. P. Hung for serving as my advisory committee members. I sincerely appreciate the time, advice, and support they provided me with during my doctoral study. The significant contributions of the committee members brought this dissertation to success.

I would like to thank Mr. Nikhil Bhat, a former student of Dr. Kim, for the initial design of the experimental set-up. Then I would like to give my special thanks to Drs. Kihwan Kim, Guangyoung Sun, and Murray Kerr. Dr. Kihwan Kim helped me a lot with the system identification and the control system design whenever necessary, and Dr. Guangyoung Sun helped me with general concepts of feedback control skills in our discussions. Dr. Murray Kerr gave me valuable suggestions on control-design and modeling issues. I would also like to thank Mr. Mike Walker of the mechanical engineering machine shop who much helped me in the fabrication of the parts for my experiments. I appreciate all my labmates for their providing a congenial atmosphere in the lab.

My special appreciation goes to Dr. Donald Leo and Mr. Matt Bennett of Virginia Polytechnic Institute and State University for providing with IPMC samples. Mr. Matt Bernett gave me the information of the IPMC samples and valuable discussions.

I am also grateful to Drs. Othon K. Rediniotis and Hyoung-yoll Jun of Department of Aerospace Engineering at Texas A&M University for providing the EAP samples.

Finally, I can never thank enough for my parents, Mr. Young-gil Yun and Mrs. Myoung-ja Lee for their endless love and encouragement. My wife, Jeong-ok Kim, always helps me a lot for her support and understanding as my soul mate.

TABLE OF CONTENTS

Page

CHAPTER Page

LIST OF TABLES

LIST OF FIGURES

FIGURE Page

FIGURE Page

FIGURE Page

FIGURE Page

FIGURE Page

CHAPTER I

INTRODUCTION

Ionic polymers are a recently discovered class of active materials. Their capabilities and limitations must be well understood and documented before they can be applied for a new generation of actuators and sensors. To facilitate their design process, simple but accurate models must also be developed. In this chapter, the development history, current trends' modeling and applications of ionic polymers are presented. Then, research goals and contributions and an overview of this dissertation are given.

1.1 History and Current Trends of Novel Ionic Polymers

Smart materials exhibit physical responses, such as mechanical deformation and heat generation in the presence of applied stimuli, such as electricity, heat, chemical reaction, pressure, and mechanical deformation. These responses can be used in converting the applied energy into a desired form. Ionic polymers are a subset of a class of smart materials known as electro-active polymers (EAPs), polymers that respond to electrical stimulus. The EAP is a class of materials composed of polymers, metals, and other elements that show unique properties: (1) This composite material produces a mechanical motion in response to applied electrical voltage. (2) Conversely, EAP can be used as a sensor by measuring the output voltage generated by imposed mechanical

---

This dissertation follows the style and format of *IEEE Transactions on Automatic Control*.

deformation. These properties can be useful in a variety of applications requiring actuation or sensing.

During the last decade, Sadeghipour *et al*., Shahinpoor *et al*., Oguru *et al*., and Tadokoro *et al*. investigated the bending characteristics of Ionic Polymer Metal Composite (IPMC) [1–4]. Bar-Cohen *et al.* characterized the electromechanical properties of IPMC [5]. An empirical control model by Kanno *et al.* was developed and optimized with curve-fit routines based on open-loop step responses with three stages, i.e., electrical, stress generation, and mechanical stages [6–8]. Feedback compensators were designed using a similar model in a cantilever configuration to study its open-loop and closed-loop behaviors [9–10].

Bhat and Kim [10–11] identified the position and the force modeling of IPMC using an empirical control model suggested by Kanno *et al.* [6]. These models were optimized using curve-fit routines on the open-loop step responses. Feedback compensators were then designed using these models, and the ionic polymer actuator was used in a cantilever configuration to study open-loop and closed-loop feedback control. Furthermore, Bhat and Kim [9] demonstrated the novelty of a hybrid control scheme switching between position and force control schemes using ionic polymer actuator. This work was supposed to use in application to a robotic micro-gripper.

Many ionic polymers including IPMC or EAP can be also classified as viscoelastic materials, so researchers adopted the Golla-Hughes-McTavish (GHM) method [12]. It enabled the modeling of linear viscoelastic materials using Young's modulus as a function of frequency [12–13]. Alvarez and Shahinpoor showed the static and dynamic deflection with the nonlinear equation for large-angle deflections in an

elastic cantilever beam by simulation [14]. Prevailing approaches to controller design presume that an applicable model for the plant to be controlled is available. Although most real-world dynamic systems are nonlinear, they could usually be approximated in their normal ranges of operation, and relatively simple, lumped-parameter input-output linearized models can often be used. Some EAP materials are now commercially available [15], but their material properties are still under investigation with analytical and numerical approaches.

The step response, as a means for modeling, of EAP was observed to be inconsistent and non-repeatable because its stiffness is a function of the hydration level of the polymer, which might change with respect to time while in continual use. Damping of the ionic polymer actuator in air is much lower than that in water. Feedback control is necessary to decrease the response time of an ionic-polymer actuator to a step change in the applied electric field and to reduce overshoot. The position control of the EAP was investigated by using a linear quadratic regulator (LQR) [12], a PID controller with impedance control [16], and a lead-lag compensator [9–10]. Advanced control algorithms must be developed for EAP or IPMC to compensate for their highly nonlinear and non-repeatable open-loop behaviors.

1.2 Modeling and Applications of Ionic Polymers

Microgrippers are essential tools in industrial processes. An integrated microgripper system, which can be easily implemented with any platforms operated with objects having a wide range of sizes and shapes, will have a great impact on micro-optics manipulation, micro-electro-mechanical systems (MEMS), fiber-optics assembly,

biomedical manipulation, and semiconductor manufacturing. The success of microgrippers heavily depends on the reliability and durability of the actuator and the sensor.

Researchers in the field of biomimetics anticipate that ionic-polymer materials may be applied to many applications of theirs [17]. Although applications of IPMC are still in early stages, they will have the versatility to mimic insect, animal, or even human systems (e.g. human artificial muscles) with catheter-steering elements, miniature manipulators, dust-wipers, miniature robotic arms, grippers, electro-rheological fluids for active damping, miniature boxes, micro-robots, and surgical tools and robots that have the ability to assemble other micro-devices [17–18].

This research focuses on the design of a miniature displacement mechanism and the electromechanical characteristics of this IPMC actuator. Strips of EAP composites can bend and flap dramatically when an electric voltage is applied. In this sense they are large motion actuators; they can move and exert force. Conversely, when a strip is bent, a voltage is produced across its thickness, allowing the strip to behave like a sensor that can determine a given level of force and motion. These are EAPs that bend in response to an electrical activation as a result of the mobility of cations in the polymer network. Generally, two types of base polymers are employed to form IPMCs. These are Nafion® (perfluorosulphonate manufactured by DuPont) and Flemion® (perfluorocaboxylate manufactured by Asahi Glass, Japan) [17]. IPMC requires relatively low voltages (1–10 V) to generate bending responses at low frequencies below 5 Hz.

Since micromechanical systems like micro-optical devices, microfluidic components or other hybrid microsystems became ever more complex, developing an

enabling micro-assembly technique is of great importance. The production of microsystems requires a tighter control due to the small size of the microparts to be mounted in hybrid microsystems (e.g. microlenses, optical fiber, and microtubes). It also needs very high accuracy in the assembly processes, which cannot be achieved with conventional assembly equipment. Therefore the demand of micro-assembling tools as high-precision robots and microgrippers has increased dramatically.

Ionic polymer actuators were modeled in various ways by taking relevant physical phenomena into consideration. Electromechanical modeling was performed with an Euler-Bernoulli beam theory. The governing equation used in [18–19] assumed small bending deflection. Actual bending deflections can be large, which is contradictory to this assumption. The material properties of IPMC were not fully considered in [20] since the measurement of the deflection of the activated IPMC strip is related to its Young's modulus because the Young's modulus of IPMC is a function of frequency and temperature [21]. Alvarez and Shahinpoor [14] approached the static deflection of the nonlinear equation with a hypothetical deflection under a constant moment, not a variable moment. Nemat-Nasser and Li [22] developed a model accounting for the coupled ion transport, electric field, and elastic deformation to predict the response of the Nafion-based IPMC.

The Kanno-Tadokoro model contains the electrical, stress generation, and mechanical stages [23]. For the electrical model, the characteristics is approximated by a series connection of RC circuits based on an experimental curve. In the stress generation stage, the internal stress that plays a key role in bending was represented by a similar manner of piezoelectric elements. Bao *et al*. [24] derived macroscopic models for the

electric input and the electromechanical actuation of IPMC. The models that relate the electric input and the mechanical output are required for the material characterization, i.e. to define and extract the material parameters in order to establish mathematical groundwork for actuator design. A lumped RC model for the input current/voltage response of IPMC and a distributed RC model were presented.

In a linear-actuator aspect, Jung and Ryew [25] addressed the bending motion to a linear motion of IPMC using the analogy of a centipede. This model still requires to improve the efficiency of the effective force and controllable velocity. For a feedback-control approach, Mallavarapu *et al*. [26] derived an empirical model of IPMC to manipulate the pole-zero locations in the frequency domain and in the state space. LQR control was used to optimize the settling time and lower the control input [27]. On the other hand, Bhat and Kim [11] identified a force model experimentally, improved the performance in the settling time, and reduced the overshoot using a lead-lag compensator. Open-loop step responses of the IPMC polymer were observed to be non-repeatable as the stiffness is a function of the hydration of the polymer, which might change with respect to time during continual use.

The enhancement of the actuation capability of IPMC materials is studied in this dissertation on a fundamental level using black-box-model approaches. The large strain response of IPMC to electrical simulation is nonlinear and still requires adequate analytical methods for the design and control of related devices based on the material. The origin of the electro-activity in IPMC materials must be understood better to improve their performance and to offer effective design methods to enhance their robustness. The development of a dynamic model of a single-degree-of-freedom mechanism by system

identification is necessary to design the control system to manipulate IPMC strips in a three-finger gripper simultaneously.

1.3 Research Goals and Contributions

The primary goal of this work is to characterize and model the behavior of ionic polymers at both macroscopic and microscopic levels. Another main goal is to develop and implement a new generation of precision position and force control methodologies with a smart three-finger gripper system that would enhance manipulation capabilities and add intelligence to existing systems with regard to design, performance, and cost. This research is aimed at achieving these goals by accomplishing the following tasks:

1. To compensate for the highly nonlinear behavior of the IPMC to improve the actuator and sensor performance by increasing its dynamic range and making it less sensitive to measurement noise.
2. To develop multivariable schemes and implement them in real-time applications.
3. To operate the three-finger gripper to satisfy the control requirements such as proper functioning, repeatability, and reliability.

The main contribution of this dissertation is the design and realization of a three-finger gripper with very compact mechanical structures and its extensive testing. I designed and fabricated the parts for the gripper in the mechanical engineering machine shop at Texas A&M University. The precision assembly was performed using the fixtures that I designed and built. I performed extensive precision-position-control tests and force-control tests with the real-time codes I developed.

To enhance the transient performance of the IPMC actuator when the control input was saturated, the anti-windup control scheme was developed to avoid of the saturation effect. The linear approximation of inherently nonlinear IPMC dynamics was suitable for the microscale gripping application since the control voltage was below the saturation limit. In the IPMC actuator case where simulations and experiments in this research overlap the scope of previously published results [9–11], the new results are still useful for the sake of comparison.

Another contribution of this work is that the system identifications both the position and the force have been predicted by the model and demonstrated experimentally. In addition, the validated model to predict the IPMC actuator's dynamic behavior is compared with the experimental data. The model presented in this dissertation is a simple, linear dynamic model that represents the characteristics of the IPMC actuator with a single, frequency-dependent term. This document also describes how the highly nonlinear behavior can be treated with an approximated linear model with applying specific chirp signal inputs. The model was used to determine the feasibility of the three-finger gripper from an electromechanical standpoint. After the IPMC strip was designed, the model of the IPMC strip was utilized to predict open-loop and closed-loop performances in both position and force control for the purpose of manipulating the IPMC actuator effectively in 'pick-and-place' operations. The precise manipulation of this three-finger gripper was successfully demonstrated with experimental closed-loop responses in both macroscale and microscale. This three-finger gripper is an excellent candidate for macro- and micro-manipulation in the future technology.

1.4 Overview of Dissertation

This dissertation contains seven chapters. Chapter I describes the importance of precision position and force control of the three-finger gripper. It presents a literature review of published research work with a brief description of EAP and IPMC.

Chapter II presents the working principle of an IPMC actuator and the advantages of using the EAP or IPMC actuator comparing with other smart materials and its practical applications.

Chapter III presents the experimental setup including both position and force sensors. The design of the three-finger gripper is also presented.

Chapter IV describes the system identification for modeling and the dynamic behavior of the EAP or IPMC actuator with open-loop force and position responses. The model parameters are identified experimentally. To accurately model the system, system-identification methods for properly selected model structures are applied. In addition, the identified model is validated by comparing predicted and experimental responses.

Chapter V presents the design of the position and the force controller in simulation and the closed-loop experimental results with several modified controllers for the IPMC actuator. Precision position control is demonstrated by implementing a digital PID controller with an integrator anti-windup scheme that reduces the performance degradation due to actuator saturation. The design of the linear estimator observer controller using LQR method is explained. The difference between the simulations and experimental results is explained.

Chapter VI provides the controlled precision macro- and micro-scale position and force control. Simulated and experimental results obtained with the closed-loop position

controller implemented on the IPMC three-finger gripper are presented. The feedback control algorithm using a modified PID controller was used for the force control in both micro- and macro-scale. The grabbing the object with three-finger gripper is demonstrated.

Lastly, Chapter VII summarizes the conclusions of this research and the suggestions for future work.

CHAPTER II

WORKING PRINCIPLE AND PRACTICAL APPLICATIONS OF IPMC

This chapter describes the working principle of an IPMC actuator. Comparison in performance parameters with other smart materials shows its advantages and disadvantages. Also practical applications of IPMC are presented.

2.1 Working Principle of an IPMC Actuator

IPMC is made of a perfluorinated membrane (i.e., all of the hydrogen atoms attached to carbon atoms are replaced with fluorine atoms) with noble metal plating (typically gold or platinum) for electrodes [28], then cut to be of the desired geometry. The IPMC samples we used in this research have two metal coatings on the Nafion membrane. The first metal coating consists of many small platinum particles dispersed inside the surface of the membrane within the polymer. The depth of penetration is usually 10–20 μm. The second metal coating is gold deposited by electroplating. This coating is intended to enhance the surface conductivity of the IPMC.

The chemical structure of Nafion 117 is shown in Fig. 2-1. The particular permeability arises from the charged sulfonic acid groups (SO_3^-) that are tied up the sidechains of the polymer backbone. When the polymer is hydrated, the cations (positively charged ions) associated with the SO_3^- groups become mobile, allowing the polymer to conduct cations.

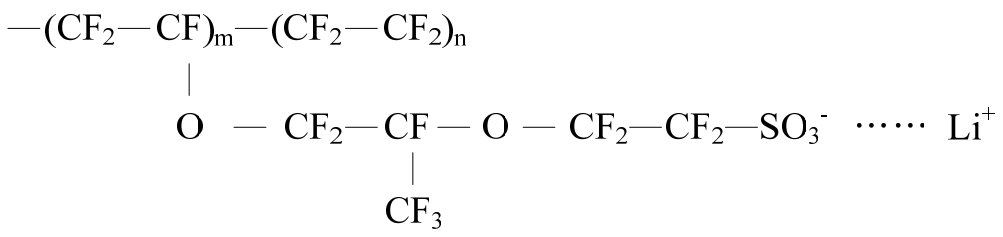

Fig. 2-1. Chemical structure of Nafion [29]. Note that the counter ion can be replaced by other mobile cations.

Ionic polymers are typically either Flemion (a perfluorocarboxylate, Asahi Glass, Japan) or Nafion (a perfluorosulfonatem, Dupont, USA) that swell in water due to their ionic and hydrophilic nature. Anions (negatively charged ions) are located on the polymer membrane while cations are present and freely moving in the fluid. A photograph of the IPMC membrane is shown in Fig. 2-2.

Fig. 2-2. Platinum- and gold-plated Nafion 117 membrane (Lithium counter ion).

The thickness of Nafion 117 is approximately 0.18 mm. The IPMC consists of the composite by plating Nafion 117 on both sides with an approximately 2 μm-thick film of gold or platinum by the chemical plating method. After roughening the surface of Nafion 117 by mild sand blast, exchange of hydrogen ions and platinum cations took place, immersing the film in complex ions of platinum ammine [30]. The IPMC process is summarized in Table 2-1.

Table 2-1. IPMC manufacturing process.

Stage	Procedure
1. Nafion roughening	Roughen polymer to ensure platinum adheres to polymer surface.
2. Primary plating	Electrochemically deposit a thin layer of platinum on the Nafion surface.
3. Secondary plating	Deposit a thicker layer of platinum on top of the primary plating.

An illustration of a typical IPMC cross-section is shown in Fig. 2-3. The metallic layers act as flexible electrodes, generating an electric field across the IPMC's thickness for actuation or collecting charges for sensing. An ionic polymer, due to its molecular structure, is permeable exclusively to cations or to anions (negatively charged ions). Dupont's Nafion, the most common base material for an ionic polymer actuator, is permeable to cations and water molecular.

When an electric field is applied to the IPMC, the cations diffuse toward the negative electrode, which causes the composite polymer to deform [31] as depicted in Fig. 2-4. On the other hand, when a mechanical load is applied to the IPMC, a few millivolts are generated across the electrodes [31].

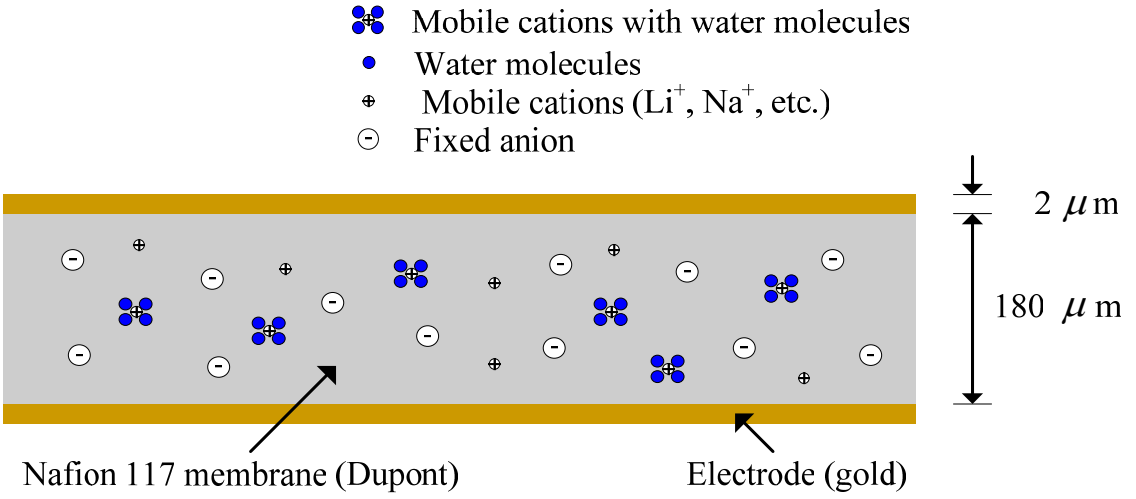

Fig. 2-3. Cross-section of an ionic polymer metal composite.

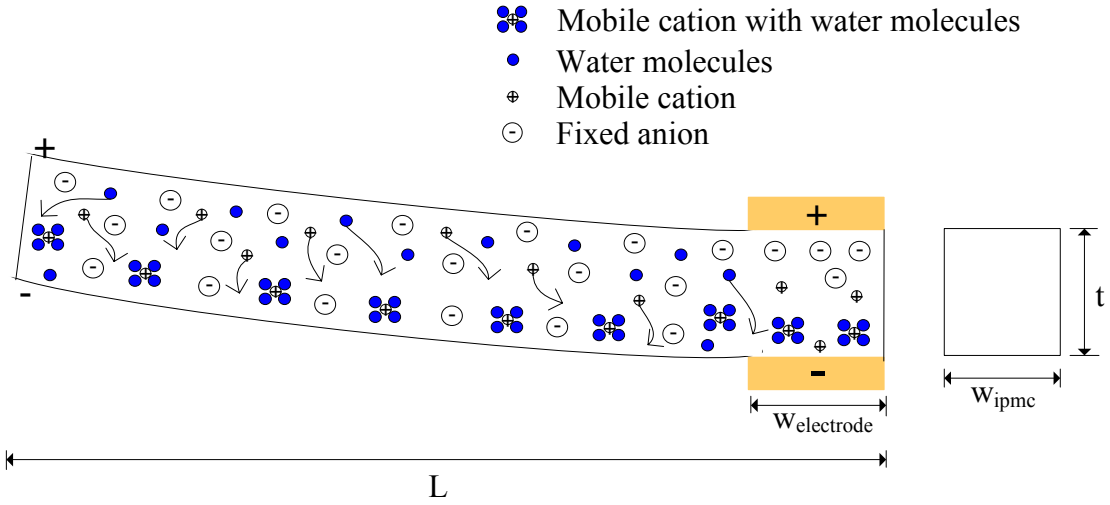

Fig. 2-4. Redistribution of charges in an ionic polymer due to an imposed electric field.

Typically, the strip of the perfluorinated-ionic-polymer membrane bends toward the anode in case of cation-exchange membranes under the influence of an electric potential. The appearance of water on the surface of the expansion side and the disappearance of water on the surface of the contraction side are common. This

electrophoresis-like internal ion-water movement is responsible for creating effective deformation for actuation. Water leakage through the porous platinum electrode reduces the electromechanical-conversion efficiency [32]. This can support the phenomenon of generating the water on the surface of the IPMC strip stuck to the negative electrode.

Because of its ion selectivity, as well as other desirable material properties, Nafion is used in application such as a fuel cell, i.e., an electrochemical device converting chemical energy to electric energy as shown in Fig. 2-5.

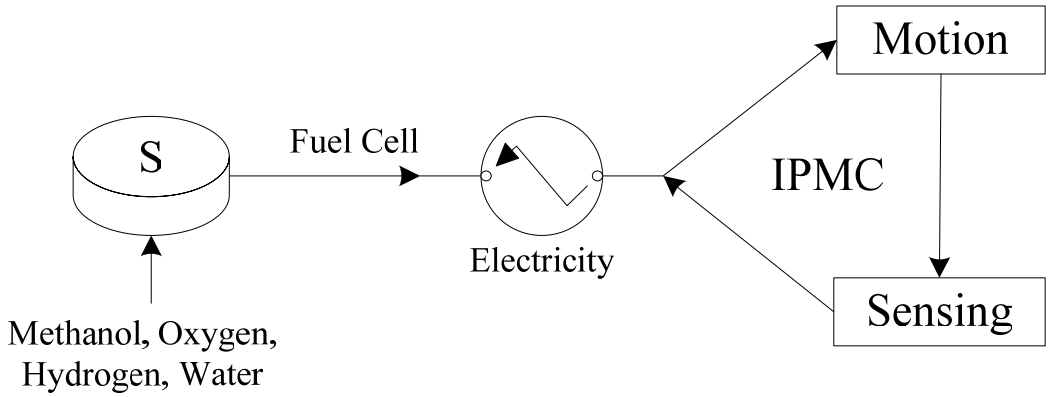

(a)

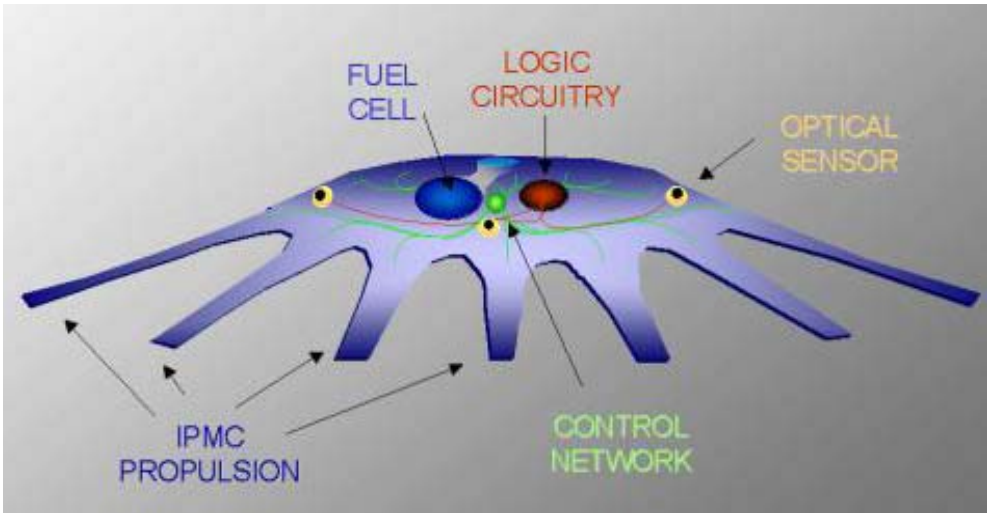

(b)

Fig. 2-5. Biomimetic integrated system: (a) schematic diagram of biomemetic system, (b) a prototype biomemetic system [33].

2.2 Various Smart-Material Properties

Structures and materials that sense external stimuli and respond accordingly in real time are called as smart materials. The actuator technologies using smart materials under development include shape memory alloys, piezoelectrics, magnetostrictive actuators, electroactive polymers, and electrostatic actuators. It is essential to compare the performance of these artificial actuators with each other before making a final decision of our design. Table 2-2 compares performance parameters of EAP with other actuators. As seen in Tables 2-2 and 2-3, IPMC is not the best candidate in any single measure of performance aspect. However, its overall performance is good enough that it can be used comparatively in energy-efficient actuator as a lightweight, low-cost device with high displacement and high power output relative to well-established smart materials such as piezoelectrics, shape memory alloys, etc. Other important considerations include the repeatability and accuracy such that how well the output of the actuator can be controlled and the reliability and endurance such that how long the actuator will last.

2.3 Ionic EAP and Its Benefits

Generally, EAPs can be classified into two major categories based on their activation mechanism including ionic and electronic. The electric polymers (electrostrictive, electrostatic, piezoelectric, and ferroelectric) can be made to hold the induced displacement under activation of a DC voltage, allowing them to be considered for robotic applications. These materials also have a greater mechanical energy density and can be operated in air. However, they require a high activation field (> 100 V/μm) [34]. As contrasted, ionic EAP materials (gel, polymer-metal composites, conductive

Table 2-2. Comparison between EAPs, natural muscle and other actuation technologies [35–36].

Actuator type	Maximum Strain (%)	Maximum Pressure (MPa)	Specific Elastic Energy Density (J/g)	Maximum Efficiency (%)	Relative Speed (full cycle)
Carbon Nanotube	> 2.5	> 1.0	> 0.013	< 10?	Medium
Liquid Crystal Elastomer	> 35	> 0.3	> 0.10	< 10?	Slow
IPMC (Nafion)	10	1.0	0.025	< 10?	Medium
Conducting Polymer (Polyaniline)	10	450	23	< 10?	Slow
Electrostatic Devices (Integrated Force Array)	50	0.03	0.0015	> 90	Fast
Electromagnetic (Voice Coil)	50	0.01	0.003	> 90	Fast
Piezoelectric Ceramic (PZT) Single Crystal (PZN-PT) Polymer (PVDF)	 0.2 1.7 0.1	 110 131 4.8	 0.013 0.13 0.0013	 90 90 ~ 80 est.	 Fast Fast Fast
Shape Memory Alloy (TiNi)	> 5	> 200	> 15	< 10	Slow
Magnetostrictive (Terfenol-D)	0.2	70	0.0027	60	Fast
Natural Muscle Peaks in nature Human Skeletal	 100 > 40	 0.80 0.35	 0.04 0.07	 - -	 Slow-Fast Medium

polymers, and carbon nanotubes) in Table 2-4 require drive voltages as low as 1–2 V. However, there is a need to maintain their wetness, and except for conductive polymers it is difficult to keep DC-induced displacements. The induced displacement of both electronic and ionic EAPs can be geometrically designed to bend, stretch, or contract.

Table 2-3. Actuator technology synopsis [37].

Actuator type	Description
Carbon Nanotube	High stress (> 10 MPa), very small strain (0.2%), low driving voltage (~ 2 V), inefficient unilateral actuation expensive.
Liquid Crystal Elastomer	Low-moderate stress (0.01–0.45 MPa), moderate-high strains (2–45%, depending on whether thermal or field induced strain), moderate-high efficiency difficult to control (creep), new material high driving voltages, slow.
IPMC (Nafion)	Large strain, low driving voltage (< 10 V), unilateral actuation low efficiency.
Conducting Polymer (Polyaniline)	High stress (5–34 MPa), low strain (2%), high stiffness, low driving voltage (~ 2 V), high work density (100 kJ/m³), slow bilateral actuation, low efficiency.
Electromagnetic (Voice Coil)	Low peak stress (0.05–0.1 MPa), large strain (50%), high power density (200 W/kg), efficiency varies from high (~ 90%) at high speeds and short strokes to low (~ 5%) at low speeds and high stroke lengths. Fast, high compliance, form factor compatible with human-form design. Produces smooth, backlash-free, quiet motion. Low material overhead, few moving parts; robust to overloading, bi-directional (push-pull) actuation. High force applications require mechanical transformers.
Piezoelectric Ceramic (PZT) Single Crystal (PZN-PT) Polymer (PVDF)	High peak stress (35 MPa), low strain (1%), very low power density (0.1 W/kg), very high speeds (high frequency, very short stroke actuators – less practical for robotic applications), moderate material (and control), quiet, bilateral actuation. Must be driven with high voltages, “Inchworm” and “waverotor”- type actuators have been developed with larger strains and lower stresses.
Shape Memory Alloy (TiNi)	Very high peak stress (200 MPa), low strain (1–8%), very high power density (100 kW/kg), very low efficiency (< 5%), very difficult to control, slow low voltage activation, low cycle life, unilateral actuation. Can have good form factor for mammal-form robots.
Magnetostrictive (Terfenol-D)	High peak stress (10 MPa), low strain (2%), very high power density (5 W/kg), high efficiency (~ 80%), high speeds are possible, usually unilateral actuation, high material overhead (bulky magnets or coils are required for activation).

However, bending actuators have relatively limited applications due to low force or torque that can be induced. IPMC actuators require some humidity to work and may eventually dry out and stop working. Despite this shortcoming and the fact that they work

in bending mode, IPMCs have been the most widely applied actuators, at least at the research level. They are easy to drive, produce, and handle. Mechanically, they are much stable than gels and can be produced in large sheets from which any form can be cut.

Table 2-4. Advantages and disadvantages of ionic EAP [9].

Advantages	Disadvantages
• Requires low voltage (1.0–5 V) to stimulate a bending response with low frequency below 1 Hz. • Provides predominately bending actuation (longitudinal mechanisms can be constructed). • Exhibits large bending displacements (deformation). • Longitudinal mechanisms can be constructed. • Responses to high frequency input (100 Hz). • Miniaturization is possible (millimeter order). • Durability is high (> 10^5 cycles). • Moves in water or in a wet condition. • Easily processed/formed. • Performs stress (0.1–1MPa) and strain (1–10%).	• Except for CP (Conductive Polymers), ionic EAPs do not hold strain under DC voltage. • Except for CP and CNT (carbon nanotubes), it is difficult to produce a consistent material (particularly IPMC) • Slow response (fraction of a second). • Bending EAPs induce a relatively low actuation force. • Low mechanical energy density and lack of robustness. • In aqueous systems the material sustains hydrolysis at > 1.23 V. • Poor understanding of processing-property relationships. • Higher speeds and work capability desired.

2.4 Prior Applications of IPMC

Several of the characteristics of the IPMC actuator distinguishing itself from other actuators are considered advantages. An example is the fact that actuation is possible with low electric fields — typically no more than a few volts are required. These small potentials can be easily imbedded by simple control circuits. The fact that they operate at low voltages makes ionic polymer actuators well suited to battery-operated devices.

As a polymer, EAP materials can be easily formed in various shapes, their properties can be engineered and they can potentially be integrated with MEMS sensors to produce smart actuators. The most attractive feature of EAP materials is their ability to emulate the operation of biological muscles with high fracture toughness, large deformation, and inherent vibration damping.

EAP-based actuators could eliminate the need for gears, bearings, and other components that complicate the construction of robots, which reduce the cost and the weight. The following categorizes the practical applications of IPMCs.

- Planetary Application — the NASA Viking and Mars Pathfinder missions notice that operation on Mars involves an environment that causes accumulation of dust on hardware surfaces. The dust accumulation is a serious concern that obstructs long-term operation of optical instruments due to loss of visibility and degrades the efficiency of solar cells to produce power. Planetary dust wiper can remove dust from surfaces [38].
- Robotic Applications — combining the bending and longitudinal strain capabilities of EAP actuators, a miniature robot arm was designed and constructed at JPL [34]. A multi-finger gripper was demonstrated in open loop, but the design of the hooks at the end of the fingers represents allowing securing the gripped object encircled by the fingers [39]. The University of Pisa in Italy emulated facial anatomy with a robotic humanoid head using dielectric elastomer [40]. Mimicking the human face with a simplified array of electroactive artificial muscle may improve relations between human and machines. Biomimetic fish-like propulsion using Ionic Conducting

Polymer Film (ICPF) actuator as a propulsion tail fin for an underwater microrobot swimming structure in water or aqueous medium is developed [41].

- Medicine and Biotechnology — blood vessels of the brain are narrow and complex, and there are many problems and risks of intravascular neurosurgery by using traditional catheter with guide wires. A new type of micro active catheters (MAC) was proposed [42–45]. Shahinpoor and Kim proposed a heart-assist device [46], and Keshavarizi *et al*. suggested using an ionic-polymer actuator to measure blood pressure [47].
- Human-Machine Interface — a virtual tactile feel display device for delicate touch of cloth was developed using Nafion-platinum-composite-type EAP actuators [48].
- Micro-Fluidic Applications – IPMC is a promising material candidate for micorpump applications since it can be operated with low input voltages and can produce large stroke volumes along with controllable flow rates. Micropump is one of the micro and miniature devices, which is installed with sensing and actuating elements [49–52].
- Fuel Cell — Artificial Muscle Research Institute (AMRI) IPMC proposed the chemical process of IPMC could promise for applications of fuel cells, electrolysis, and hydrogen sensors [53].

Note that ionic polymer actuators are a currently developing technology, and researchers are still seeking a niche field to break through the limitations. The applications mentioned above are laboratory demonstrations of concepts — ionic-polymer actuators have not yet found their way into commercial applications due to the lack of suitable engineering models, an important issue addressed in this dissertation.

CHAPTER III

EXPERIMENTAL SET-UP AND INSTRUMENTATION

In this chapter we discuss the experimental setup for the measurement of position and force. The laser distance sensor was used to measure the position of the IPMC strip. For the force measurement, we used the load cell to measure the blocked force. The entire experimental setup is also described here.

3.1 Sensors

A dictionary definition of a 'sensor' is a device that detects a change in a physical stimulus and turns it into a signal which can be measured or recorded. Fig. 3-1 is a schematic diagram of the whole experimental set-up.

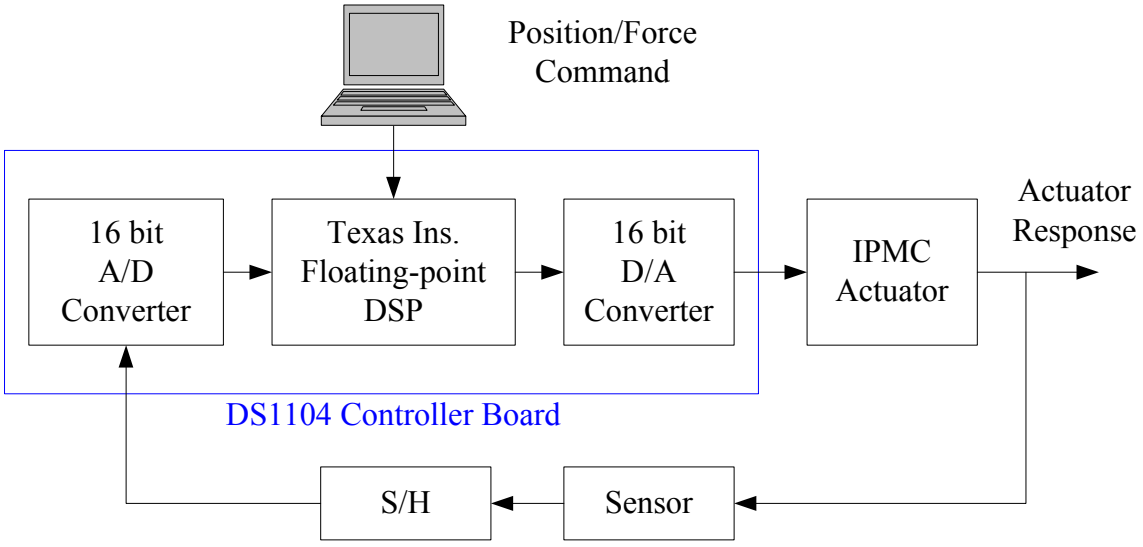

Fig. 3-1. Schematic diagram of the whole experimental setup.

3.1.1 Laser Distance Sensor

We used a laser distance sensor (Model OADM 20I4540/S14C) from Baumer Electric, Ltd. to measure the tip displacements of the IPMC fingers. The analog output of this sensor is in the range of 0–10 V or 4–20 mA. The laser distance sensor has a resolution of 5 μm with a position-noise standard deviation of 10 μm and the operation range is 10 mm with a 15 mm off from the reference as shown in Fig. 3-2. The response time is less than 10 ms. The sensing principal is based on triangulation between the emitter and the receiver. The bending angle could be measurable down to about 30° [54].

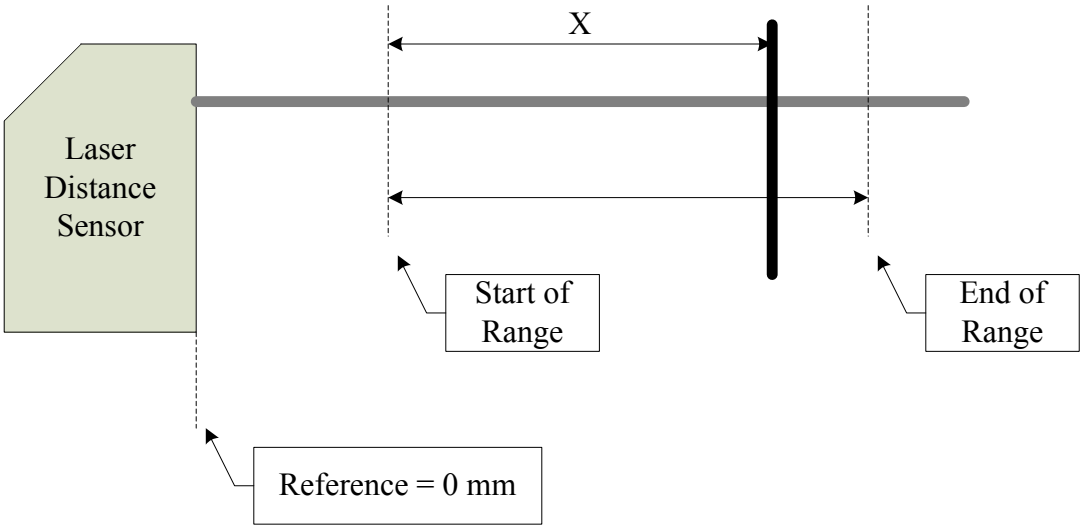

Fig. 3-2. Schematic view of the operating range of the laser distance sensor.

When the IPMC starts to bend, the laser distance sensor can detect the deflection of the tip position on the free end of the IPMC strip. Fig. 3-3 shows a schematic diagram of measuring position responses.

This position measurement is fed to a 16-bit analog-to-digital (A/D) converter of a floating-point digital-signal-processing (DSP) board (Model DS1102 from dSPACE). This DSP board communicates with a Pentium III personal computer for user interface. The control voltage to actuate the IPMC strip is generated through a 16-bit digital-to-analog (D/A) converter channel of the DSP board.

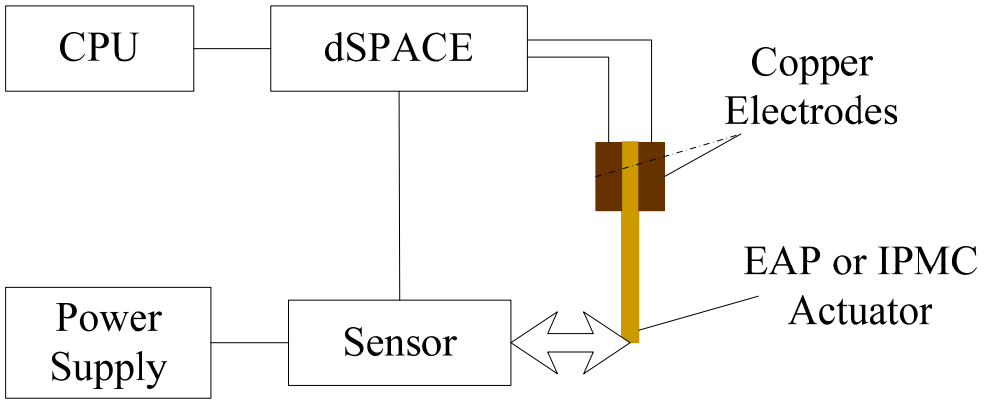

Fig. 3-3. Schematic diagram of measuring position responses.

A clamp (McMaster Inc., GA, USA) was modified by attaching 2 copper electrodes of dimensions 11.43 × 4.28 × 1.27 mm (Alfa Aesar, Ward Hill, MA , USA). Two holes behind the copper electrodes were drilled, allowing wires to be soldered to the electrodes. The copper electrodes between the modified clamps were positioned such that the contact area of the IPMC strip could activate safely under the applied voltage input. Fig. 3-4 shows a photograph of the experimental set-up for position response. The mounted laser distance sensor aims the tip of the IPMC strip, and the modified clamp with the copper electrodes holds the IPMC strip.

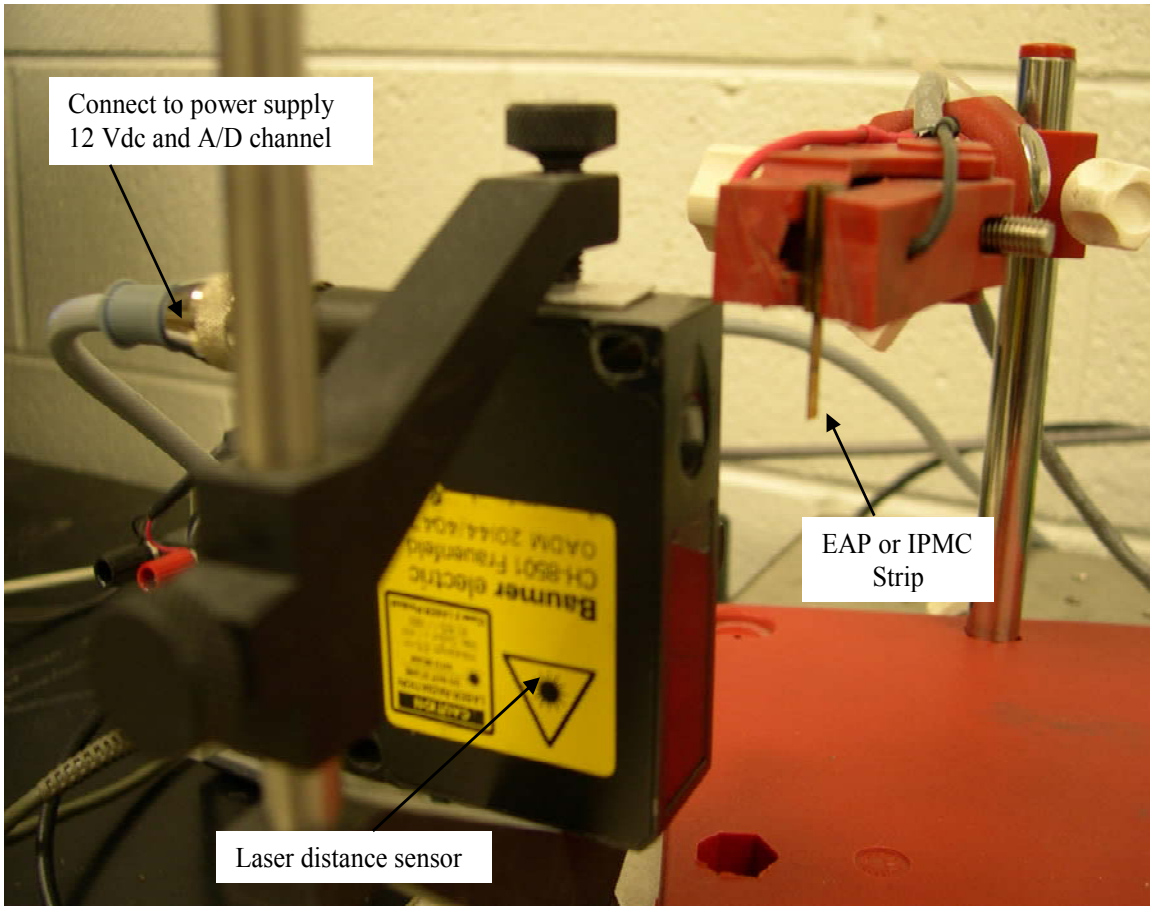

Fig. 3-4. Experimental set-up used for both open-loop and closed-loop position responses.

3.1.2 Force Transducer

A precision load cell (Model GM2, PTC Electronics Inc., Wyckoff, NJ, USA with a full scale of 300 mN, accuracy 0.01 mN), and force resolution of 900 nN was used for the force sensing purpose. For load cells and pressure sensors, PTC Electronics Inc., Wyckoff, NJ, offers a signal amplifier (SCAIME CMJ-CEB, an enhanced version of the CMJ-CE amplifier) that provides a bipolar ±5-V output in addition to 4–20-mA and 0–10 -V outputs as shown in Fig. 3-5. Since the output signal of the load cell was very small, it requires such a signal amplifier. For calibration it needs two adjustments. First is the zero

adjustment. Adjust the zero with potentiometer P2 until the voltmeter displays 0 V measuring the voltage output. Second is the span adjustment. We need to mount the load cell vertically with the armature pointing vertically upwards, and place the 30 g mass on it. The voltage measured from the voltage output must display 30 mV. Otherwise, adjust the span with potentiometer P1 in order to obtain the requested output. We should point out that the output of 6 mV/V, i.e., 30 mV nominal at a 5-V excitation from measuring between EX+ and EX– should be compensated for when the voltage signal is measured from the load cell.

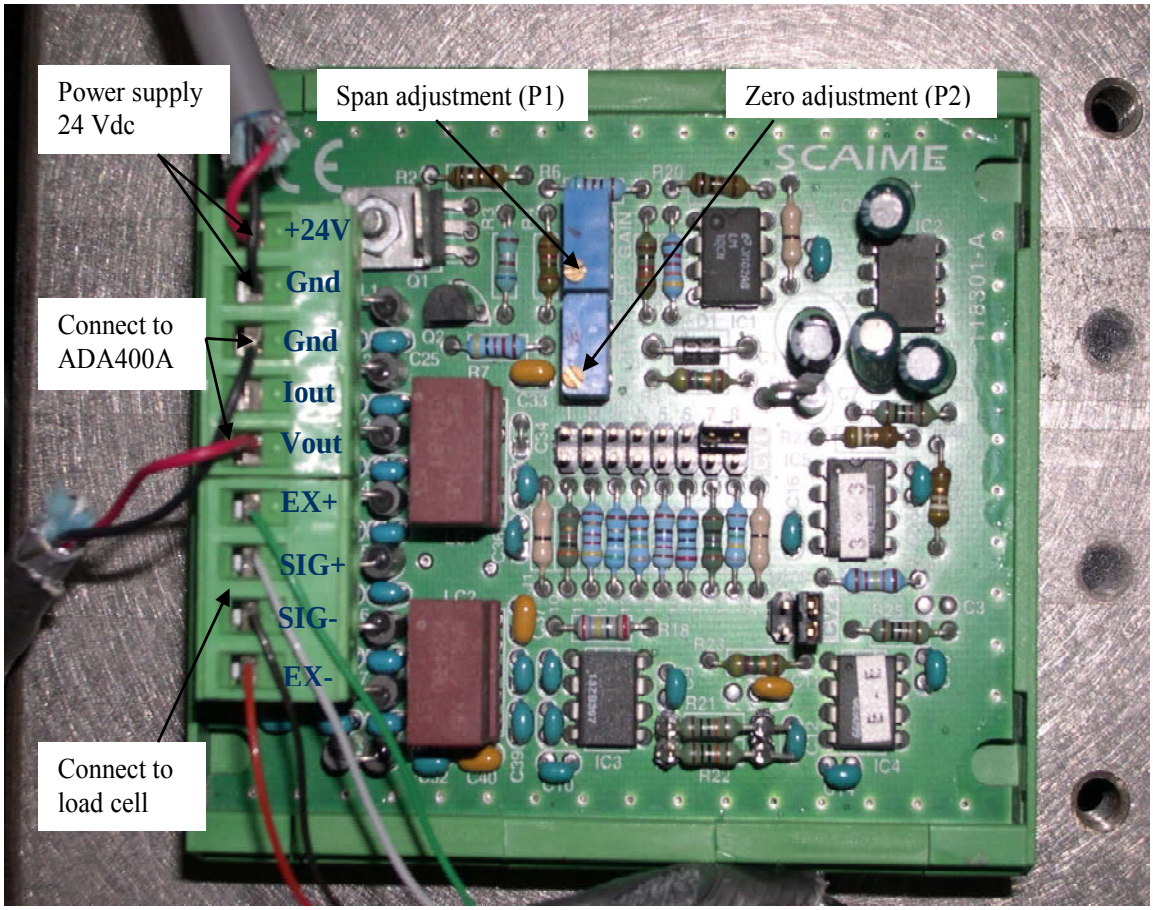

Fig. 3-5. Signal amplifier.

A differential preamplifier (Model ADA 400A, Tektronix Inc., Beaverton, OR, USA) was used not only to amplify the output signal further by a gain value of 1000, but also to reject the sensor noise. A Tekprobe power supply (Model 1103, Tektronix) was connected to this differential preamplifier. The output signal from the Tekprobe power supply was fed to the A/D converter on the dSPACE board. Fig. 3-6 shows the wire connection between the load cell and the dSPACE A/D channel. Fig. 3-7 shows an oscilloscope (Model 54624A, Agilent), a function generator (Model 33120A, Agilent), and a DC power supply (Model E3645A, Agilent).

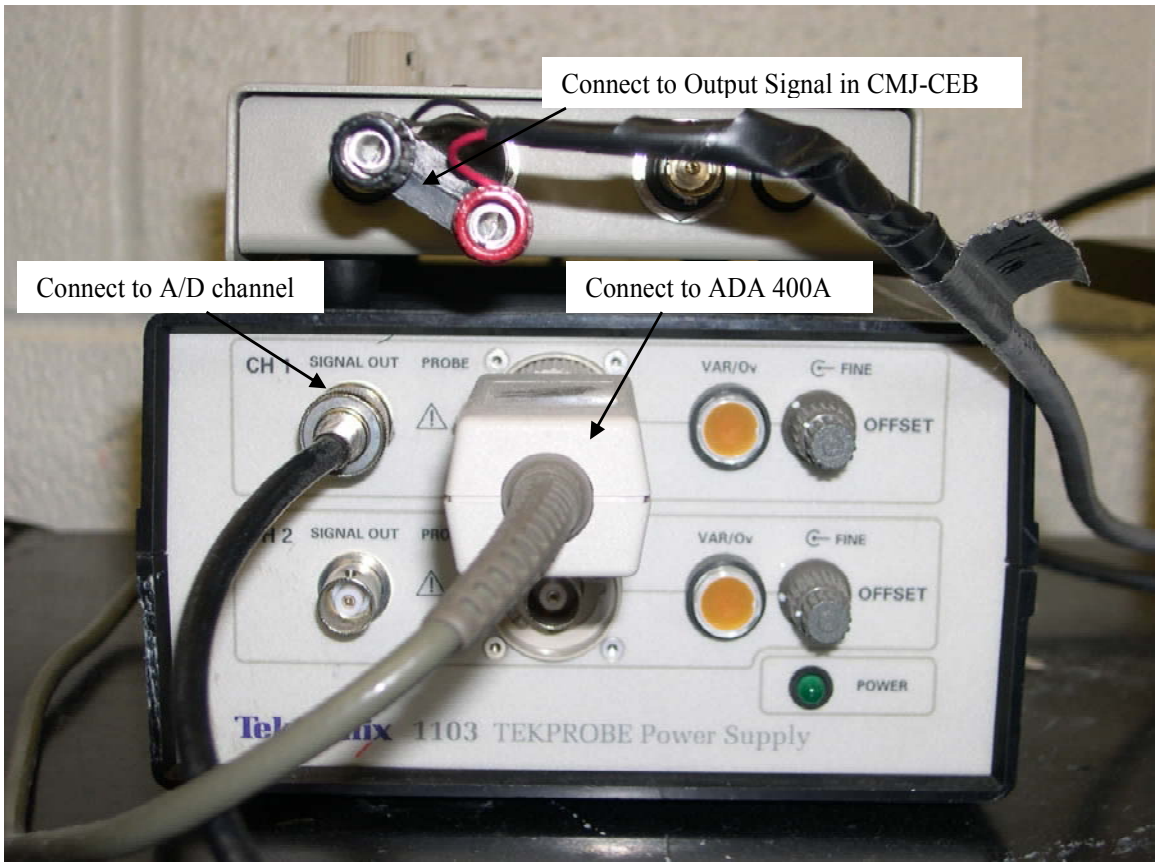

Fig. 3-6. Wire connection between load cell and dSPACE A/D channel.

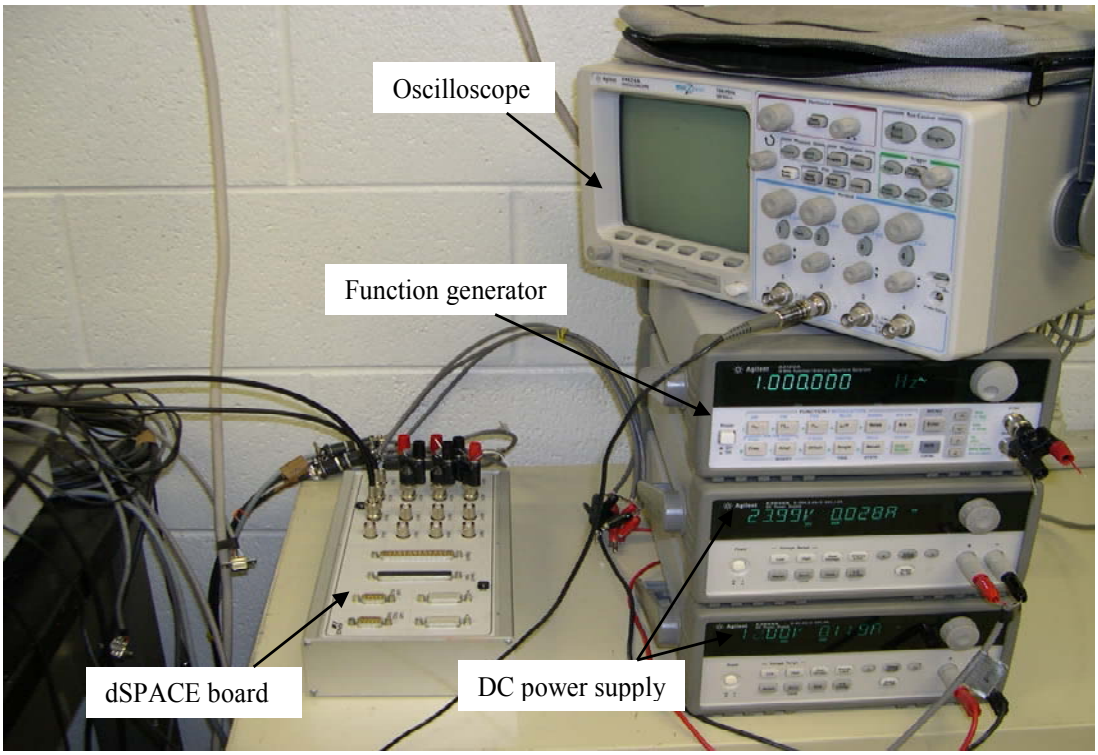

Fig. 3-7. Experimental set-up showing the dSPACE board, oscilloscope, and power supply.

After proper calibration, the output signal of the load cell can be read as a force signal. For this purpose, the IPMC strip held by the modified clamp sticks to the calibrated load cell as shown in Fig. 3-8.

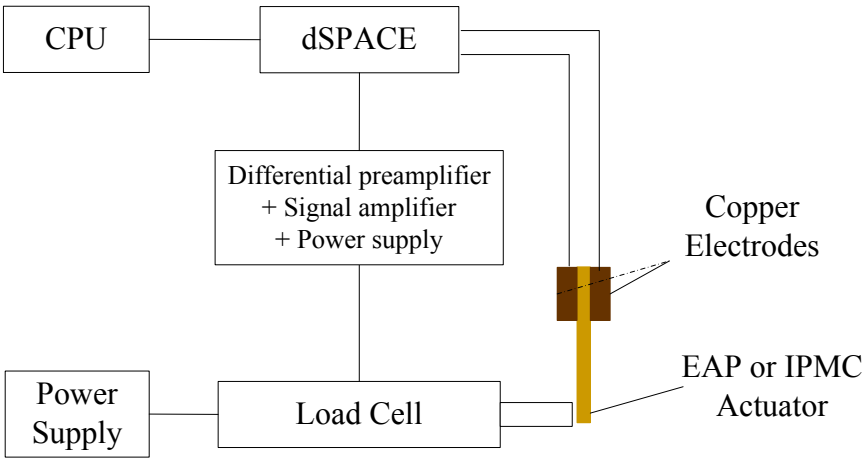

Fig. 3-8. Schematic diagram for force sensing experiment.

Fig. 3-9 shows the experimental setup related to the load cell. It was mounted on the aluminum platform so that the tip of IPMC held by the modified clamp would touch the tip of the load cell as shown in Fig. 3-10. The load cell could then measure the blocked force generated from the IPMC strip when it was exited by the applied input signal. Fig. 3-11 is the close-up photograph of the experimental set-up of position and force sensing.

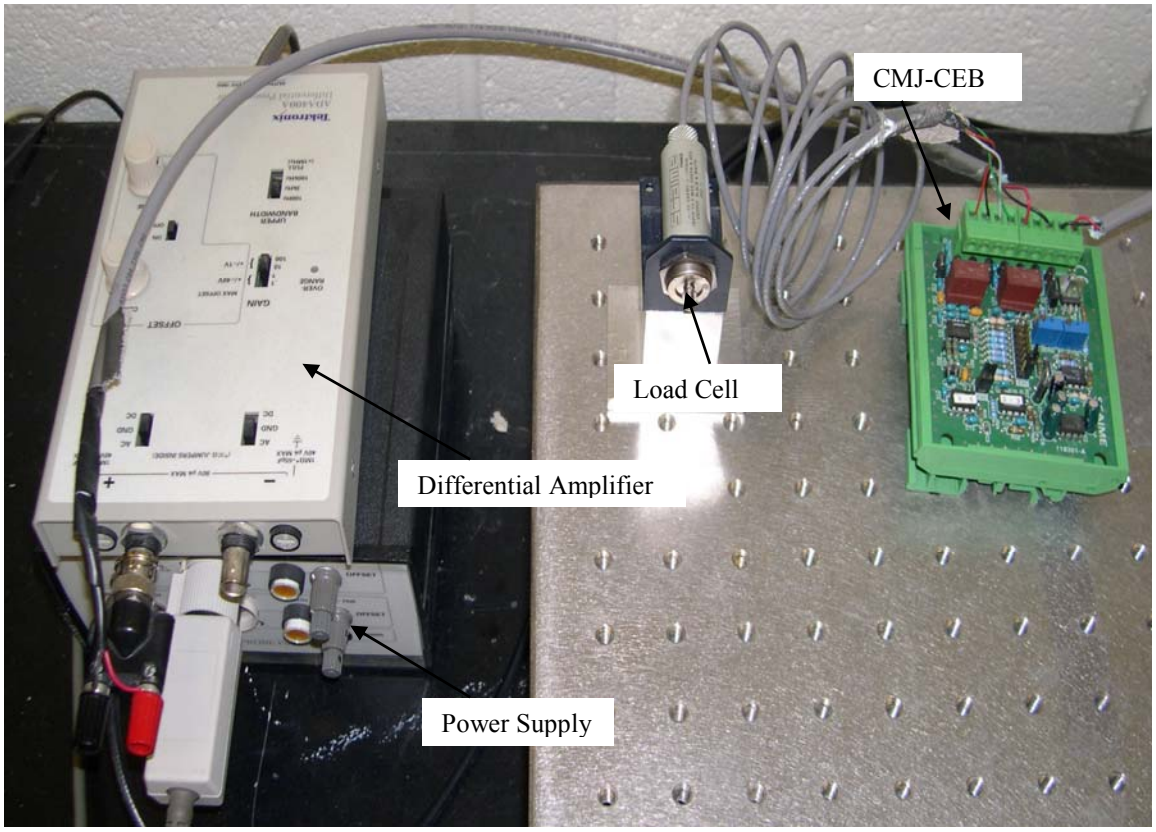

Fig. 3-9. Experimental set-up connected to the load cell.

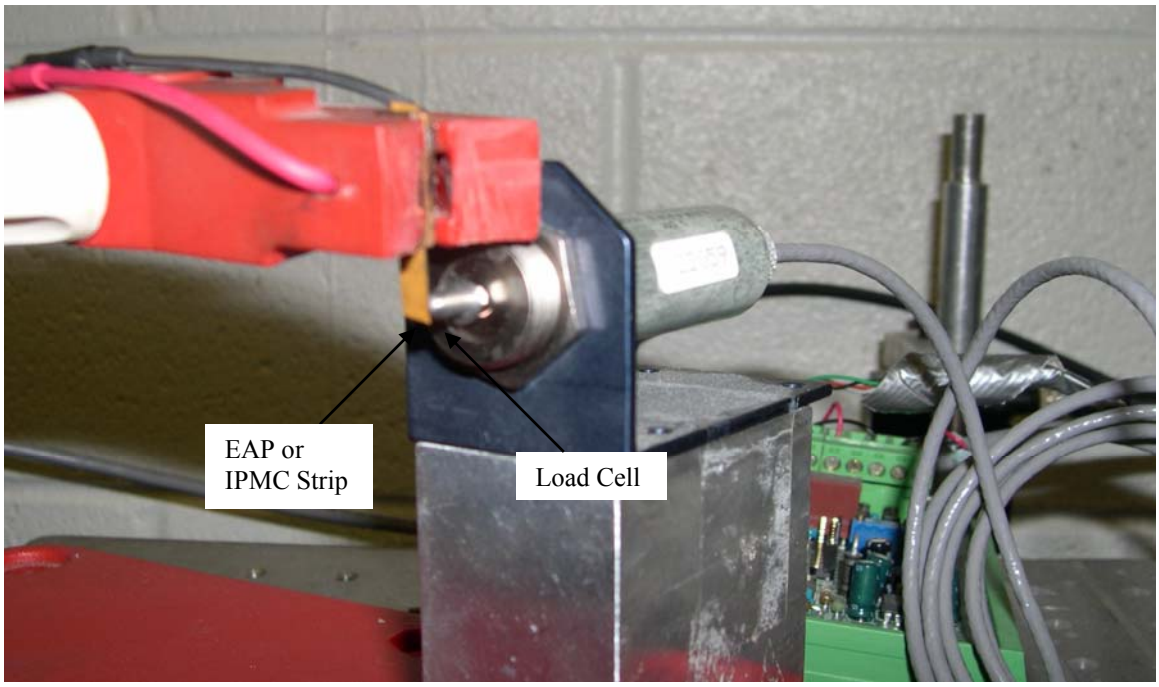

Fig. 3-10. Close-up view of the force-sensing set-up with the EAP/IPMC strip.

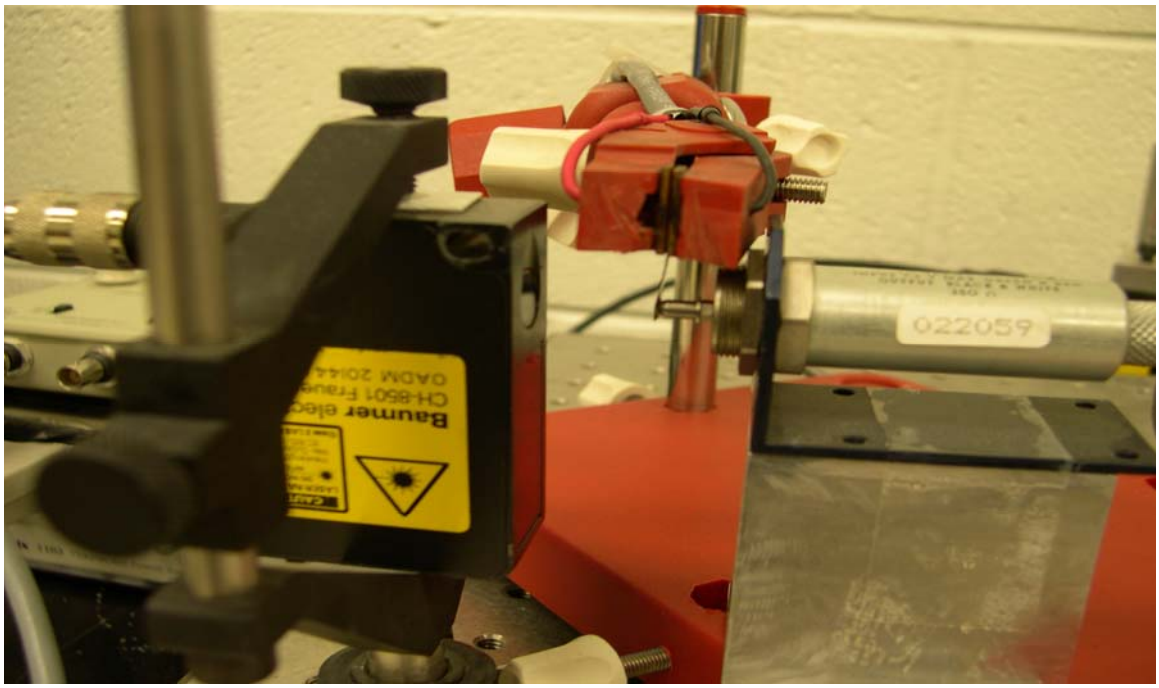

Fig. 3-11. Close-up view of position and force sensing.

3.2 Data Acquisition System

The dSPACE DS1102 DSP (digital signal processor) was used to generate the electrical input and the output from the position or the force sensor was fed to a 16-bit A/D converter board of a DSP controller board. The unit connects a PC to a maximum of 4 input channels and 4 output channels. The provided Control Desk Developer Version 2.1.1 along with Matlab 6.1 (R12.1) Simulink provides user-friendly interface to system control and observation. We used 1 input and 1 output channels for force control and 3 inputs and 3 outputs for position control. The controller board has Texas Instrument TMS320C31 floating-point DSP. It is linked directly to a PC running dSPACE software. The control desk and DS 1102 are both produced by dSPACE Incorporated. The experiments were conducted with a block schematic in Simulink®, a Matlab program. The Simulink model was then loaded onto the dSPACE hardware, and which handled data acquisition. Currently, the DSP controller board was switched to the DS1104 DSP controller board due to software license/compatibility with MATLAB 7.0. The DS1104 board has a 250-MHz Power PC 603e with Texas Instruments' DSP TMS320F240 chip. It contains four 16-bit A/D channels, four 12-bit A/D channels, eight 16-bit D/A channels, and other input/output interfaces. The Control Desk Developer Version 2.6.5 is interfaced with Matlab 7.0 (R14). The usage of A/D and D/A channels follows the same pattern with the DS1102 board.

3.3 Three-Finger Gripper

The three-finger gripper consists of three strips of IPMC clamped by cooper electrodes. Each IPMC strip can be controlled individually and approach the target object

independently. One of the IPMC strips can work as a switch since the IPMC itself generates the voltage output with being mechanically touched by the object. This IPMC strip can tell when the force control is required to start so that the three-finger gripper can grip the target object without damaging it. Fig. 3-12 shows a schematic cross-sectional view of this three-finger gripper. The object denoted with a circle has a radius r, and the three fingers around it move within the controlled range l independently. The width w can be modified to be a wedge in case of handling even more small size object.

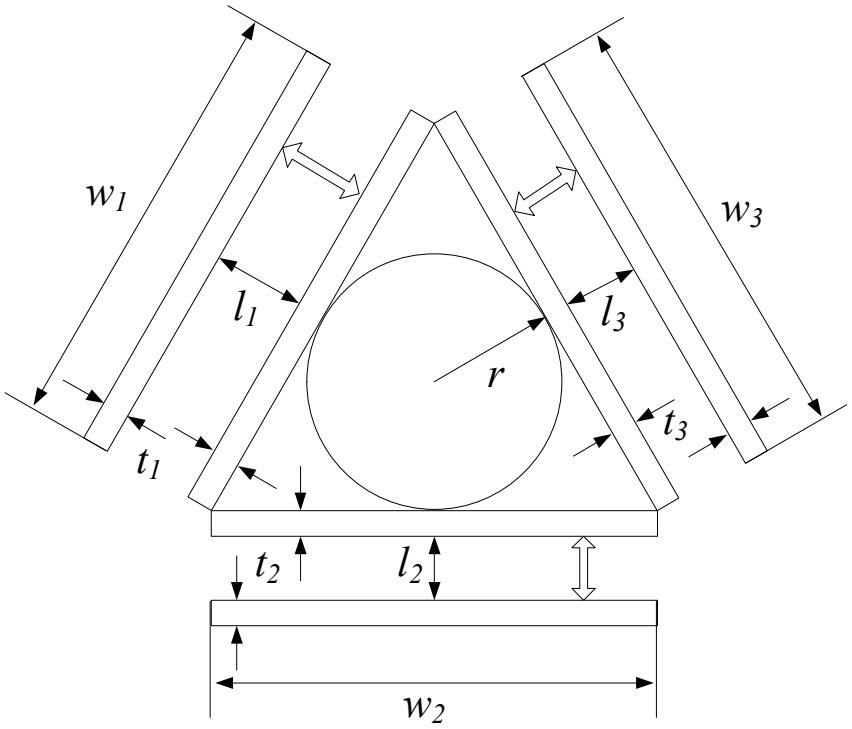

Fig. 3-12. Schematic cross-sectional view of three-finger gripper.

The three-finger gripper was designed to perform the desirable demonstration of the capability of the gripper — opening the gripper fingers, bringing the gripper near the object, closing the fingers, and lifting the object. By increasing the control voltage, the

amount of gripping force is increased, and a firmer grasp is achieved. We provide an interesting mechanism to explore how closed-loop-controlled macro- and micro-gripping is achieved in Chapter VI. The entire experimental setup is shown in Fig. 3-13 and Fig. 3-14 and 3-15 are the close-up view of the three-finger gripper and its top view, respectively.

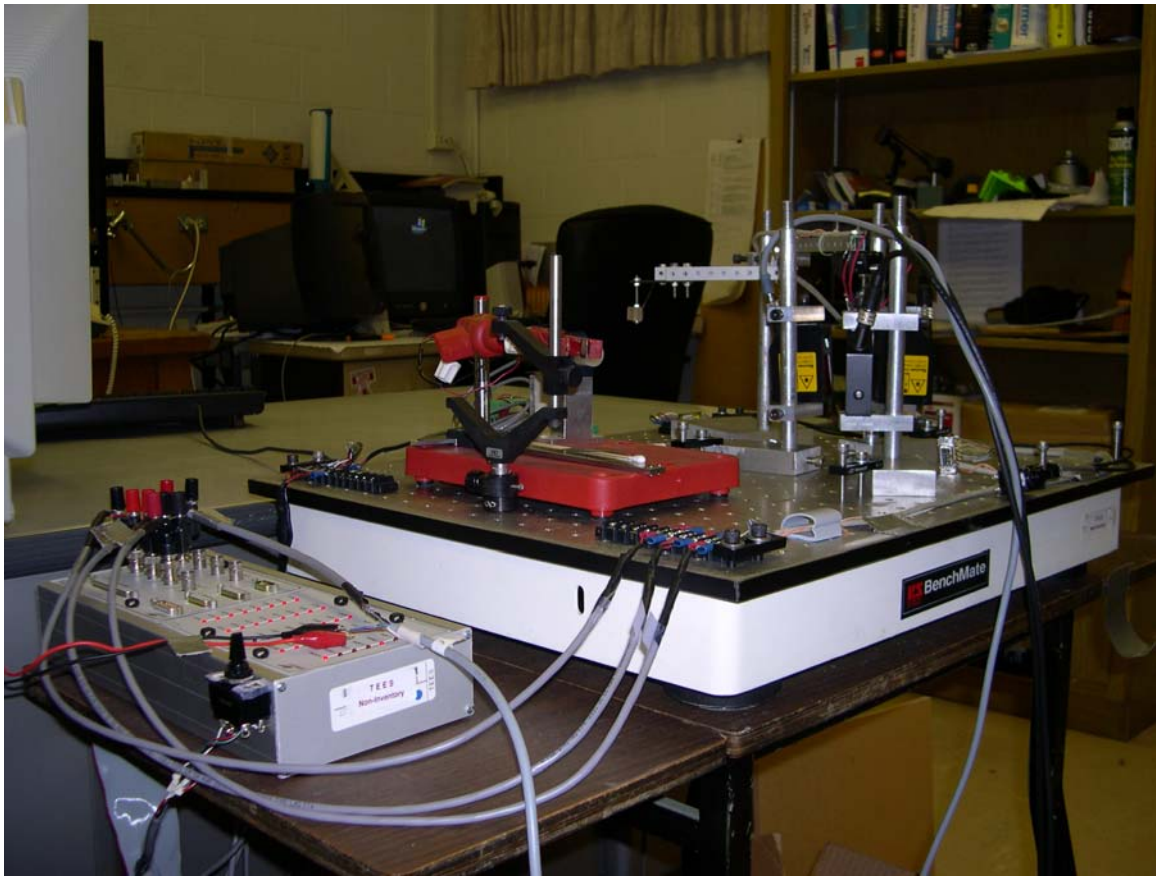

Fig. 3-13. The entire experimental setup for the three-finger gripper.

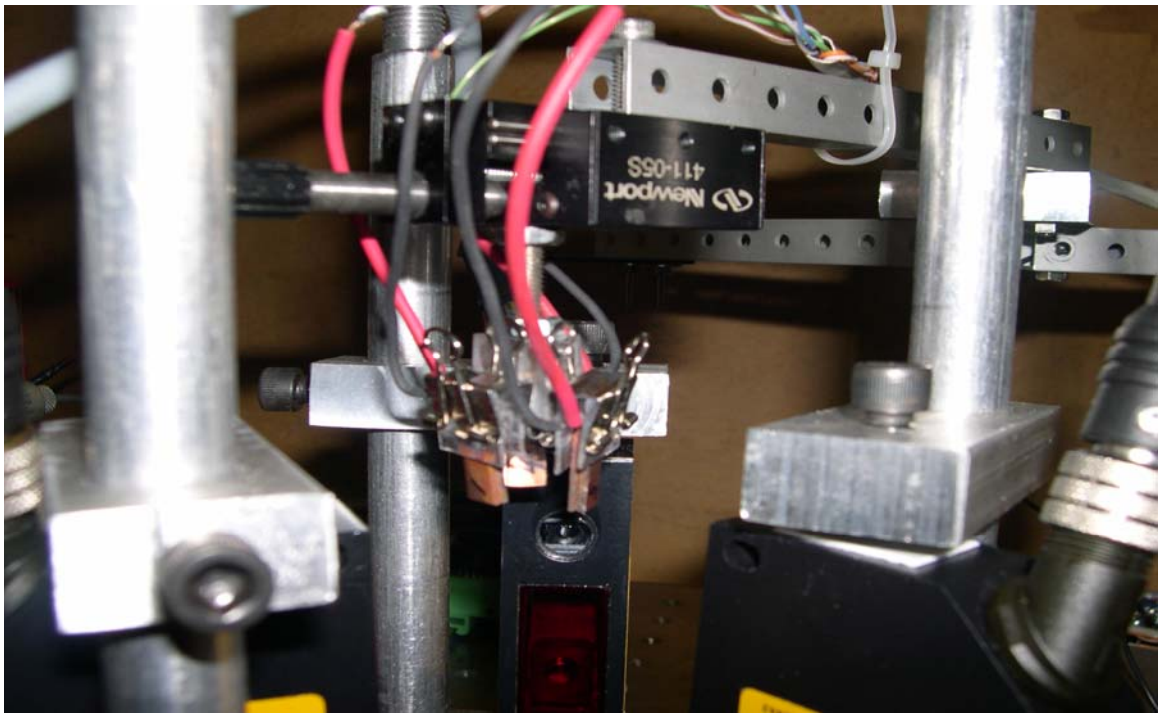

Fig. 3-14. Close-up view of the three-finger gripper.

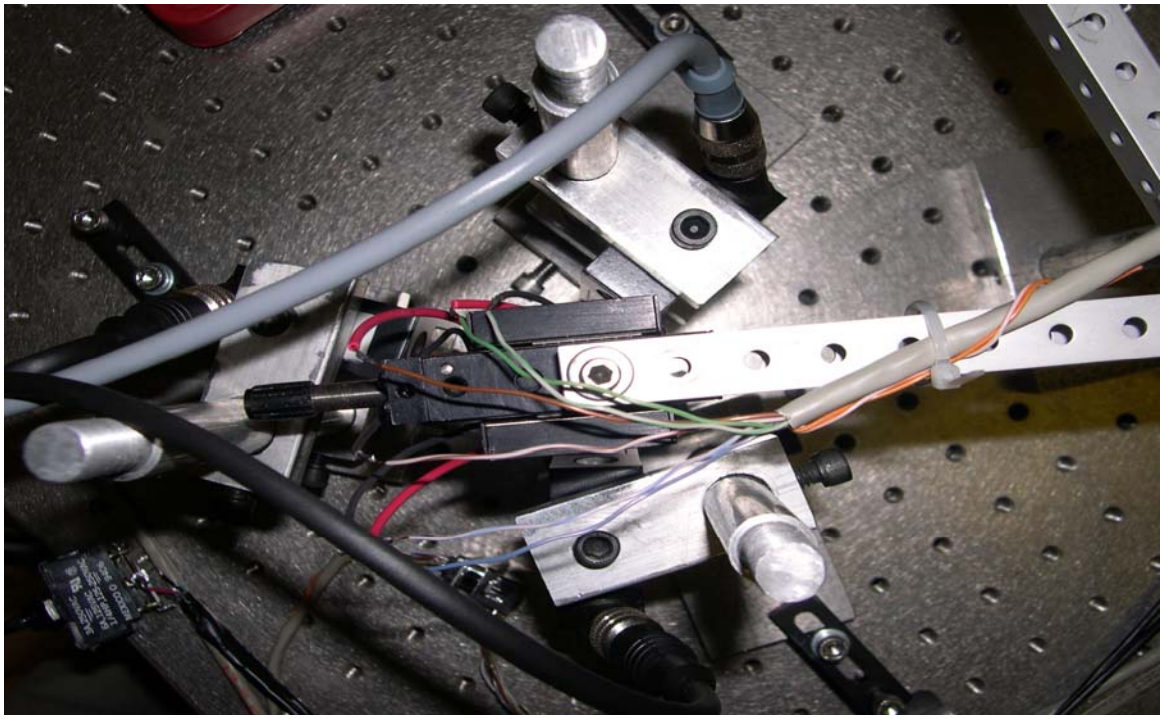

Fig. 3-15. Top view of the three-finger gripper.

CHAPTER IV

MODELING AND DYNAMIC BEHAVIOR

This chapter describes the system identification process by observing various input/output characteristics of EAP and IPMC strips. All the various transfer functions from the system identification are used to design the controller in the next chapter.

4.1 System Identification

System identification focuses on the modeling of dynamical systems based on measured data. The model from the system identification could be used for control, prediction, signal processing, error detection, or simulation. The purpose of the model affects the choice of identification methods and experimental conditions, and it should therefore be clearly stated. Fig. 4-1 shows an algorithm for modeling and system identification. System identification is an iterative process and it is often necessary to go back and repeat earlier steps. This is illustrated with arrows in the figure. Notice that the order of the blocks in the algorithm does not only describe the chronological order the tasks are performed, but also how they influence each other. A certain model structure can be derived from the physical model such as Piezoelectric material, Shape Memory Alloy (SMA), etc. although they might contain unknown parameters to be estimated. Since there are a lack of prior information and the limits of the physical modeling, EAP and IPMC are treated as black-box identification so that the input and the output relationship can describe the behavior of the characteristics of the IPMC system. The black-box

identification is important to move to grey-box identification where some part of the system is known.

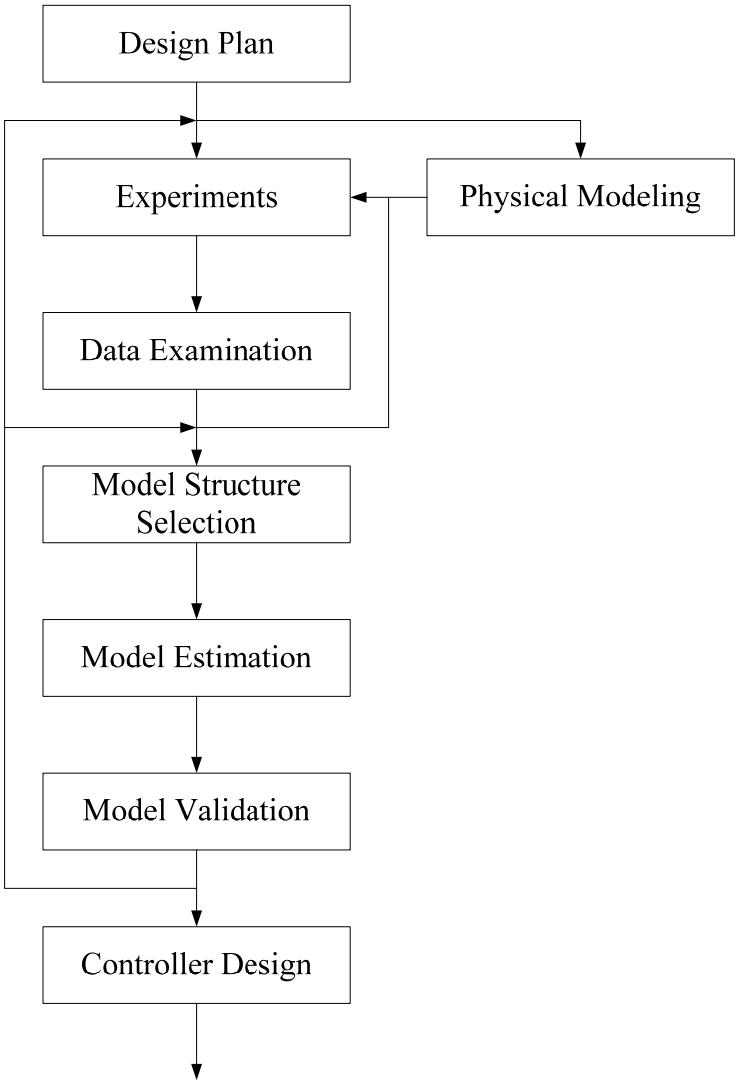

Fig. 4-1. Algorithm for modeling and system identification [55].

The experiments are done in two steps. In the first step, preliminary experiments, such as impulse and step responses are performed to obtain primary knowledge about the important system characteristics such as gain, time delay, and time constants. It is also

possible to draw conclusions from the experiments about whether or not the system is linear and time invariant and if there are disturbances acting on the system. For the transient-response analysis, a step response analysis gives information on gain, time delay, and time constant. For the frequency-response analysis, this gives an estimated transfer function for the system. In the second step, the information obtained from the preliminary experiments is then used to determine suitable experimental conditions for the main experiments, which will give the data to be used in the System Identification Toolbox [56]. In particular, the choice of the input signal is discussed. The system identification gives an accurate model at the frequencies where the input signal has contains much energy. In other words, the input signal has a good excitation at these frequencies. The frequency content of the input signal should therefore be concentrated to frequencies where small estimation errors are desired. A pseudo-random binary sequence (PRBS) is a common choice of input signal, since it has large energy content in a large frequency range. White Gaussian noise is also a good candidate for the input signal since its power spectrum density has equal power in any frequency range. In addition, chirp signals or swept sinusoids give good control over the excited frequency band [55].

4.1.1 Model Structure Selection

The model structure determines the set in which the system identification is performed. The most general parametric model structure which called Prediction Error Estimate (PEM) shown in Fig. 4-2 in the System Identification Toolbox [55] is given by

$$A(q)y(t)=\frac{B(q)}{F(q)}u(t-n_k)+\frac{C(q)}{D(q)}e(t), \tag{4-1}$$

where y and u are the output and input sequences, respectively, e is a zero-mean white noise sequence, and n_k is the number of delays from the input to the output [55, 57]. The polynomials A, B, C, D, and F are defined in terms of the backward shift operator, q^{-1}:

$$A(q)=1+a_1q^{-1}+\cdots+a_{n_a}q^{-n_a},\quad B(q)=b_1+b_2q^{-1}+\cdots+b_{n_b}q^{-n_b+1},$$

$$C(q)=1+c_1q^{-1}+\cdots+c_{n_c}q^{-n_c},\quad D(q)=1+d_1q^{-1}+\cdots+d_{n_d}q^{-n_d},$$

$$F(q)=1+f_1q^{-1}+\cdots+f_{n_f}q^{-n_f}.$$

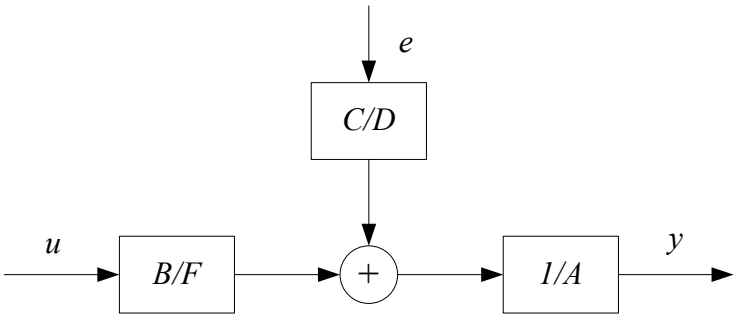

Fig. 4-2. PEM model structure.

Based on the general parameter model structure (4-1), some special forms are set to identify as following:

Auto-Regression (AR) model is

$$A(q)y(t)=e(t), \tag{4-2}$$

which is a time-series model with no exogenous input (no input $u(t)$).

Auto-Regression with eXogeneous input (ARX) model is

$$A(q)y(t) = B(q)u(t-n_k) + e(t). \tag{4-3}$$

Auto-Regressive Moving Average with eXogeneous input (ARMAX) model is

$$A(q)y(t) = B(q)u(t-n_k) + C(q)e(t). \tag{4-4}$$

Output-Error (OE) model is

$$y(t) = \frac{B(q)}{F(q)}u(t-n_k) + e(t). \tag{4-5}$$

Box-Jenkins (BJ) model is

$$y(t) = \frac{B(q)}{F(q)}u(t-n_k) + \frac{C(q)}{D(q)}e(t). \tag{4-6}$$

Within the structure of (4-1), virtually all the usual linear black-box model structures are obtained as special cases. The ARX structure is obviously obtained with $C(q) = D(q) = F(q) = 1$. The ARMAX structure corresponds to the case of $D(q) = F(q) = 1$. The output-error model is obtained with $A(q) = C(q) = D(q) = 1$, while the Box-Jenkins model corresponds to the case of $A(q) = 1$.

Equation (4-6) can be rewritten as

$$y(t) = G(q)u(t - n_k) + H(q)e(t), \tag{4-7}$$

where $G(q) = \frac{B(q)}{F(q)}$, $H(q) = \frac{C(q)}{D(q)}$. The symbol G denotes the dynamic properties of the system, that is, how the output is formed from the input. For linear systems it is called the transfer function from input to output. The symbol H refers to the noise properties, and is called the disturbance model. It describes how the disturbances at the output are formed from some standardized noise source $e(t)$. For the simulation purpose, the disturbance model plays no immediate role since the noise source $e(t)$ for new data will be unknown. It is taken as zero in the simulations, so as to study the effect of the input alone (a noise-free simulation). Making another simulation with $e(t)$ being an arbitrary white noise will reveal how reliable the result of the simulation is, but it will not give a more accurate simulation result for the actual system's response.

It is not at all necessarily true that a model with more parameters or more freedom (more polynomials) is better. Finding the best model is a matter of choosing a suitable structure in combination with the number of parameters.

For an output-error parameter estimation case, the one-step-ahead predictor for $y(t)$ is following:

$$\hat{y}(t|t-1) = -f_1\, y(t-1) - \cdots - f_{nf}\, y(t - n_f) + b_1 u(t - n_k) + \cdots + b_{n_b} u(t - n_k - n_b + 1), \tag{4-8}$$

where $\hat{y}(t|t-1)$ denotes a prediction of $y(t)$ given the data up to the (t–1) step. Equation

(4-8) can be expressed as a linear regression problem via

$$\varphi = \left[-y(t-1) \cdots -y(t-n_f) \;\; u(t-n_k) \cdots u(t-n_k-n_b+1) \right]. \qquad (4\text{-}9)$$

The parameter vector to be determined is

$$\theta = \left[b_1 \cdots b_{n_b} \;\; f_1 \cdots f_{n_f} \right]^T. \qquad (4\text{-}10)$$

Rewriting the objective ("loss") function as

$$\min_{\theta} V = \min_{\theta} \frac{1}{N} \sum_{i=1}^{N} \left[y - \varphi^T(t)\theta \right]^2 \qquad (4\text{-}11)$$

leads to the well-established linear least-squares solution [54]

$$\hat{\theta} = \left[\frac{1}{N} \sum_{t=1}^{N} \varphi(t)\varphi^T(t) \right]^{-1} \frac{1}{N} \sum_{t=1}^{N} \varphi(t) y(t). \qquad (4\text{-}12)$$

This procedure can be applied to Box-Jenkins parameter estimation when the error term from (4-6) is omitted.

4.1.2 Model Estimation

Model estimation is the procedure of deriving a model. There are non-parametric

models and parametric models. A non-parametric model consists of a time response or a frequency response; hence impossible to parameterize it with a few parameters. In practice, it is often useful to first derive a non-parametric model, and then using it as a coarse estimate of what the parameter model should look like; giving a suggestion of the model structure.

Non-parametric estimation methods are based on either correlation analysis or spectral analysis. Correlation analysis directs estimation of impulse response coefficients from identification data, and spectral analysis directs estimation of frequency response from identification data. A major advantage of the non-parametric methods is that they need no specification of the model structure in terms of model structure, model order, etc.

Parametric estimation models are based on the selected model structures. The next steps are then to choose an approximate model order which is required to be specified and to estimate the parameters of the polynomials.

By estimating a high-order model we capture most of the information in the data. After estimating the model order and the parameters of the polynomials, the model reduction may be necessary to extract the most significant states of the model. This is directly related to the minimal realization of the plant model.

4.1.3. Input Signals

Models describe the relationship between input signals and output signals. The signals are functions of time, and the value of the input at time t will be denoted by u (t). Measurement equipment typically records the signals at discrete-time with a sampling interval of T time units.

The frequency response of a linear dynamic model describes how the model reacts to sinusoidal inputs. If we let the input *u* (*t*) be a sinusoid of a certain frequency, the output *y* (*t*) will also be a sinusoid of this frequency. Therefore, we apply a linear chirp signal to the IPMC and check how it reacts to the given inputs. A chirp signal is often used for dynamic structural analysis. In order to identify the system dynamics of IPMC, a chirp signal can be implemented for *u* (*t*) as follows:

$$f_u(t) = f_{u1} + \frac{f_{u2} - f_{u1}}{M} t \,, \tag{4-13}$$

for $0 \le t \le M$,

$$\begin{aligned} u(t) &= A \sin\left(2\pi \int_0^t f_u(\tau) d\tau \right) \\ &= A \sin\left(2\pi \left[f_{u1} t + \frac{f_{u2} - f_{u1}}{2M} t^2 \right] \right), \end{aligned} \tag{4-14}$$

where the instantaneous frequency $f_u(t)$ of $u(t)$ increases from f_{u1} to f_{u2} over a time period *M*. Therefore this gives a good control over the excited frequency band. Fig. 4-3 shows the Simulink diagram for the chirp signal generator. Port 1 for a subsystem of the chirp signal in Fig. 4-3 is connected to the gain *A* in Fig. 4-4. A Simulink diagram of the open-loop position response is shown in Fig. 4-4.

The input should provide persistent excitation in the frequency range where the model needs to be accurate. The chirp signal inputs were generated in the frequency range of [0.01Hz, 1 Hz] for 30 s for EAP and [0.01Hz, 5 Hz] for 40 s for IPMC at a sampling frequency of 250 Hz.

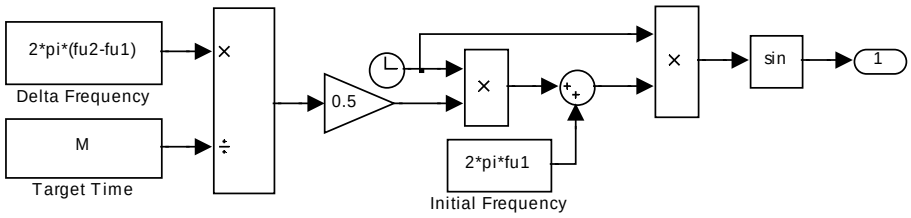

Fig. 4-3. Simulink® block diagram for the chirp signal.

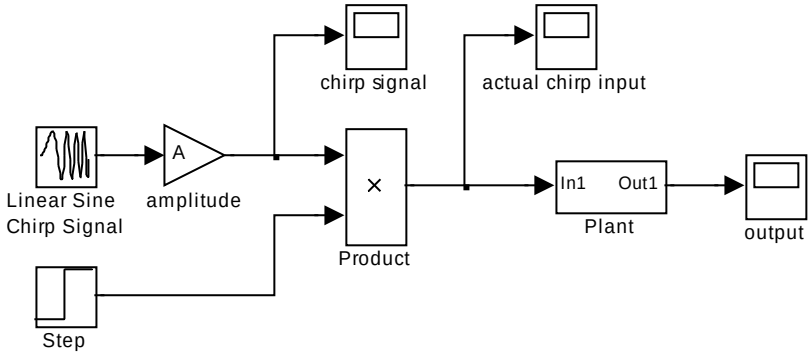

Fig. 4-4. Simulink® block diagram for the open-loop position response.

4.2 Position-Transduction Models

In this section the system identification of EAP and IPMC modeling is presented in terms of position. The inherent behavior of EAP and IPMC is discussed based on the modeling. Here are two types of actuators (EAP and IPMC type) which are identified. EAP and IPMC strips were cut in the dimension of 25.18 mm × 4.24 mm × 0.18 mm and 22.01 mm × 3.01 mm × 0.2 mm, respectively.

4.2.1 Open-Loop Position Response of EAP

In this section, a dynamic model of the EAP actuator by system identification is presented. The persistency of excitation is guaranteed by selecting the reference input

signal to have a desired range of frequency with sufficient amplitude [58]. A low-voltage signal (0.1–7.0 V) was applied across the thickness of the EAP strip, and the strip bending was recorded with the laser displacement sensor. The largest deflection could be obtained at the resonant frequency of the EAP strip. Other arbitrary waveforms can also be applied to generate desired motion. The chirp signal response offers the control of both the amplitude and frequency range of the input [32]. The dwelling time and the frequency interval are keys to control the degree of dynamic equilibrium. The chirp-signal testing is particularly appropriate for nonlinear systems because the analysis of the test results is usually easier for sinusoidal excitation than others [59].

Fig. 4-5 (a) shows such a chirp-signal response of our EAP-strip actuator. The chirp signal input shown in Fig. 4-5 (b) excited the actuator in the interesting frequency range of [0.01 Hz, 1 Hz] for 30 s at a sampling frequency of 250 Hz. The frequency of a chirp signal such as shown in Fig. 4-5 (b) is strictly controlled to be within the range between the starting (0.01 Hz) and ending (1 Hz) frequencies.

Fig. 4-6 (a) is a fast Fourier transform (FFT) of the output displacement shown in Fig. 4-6 (a). The FFT magnitude in Fig. 4-6 (a) decreases with respect to the increasing frequency due to the band-limited dynamics of the EAP actuator. Fig. 4-6 (b) shows an FFT response of the chirp signal input shown in Fig. 4-5 (b). Since the amplitude of the chirp signal input is constant, its FFT magnitude from 0.01 Hz to 1 Hz appears like a flat hat. There are many ways to represent the system model, but we used an ARMAX method based on the best fit of the input-output data. If the reference input has persistent enough frequency components, the estimated parameters will converge in this range [58].

For the system identification the discrete-time model structure for the EAP-strip

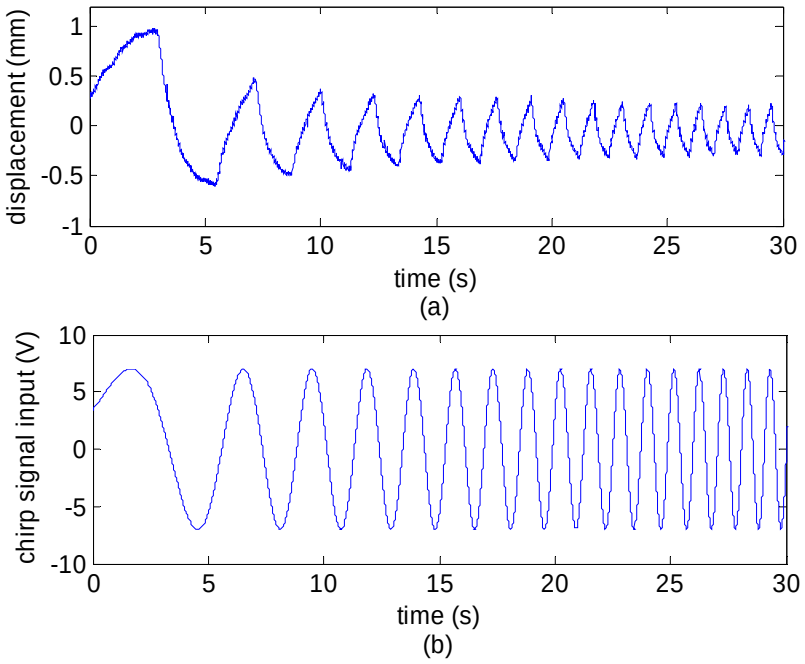

Fig. 4-5. (a) The open-loop response of the EAP strip to (b) a linear swept-frequency (chirp) signal with the 7V amplitude. At $t = 0$ s, the frequency was 0.01 Hz and continuously increased to 1 Hz at $t = 30$ s.

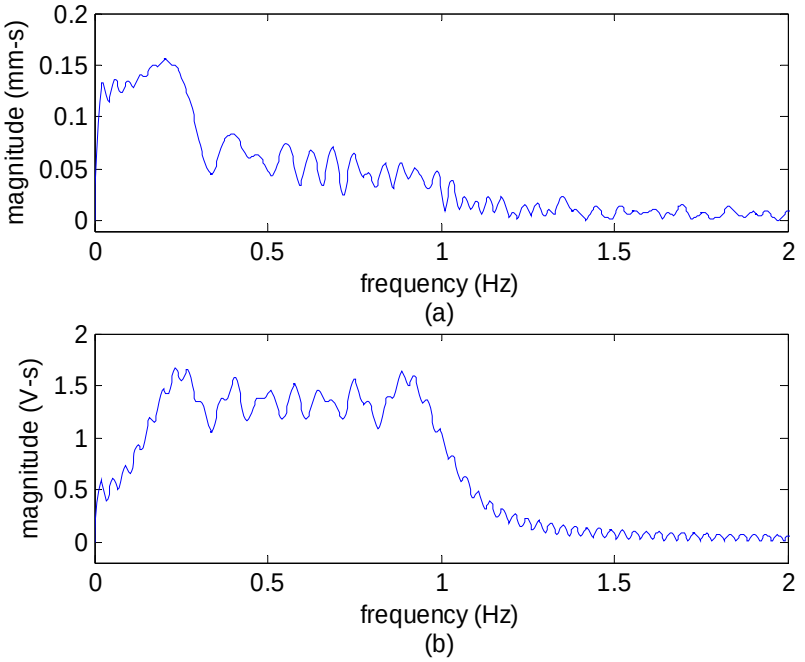

Fig. 4-6. (a) FFT magnitude of the measured displacement. (b) FFT magnitude of the chirp input signal.

actuator was set as following:

$$A(q)\, y(t) = B(q)\, u(t - n_k) + C(q)\, e(t)\,, \tag{4-15}$$

where y is the measured output, u is the manipulated or exogenous input sequence, and e is the variance of the white noise [54, 56]. The polynomials $A(q)$, $B(q)$, and $C(q)$ in the shift operator q were found to be

$$\begin{aligned} A(q) &= 1 - 1.995\, q^{-1} - 1.034 q^{-2} - 0.03881 q^{-3}\,, \\ B(q) &= 0.0204 - 0.03732 q^{-1} - 0.017 q^{-2}\,, \\ C(q) &= 1 - 1.487 q^{-1} + 0.5119 q^{-2} - 0.06948 q^{-3}\,. \end{aligned} \tag{4-16}$$

The coefficients of the polynomials $A(q)$, $B(q)$, and $C(q)$ were identified by minimizing a prediction error with n_k=0. The Matlab command 'armax' was extensively used to design the parametric model structure. From (4-16), we found the transfer function $P(z)$ from the input and the output that represents the dynamics of the system.

$$P(z) = \frac{0.02752 z^3 - 0.05163 z^2 + 0.0242 z}{z^3 - 0.9644 z^2 - 0.9194 z + 0.8845}\,. \tag{4-17}$$

Fig. 4-7 shows the comparison of the measured input with the third-order ARAMA model's output in response to the chirp signal. These well-matched responses demonstrate the accuracy of the model. The controller will be designed in Chapter V

based on this derived system model. From the cross-validation, the percentage of the matched BJ models was 74.01%.

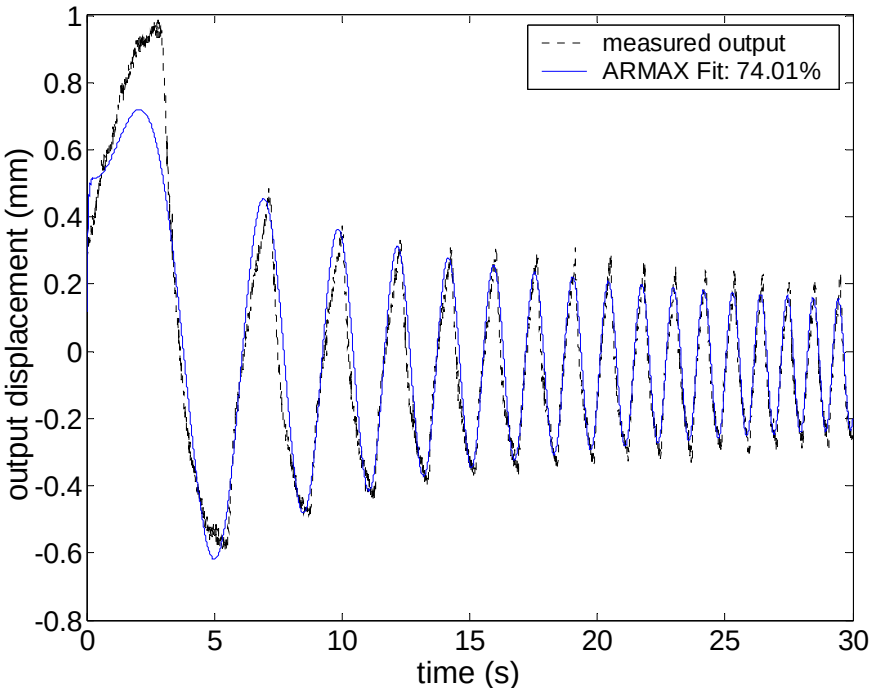

Fig. 4-7. Comparison of the measured output with the ARMAX model's output in response to the chirp signal.

4.2.2 Open-Loop Position Response of IPMC

In this section, a linearlized dynamic model of the IPMC actuator by system identification is presented. Because of their importance, nonlinear characteristics in IPMC actuation have been studied recently. Shahinpoor and Kim [31] represented IPMC behaviors with small hysteresis. The particle electrodes on the IPMC surface primarily affected its hysteretic behavior [60]. Kothera et al. [61] presented nonlinear distortion using the Volterra series. A systematic methodology is developed in this dissertation to deal with dexterously the inherent nonlinear behaviors of IPMC with a linearized model.

We also provide a means for system identification to improve the accuracy and reliability of IPMC actuators and sensors.

Linearization-related issues were paid much attention to characterize IPMC. However, a systematic methodology for inherent nonlinear behaviors of IPMC in this research is developed how to manage dexterously the nonlinear behaviors of IPMC with a linearized model and provides a means for system identification to improve the accuracy and reliability of IPMC actuators and sensors.

Incidentally, IPMC does not exhibit a high bandwidth for actuator applications. At high frequencies (5–20 Hz) its moduli are larger and displacements are smaller. Whereas at low frequencies mobile cations with water have time to effuse out of the surface electrodes, they are rather contained inside the base polymer (Nafion 117) at high frequencies. Therefore, the inherent behavior of water and the ion transportation within the IPMC affect the moduli differently at various frequencies [31]. Thus, using IPMC at high frequencies is disadvantageous in achieving high efficiency.

A chirp signal response offers the control of both the amplitude and the frequency range of the input [32]. The dwelling time and the frequency interval are the keys to control the degree of dynamic equilibrium [59]. We used a chirp signal input to excite the actuator in the interesting frequency range of [0.01 Hz, 5 Hz] for 40 s at a sampling frequency of 250 Hz. Fig. 4-8 shows the fast-Fourier-transform (FFT) magnitudes of the chirp signal inputs and measured outputs at the interesting frequency range. The several different magnitudes of the chirp signal shown in Fig. 4-8 (a) were applied to determine how significant the nonlinear behavior of the system would be. The parametric identification representing the system model based on the best fit of the input-output data.

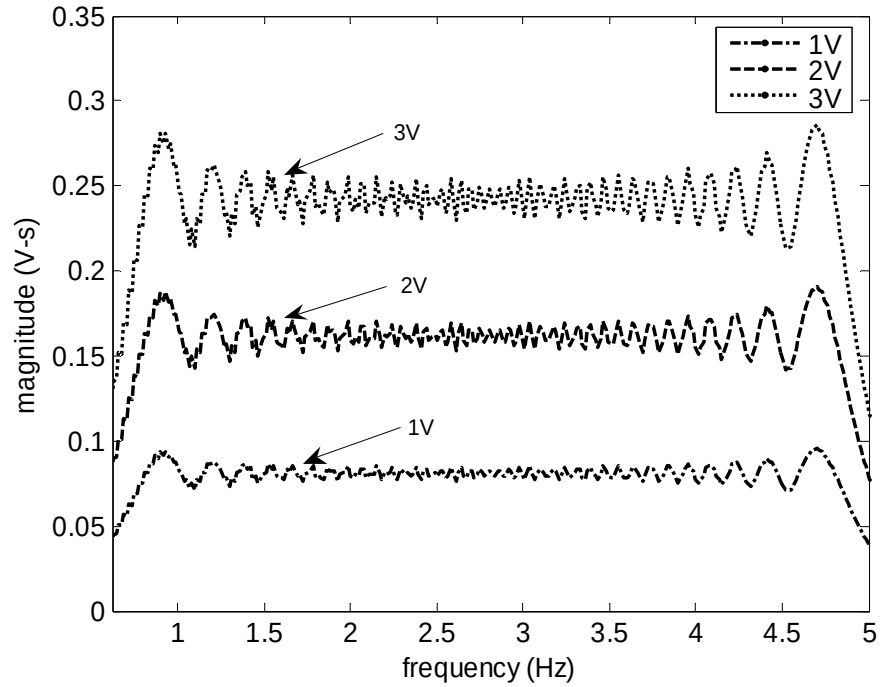

(a)

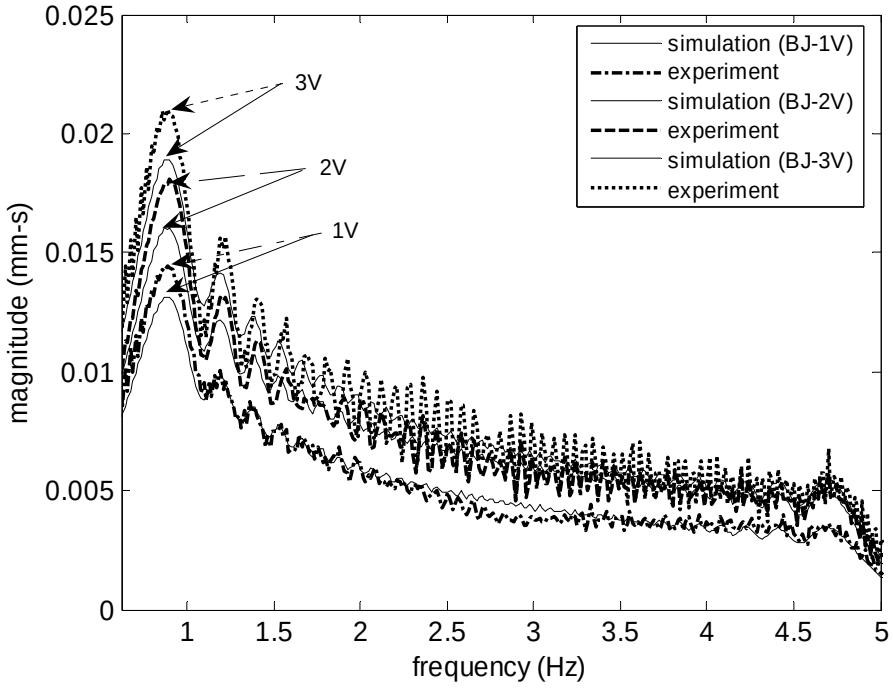

(b)

Fig. 4-8. (a) FFT magnitudes of the chirp signal inputs with three different input voltage amplitudes (1, 2, and 3 V). (b) FFT magnitudes of the measured displacements between the simulated outputs obtained using a BJ model and the experimental outputs. (c) Errors between the simulated outputs obtained using the BJ model and the experimental outputs.

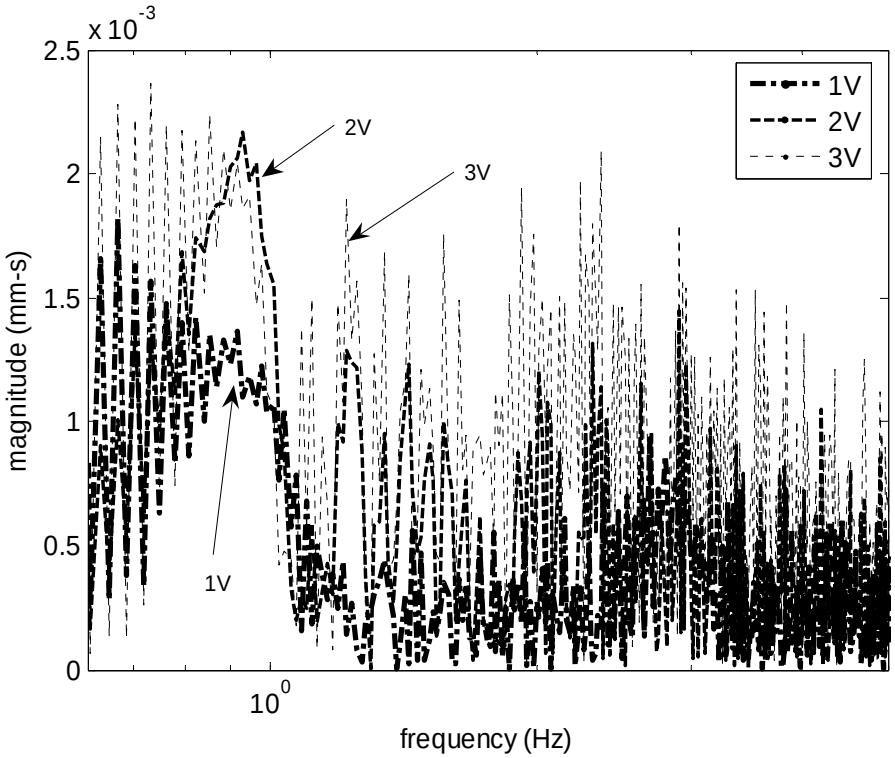

(c)

Fig. 4-8. (continued).

If the reference input has strong enough frequency components, the estimated parameters will converge in this range [58].

Bhat and Kim [62] originally employed the saturation limit of ±2 V to avoid of the integrator wind-up effect, and Yun and Kim [63] extended the saturation limit to ±3 V with an anti-windup scheme. As the nonlinear behavior in IPMC was defined due to the saturation effect [64–65], the amplitude of chirp signal input was limited to 3 V intentionally. The output magnitudes shown in Fig. 4-8 (b) decrease with respect to the frequency and also in terms of the applying voltages as expected. The frequency-domain peak magnitudes of the IPMC responses to the 3, 2, and 1 V chirp signal inputs were about 0.021, 0.0175, and 0.014 mm-s, respectively. The frequency-domain peak

magnitudes decreased by about 0.0035 mm-s as the voltage magnitudes decreased by 1 V. This phenomenon might indicate that the IPMC behavior is not highly nonlinear in this frequency range. The average magnitude errors of the chirp signal responses are approximately 0.5 μm-s as shown in Fig. 4-8 (c). Various discrete-time IPMC models acquired by BJ models are easily described by the rational transfer function $G(s)$ for the continuous-time system using numerator and denominator coefficients varying independently in prescribed intervals.

$$G(s) = \frac{n_3 s^3 + n_2 s^2 + n_1 s + n_0}{s^4 + d_3 s^3 + d_2 s^2 + d_1 s + d_0}, \tag{4-18}$$

where

$n_3 \in [1.207, 7.208]$, $n_2 \in [1906, 2299]$, $n_1 \in [2.04e+5, 9.816e+5]$, $n_0 \in [4.32e+5, 1.355e+7]$,

$d_3 \in [22.66, 500.3]$, $d_2 \in [2.068e+5, 6.805e+5]$, $d_1 \in [1.932e+6, 1.602e+7]$,

and $d_0 \in [5.109e+5, 3.266e+7]$.

Another way to find the transfer function of the IPMC is using the power-spectral density (PSD) analysis with the relationship

$$\Phi_{yy}(\omega) = |W(j\omega)|^2 \Phi_{xx}(\omega), \tag{4-19}$$

where $\Phi_{xx}(\omega)$ and $\Phi_{yy}(\omega)$ are the power-spectral densities of the input and the output, respectively, and $W(j\omega)$ is the system transfer function [64]. Each Bode plot of the

transfer function shown in Fig. 4-9 exhibits a similar trend in the characteristics of the system. We consider the system transfer function only below 5 Hz, which is the interesting frequency range.

Fig. 4-10 shows that the Bode plots of the system transfer function (solid lines) obtained from the PSD analysis and those from the BJ model (dashed lines) match very well within the interesting frequency range. Fig. 4-10 (a), (b), and (c) represent the cases of the magnitudes of the chirp signal inputs of 1, 2, and 3V, respectively. From the plots shown in Fig. 4-10, we conclude that the IPMC characteristics closely follow the linear BJ model in this frequency range.

Simulation and cross-validation are needed to test whether a model can reproduce the observed output when driven by the actual input. Since different structures can yield quite distinct models, a number of different structures must be tried out and the properties of the models' compared. The percentage data of the comparison gives a good indication whether the identified model captured the dominating dynamics of the true system or not. Cross-validation is probably an important indication of the validation tests since it shows how well the obtained model can represent the true plant. The parametric models can be validated in a variety of ways. Other validation tests can be pole-zero location, Bode plot, and residual analysis [55, 57]. After investigating the fit between the model's simulated output and the measured one for the validation data using the method of model structure selection in Subsection 4.1.1., we can pick that model with the highest percentage from the following reasons. The higher percentage represents the more the system information

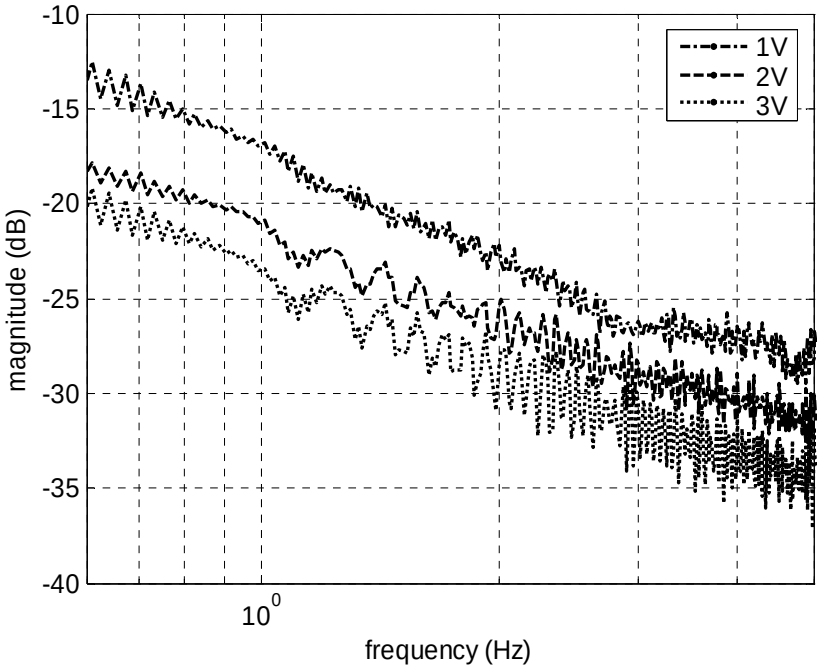

Fig. 4-9 Bode plots of the transfer function using a PSD analysis.

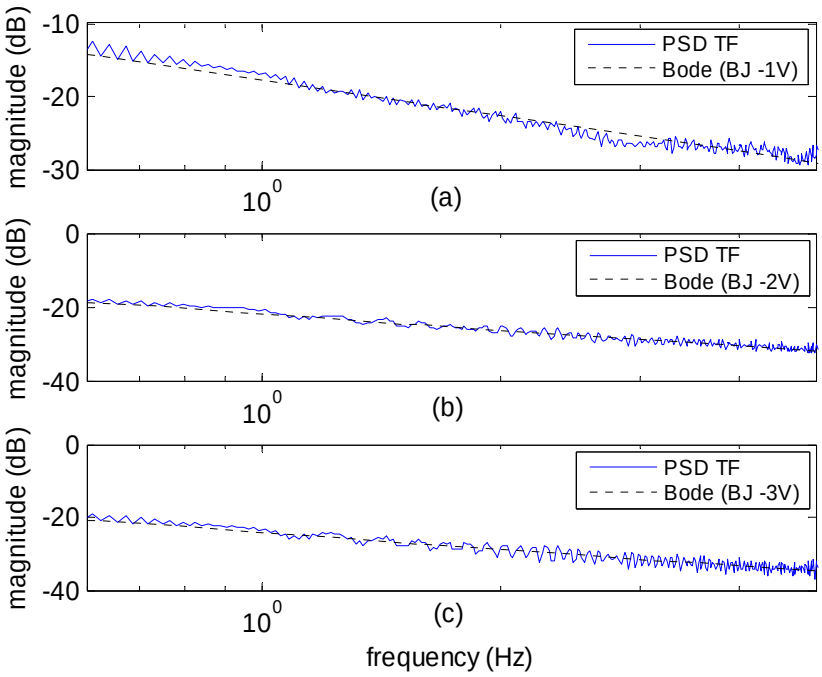

Fig. 4-10. Comparison of the Bode plots of the transfer function obtained from the PSD analysis (solid lines) with those from the BJ model (dashed lines). (a), (b), and (c) represent the cases of the amplitudes of the chirp signal inputs of 1, 2, and 3 V, respectively.

can be captured. The candidate estimated model is also required to have a valid FFT magnitude analysis test in terms of the linearized model we claimed previously. After numerous trial and errors, BJ model was the best candidate for the system identification and model structures of IPMCs were selected 3rd and 4th orders to represent the characteristic of IPMCs for the position.

Fig. 4-11 shows the example of the comparison of the measured input with the BJ model's output in response to the chirp signal from 0.01 to 5 Hz using the sample, IPMC 1. These well-matched responses demonstrate the accuracy of the model at the same as the EAP case in Fig. 4-7. The several different magnitudes of the chirp signal shown in Fig. 4-11 were applied. The comparison of the measured output with the fourth-order BJ

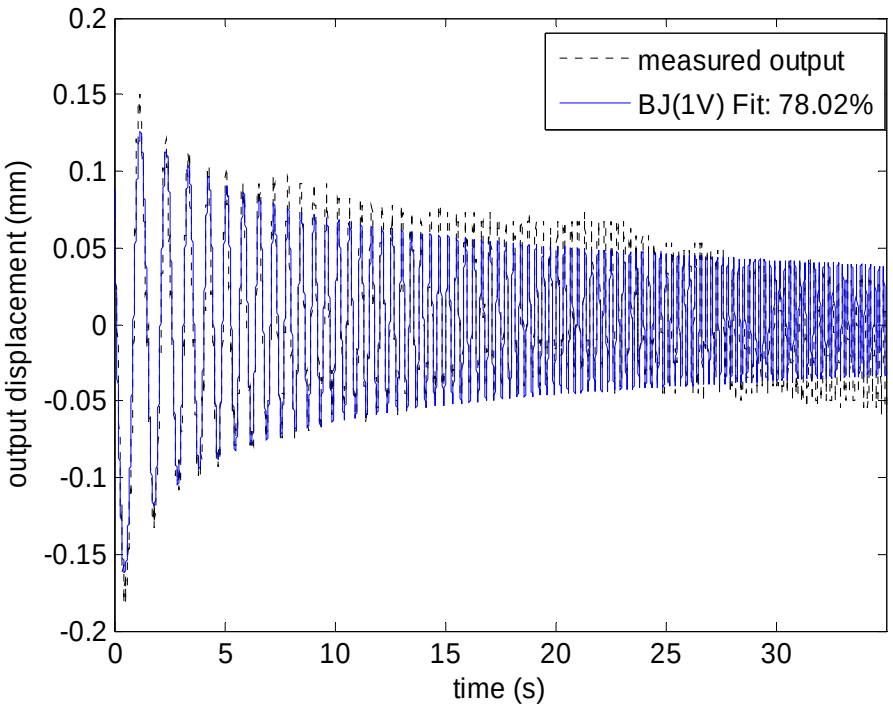

(a)

Fig. 4-11. Comparison of the measured output (dotted line) with the BJ model output (solid line) in response to the chirp signal. (a), (b), and (c) represent the cases of the amplitudes of the chirp signal inputs of 1, 2, and 3 V, respectively.

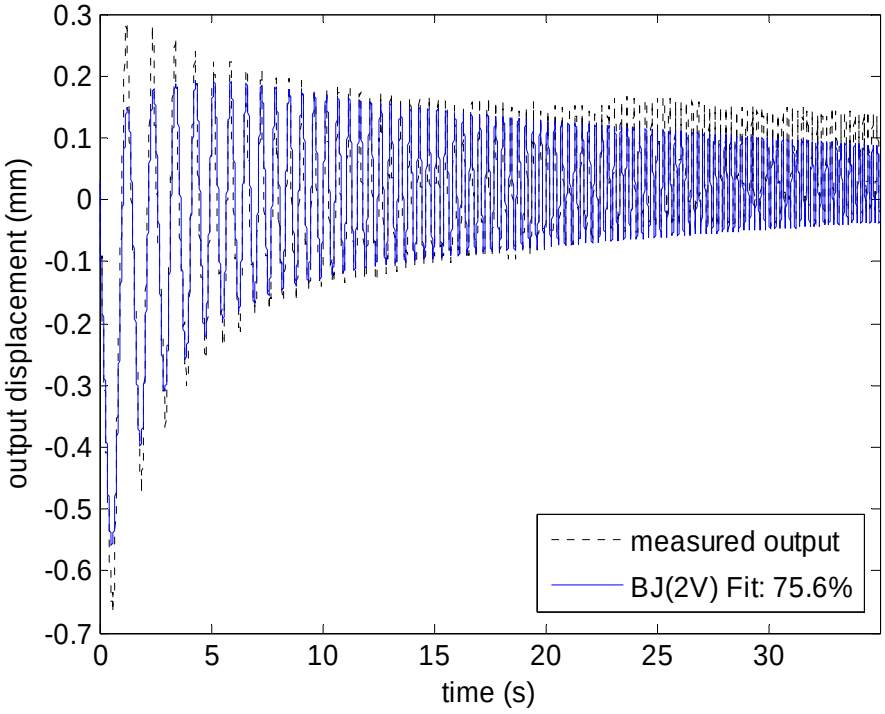

(b)

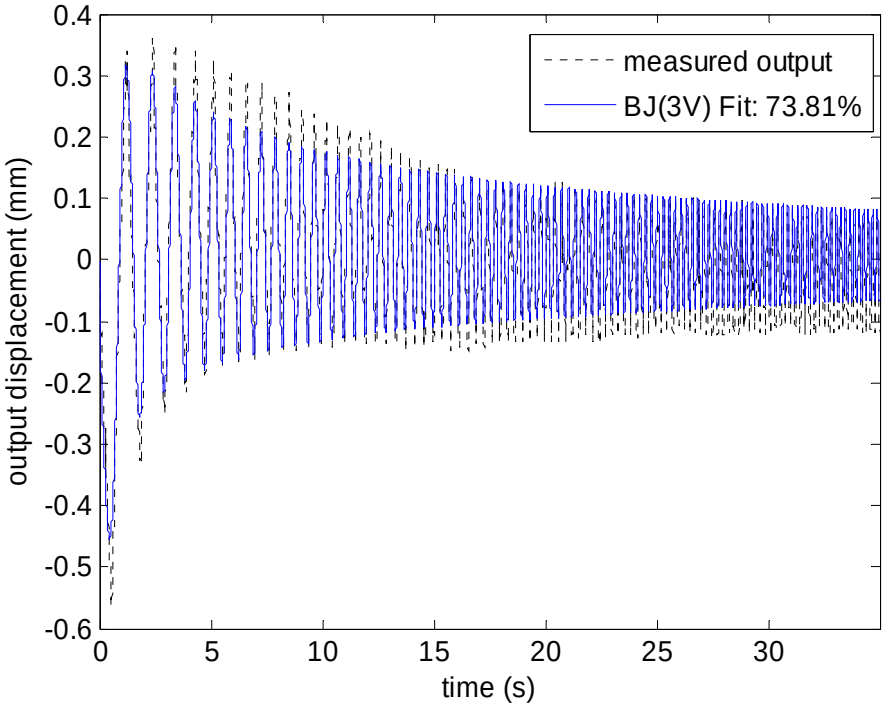

(c)

Fig. 4-11. (Continued).

model output in response to the chirp signal input was shown in Fig. 4-11. From the cross-validation, the percentages of the matched BJ models were 78.02%, 75.6%, and 73.81%, respectively.

However, it may be possible to achieve a better correlation between the simulated and measured outputs in the cross-validation test by using the residuals in the simulation. The reason is that not only the dynamic part of the model but the noise model was taken into consideration in the simulation.

The residuals should not be correlated with the system's input, and the cross correlation function between the residuals and the input does not go significantly beyond the confidence region.

$$R_1(\tau) = \frac{1}{N}\sum_{t=1}^{N} \varepsilon(t)u(t-\tau) \tag{4-20}$$

$$R_2(\tau) = \frac{1}{N}\sum_{t=1}^{N} \varepsilon(t)\varepsilon(t-\tau), \tag{4-21}$$

where $\tau = n_k, n_k+1, \ldots, n_k+n_b-1$. The residual ε is the difference between the measured output and the simulated output, $R_1(\tau)$ is the covariance between the residuals and the past input. $R_2(\tau)$ is the correlation among the residuals themselves. Fig. 4-12 shows model validation of the BJ models using validation data. Dashed lines denote confidence intervals. The functions are displayed up to lag *M*, which was set to be 6 in Matlab command, *RESID*.

For a good model, the residuals should be independent of the input. Otherwise, there would be more in the output that originates from the input and that the model has not picked up. To test this independence, the cross-correlation function between the input and the residuals was computed by checking the model residuals. The confidence interval which is shown dashed-lines in Fig. 4-12 was also displayed for this function. For an ideal model the correlation function should lie entirely between the confidence lines for positive lags. If, for example, there is a peak outside the confidence region for lag *M*,

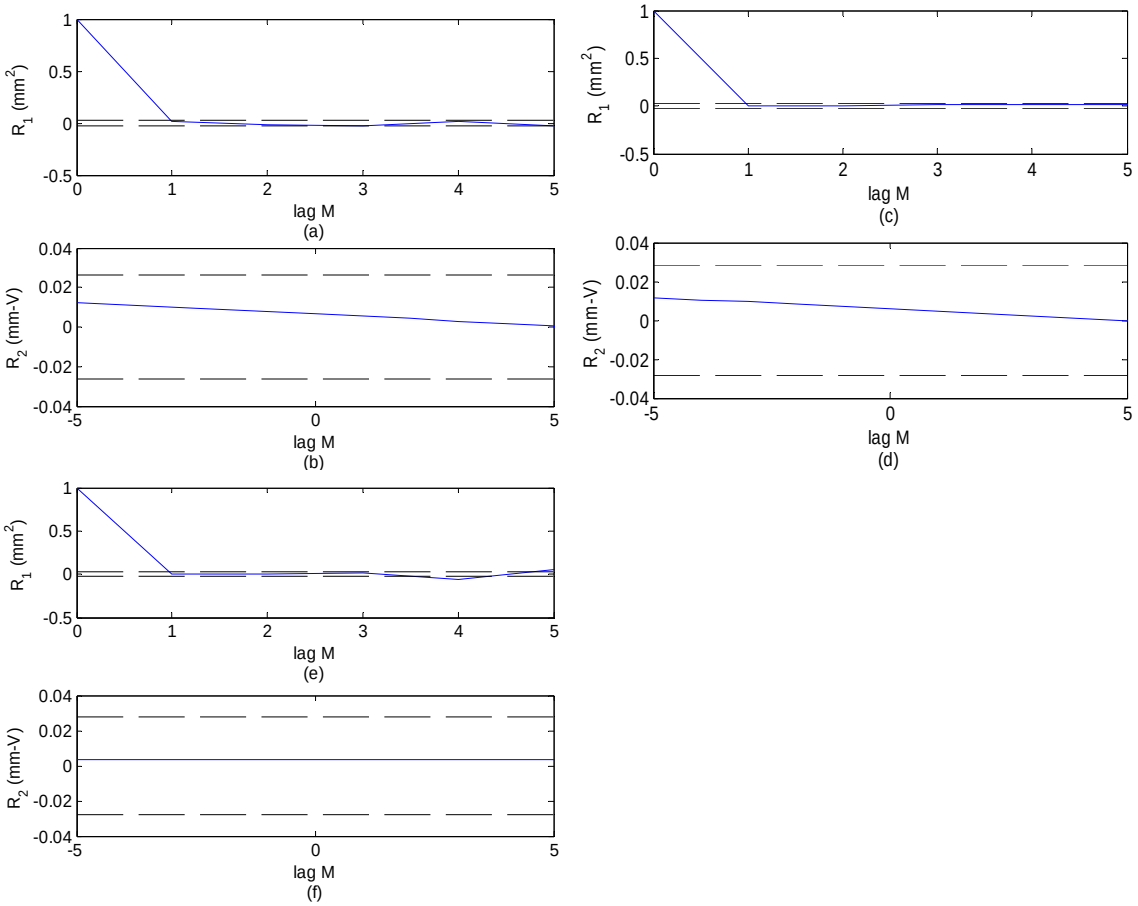

Fig. 4-12. Conventional residual analysis correlation functions for the position models of IPMC 1, 2, and 3. (a) Correlation functions of residuals and (b) cross-correlation functions between the input and the residuals from the output of the IPMC model 1. (c) and (d) of IPMC 2. (e) and (f) of IPMC 3.

there is something in the output $y(t)$ that originates from $u(t-\tau)$ and that has not been properly described by the model. The residual analysis test is carried out using the validation data. As shown in Fig. 4-12, the auto-correlation R_1 and the cross-correlation R_2 are within the confidence intervals which represent the reliable model error.

Three discrete-time IPMC transfer functions representing open-loop position responses acquired by the fourth-order BJ models are as followed.

$$G_{1p}(z)=\frac{0.4995\,z^3-1.496\,z^2+1.515\,z-0.5171}{z^4-1.579\,z^3+1.344\,z^2-1.252\,z+0.4918}$$

$$G_{2p}(z)=\frac{0.2338\,z^3-0.6801\,z^2+0.6718\,z-0.2249}{z^4-0.3604\,z^3-1.22\,z^2-0.07111\,z+0.6537} \tag{4-22}$$

$$G_{3p}(z)=\frac{-0.0755\,z^2+0.1973\,z-0.1168}{z^3-0.495\,z^2-0.2224\,z-0.2604}$$

The pole and the zero locations of the system transfer functions are summarized in Table 4-1.

Table 4-1. Pole-zero locations of the system models of IPMCs.

	IPMC 1	IPMC 2	IPMC 3
Poles	– 0.0210 + 0.8877i – 0.0210 – 0.8877i 0.9929 0.6281	– 0.7577 + 0.4146i – 0.7577 – 0.4146i 0.9943 0.8814	0.98736 – 0.24618 + 0.4507i – 0.24618 – 0.4507i
Zeros	1.0277 + 0.2136i 1.0277 – 0.2136i 0.9396	0.9784 + 0.2304i 0.9784 – 0.2304i 0.9521	1.7069 0.90632

The position model for the IPMC finger 3 has the third-order since this has a better cross-validation than the fourth-order BJ model. Although we cut the IPMC membrane to make the same size of the IPMC fingers by hands, but there might have an inaccuracy for the size of the IPMC fingers. Therefore, they can not exactly represent the same behaviors. The subscript in (4-22) implies each IPMC.

The open-loop Bode plots of the force models given in (4-22) are shown in Fig. 4-13. The open-loop Bode plots show 40.1°, 180°, and infinity phase margins.

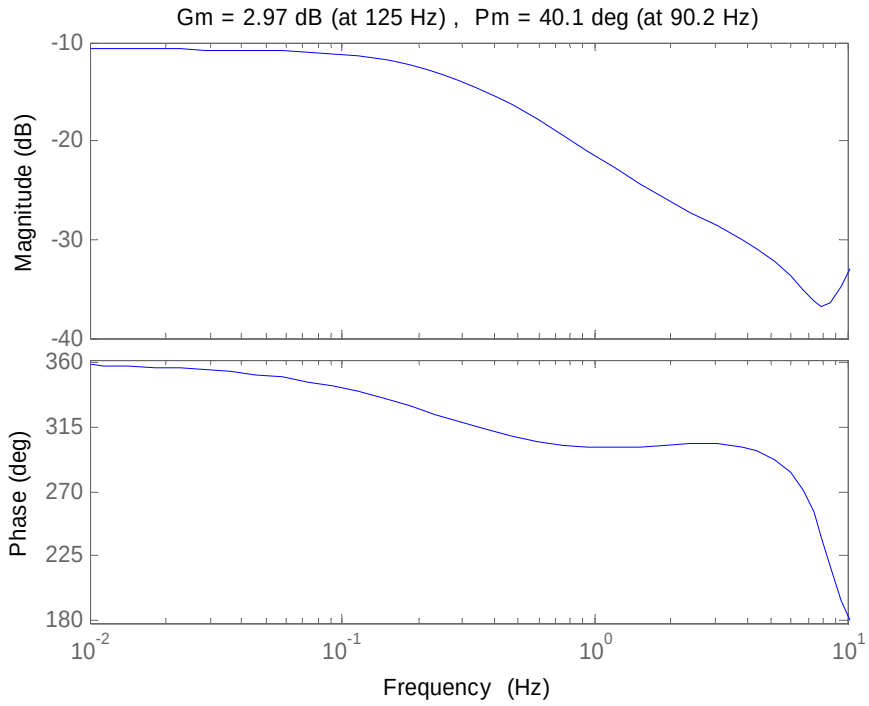

(a)

Fig. 4-13. Open-loop Bode plots of the position models for (a) IPMC 1, (b) IPMC 2, and (c) IPMC 3.

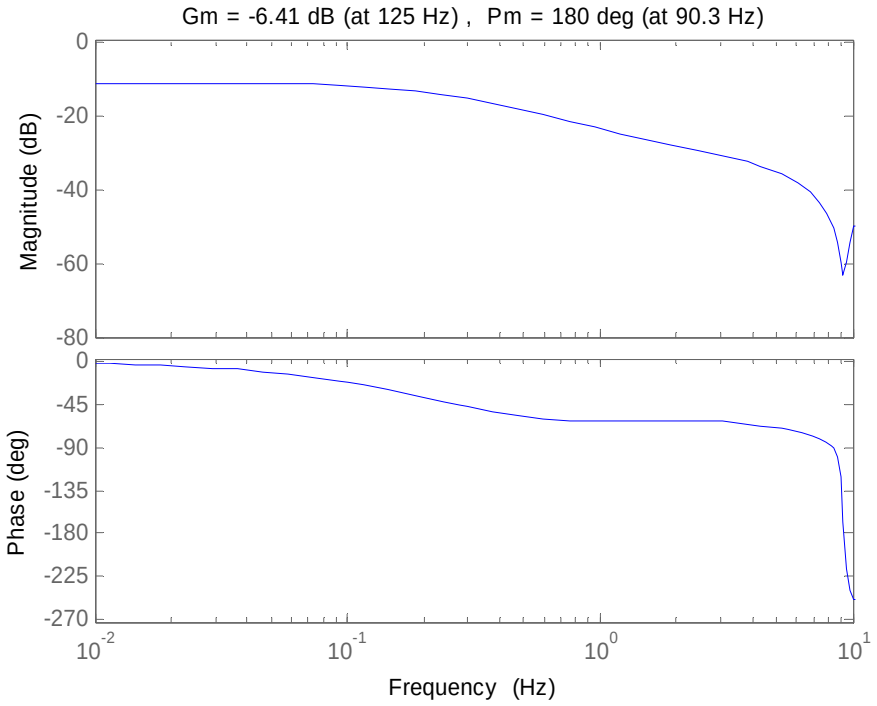

(b)

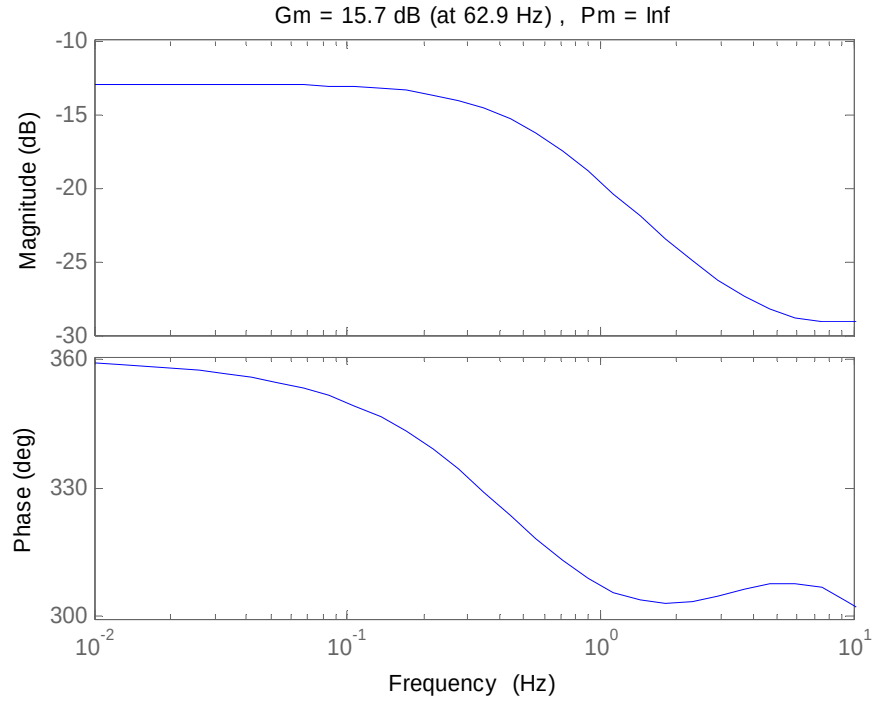

(c)

Fig. 4-13. (Continued).

For comparison, a band-limited white noise (BLWN), the noise power was set to 0.01 dBW with seed [23341] in Simulink® was used to compare with the PSD analysis (solid line) with a chirp input signal in Fig. 4-14 (a). A pseudo-random binary sequence (PRBS) [55, 57] was used to re-find the transfer function, and the three Bode plots including BLWN plot (dashed line) were shown in Fig. 4-14 (b). The Bode plot (dashdot line) from using a PRBS matches well with that from the PSD analysis with a chirp input signal and BLWN. From the result of PSD analyses, each Bode plot of the transfer functions shown in Figs. 4-14 (a) and (b) exhibit similar trends in the characteristics of the system.

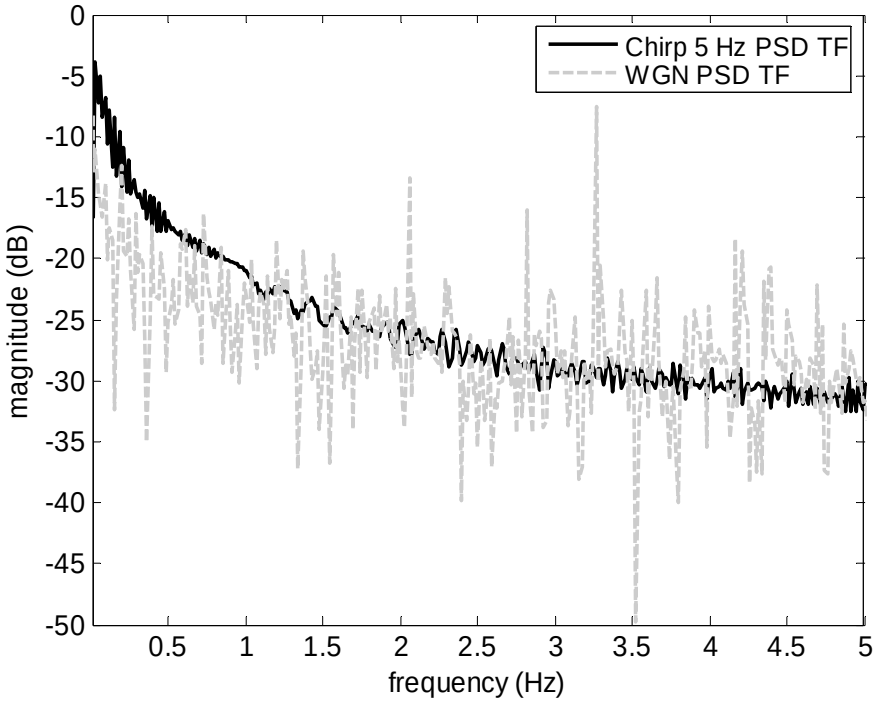

(a)

Fig. 4-14. (a) Comparison of Bode plots from the PSD analysis for the 2-V BJ model with the PSD analysis from the WGN. (b) Comparison of Bode plots of the PSD analysis from the BJ model with the PSD analysis from PRBS and WGN.

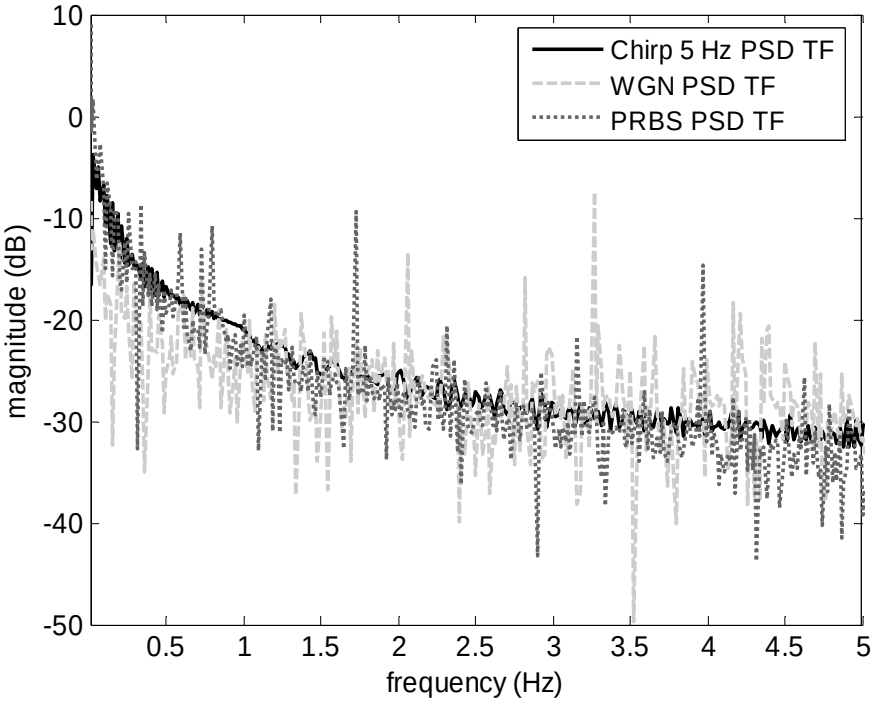

(b)

Fig. 4-14. (Continued).

4.3 Force-Transduction Models

In this section the system identification of EAP and IPMC modeling is presented in terms of force. The methodology of the system identification is the same as the position case except the measured force output from the actuators. The inherent behavior of EAP and IPMC is discussed based on the modeling.

4.3.1 Open-Loop Force Response of EAP

After various cross-validation for the model structure, the fourth-order BJ model for EAP actuator. The discrete-time EAP acquired by BJ models are as follows.

$$G_f(z)=\frac{9.4\times10^{-4}\,z^3-2.902\times10^{-3}\,z^2+3.013\times10^{-3}\,z-1.05\times10^{-3}}{z^4-1.51\,z^3+0.09429\,z^2+0.6785\,z-0.2599} \qquad (4\text{-}23)$$

The pole and the zero locations of the system transfer function are summarized in Table 4-2.

Table 4-2. Pole-zero locations of the system model of EAP.

	EAP
Poles	–0.6761, 0.9915, 0.5973 + 0.1760i, 0.5973 – 0.1760i
Zeros	1.0614 + 0.1777i , 1.0614 – 0.1777i , 0.9642

The comparison of the measured output with the fourth-order BJ model output in response to the chirp signal input was shown in Fig. 4-15. From the cross-validation, the percentage of the matched BJ model was 79.37%. The auto-correlation R_1 and the cross-correlation R_2 are also within the confidence intervals as shown in Fig. 4-16. Fig. 4-17 shows Bode plots of the open-loop force model for EAP.

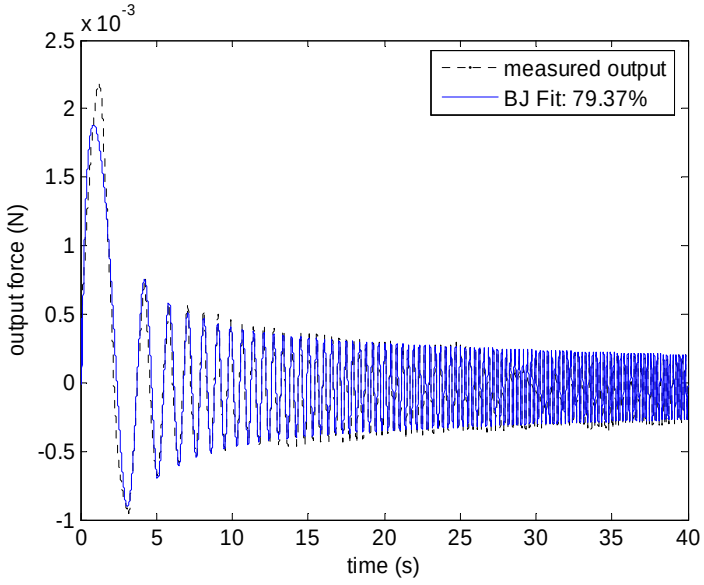

Fig. 4-15. Comparison of the measured output (dotted line) with the BJ model output (solid line) in response to the chirp signal. The measured output represents the amplitude of the chirp signal input of 3V with EAP.

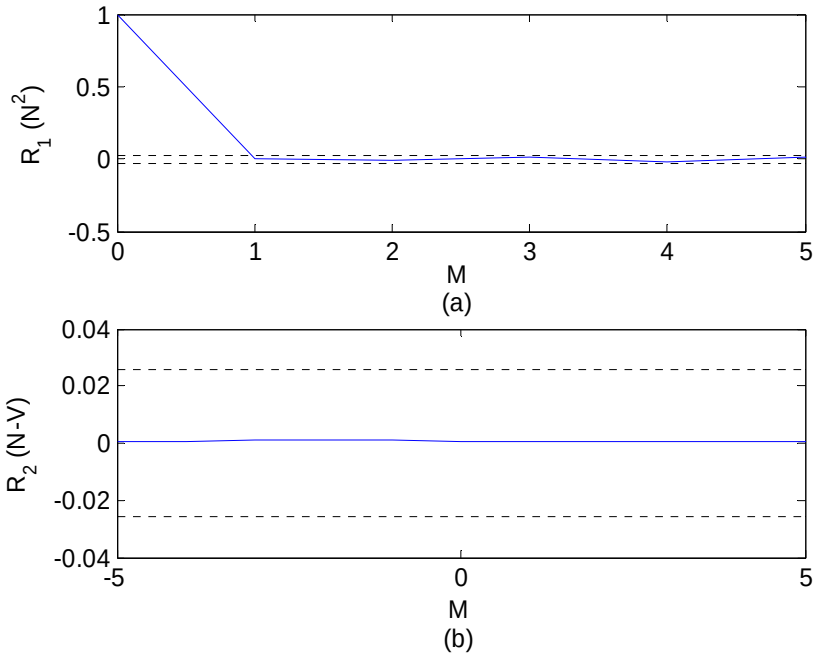

Fig. 4-16. Conventional residual analysis correlation functions for the force model of EAP. (a) Correlation function of residuals and (b) cross-correlation function between the input and the residuals from the output of the EAP.

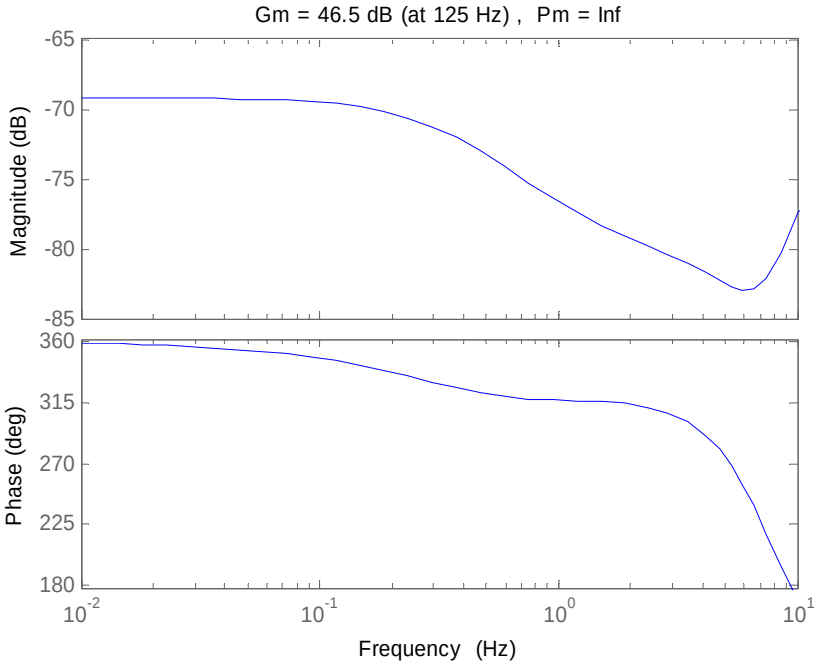

Fig. 4-17. Open-loop Bode plots of the force model for EAP.

Fig. 4-18 shows the fast-Fourier-transform (FFT) magnitudes of the chirp signal inputs and the measured force outputs at the interesting frequency range for the EAP actuator. The several different magnitudes of the chirp signal shown in Fig. 4-18 (a) were applied to determine how significant the nonlinear behavior of the system would be as we performed in the position system in Fig. 4-8. The output magnitudes shown in Fig. 4-18 (b) also decrease with respect to the frequency and also in terms of the applying voltages as expected. The frequency-domain peak magnitudes of the IPMC responses to the 3, 2, and 1 V chirp signal inputs were about 0.287, 0.182, and 0.148 mN-s, respectively at 0.1 Hz. The frequency-domain peak magnitudes decreased by about 0.1 mN-s as the voltage magnitudes decreased by 1 V.

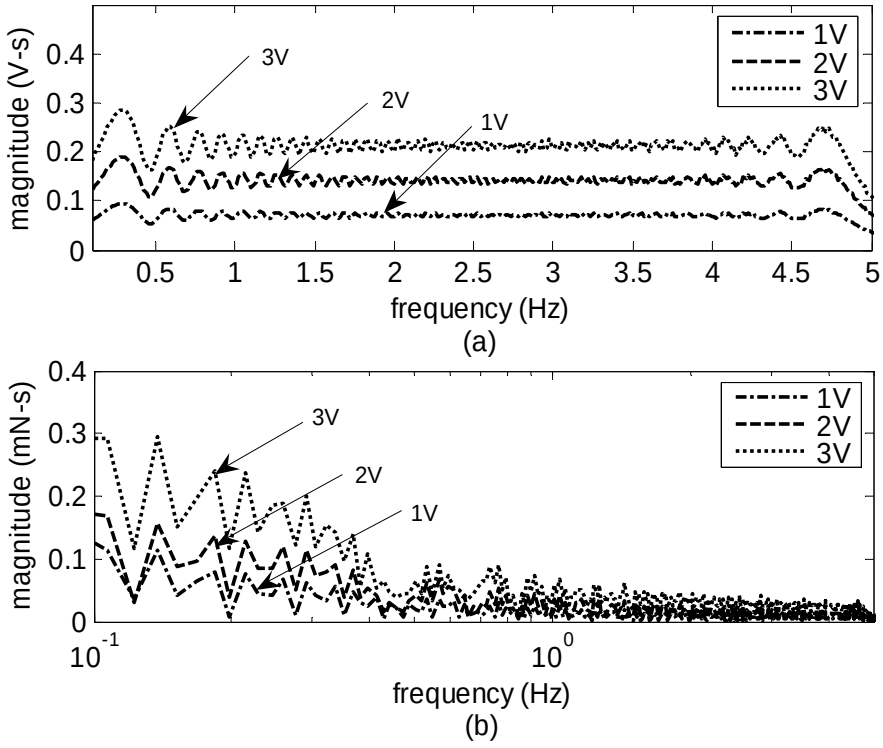

Fig. 4-18 (a) FFT magnitudes of the chirp signal inputs with three different input voltage amplitudes (1, 2, and 3 V). (b) FFT magnitudes of the measured forces between the simulated outputs obtained using a BJ model and the experimental outputs.

4.3.2 Open-Loop Force Response of IPMC

The procedure of the force system identification is the same as the case of the position system identification. Note that the load cell can only measure the blocked force; therefore we initially need to contact the tip of the load cell with the IPMC strip before applying the chirp signal voltage. To compensate for the offset due to this initial loading, we subtracted the initial contact force in this figure. This might have caused the loss of the system information since the percentages of the force models turned out to be lower than those of the position models. After performing the similar routine except sensing the

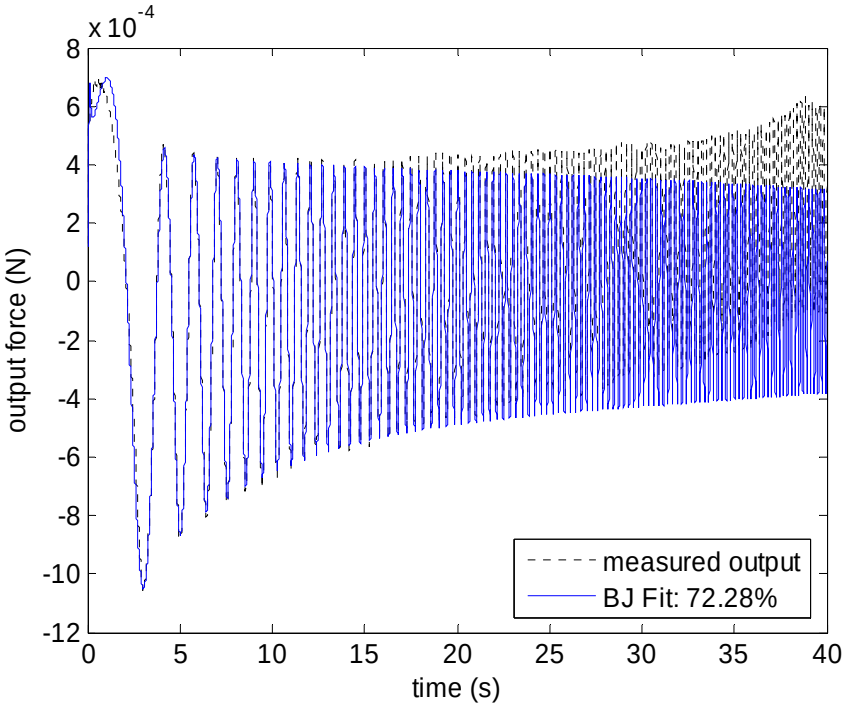

(a)

Fig. 4-19. Comparison of the measured output (dotted line) with the BJ model output (solid line) in response to the chirp signal. (a), (b), and (c) represent the cases of the amplitudes of the chirp signal input of 1V with IPMC Fingers 1, 2, and 3, respectively.

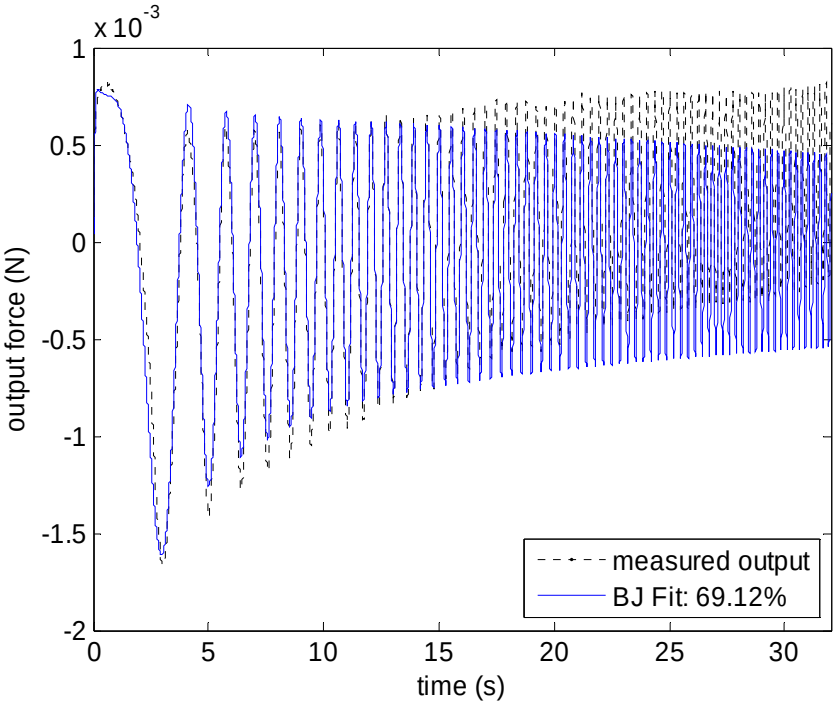

(b)

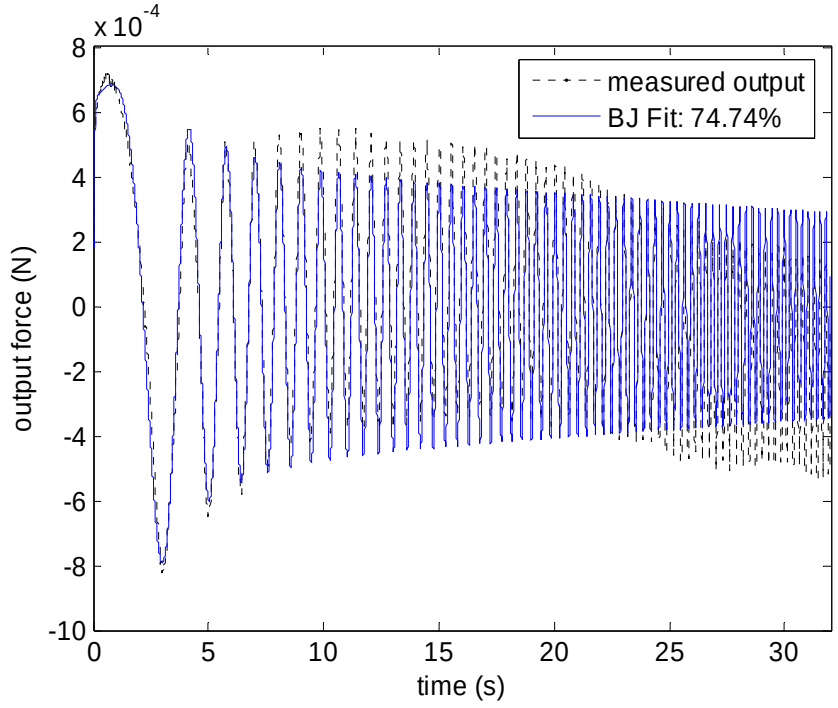

(c)

Fig. 4-19. (Continued).

blocked force measured from the load cell. The comparison of the measured force output with the third- and fourth-order BJ model output in response to the 1V chirp signal input from 0.01 to 5 Hz in the frequency range of 0.01 to 5Hz. From the cross-validation, the percentages of the matched BJ models were 72.28%, 69.12%, and 74.74%, respectively as shown in Fig. 4-19. The model structure of IPMC Finger 2 was selected to the third-order model since the percentage of the fourth-order model from the cross-validation is 66.71% which is less than the third-order case. The case of IPMC Finger 3 has the same reason since the fourth-order BJ model has a lower percentage, 66.71%.

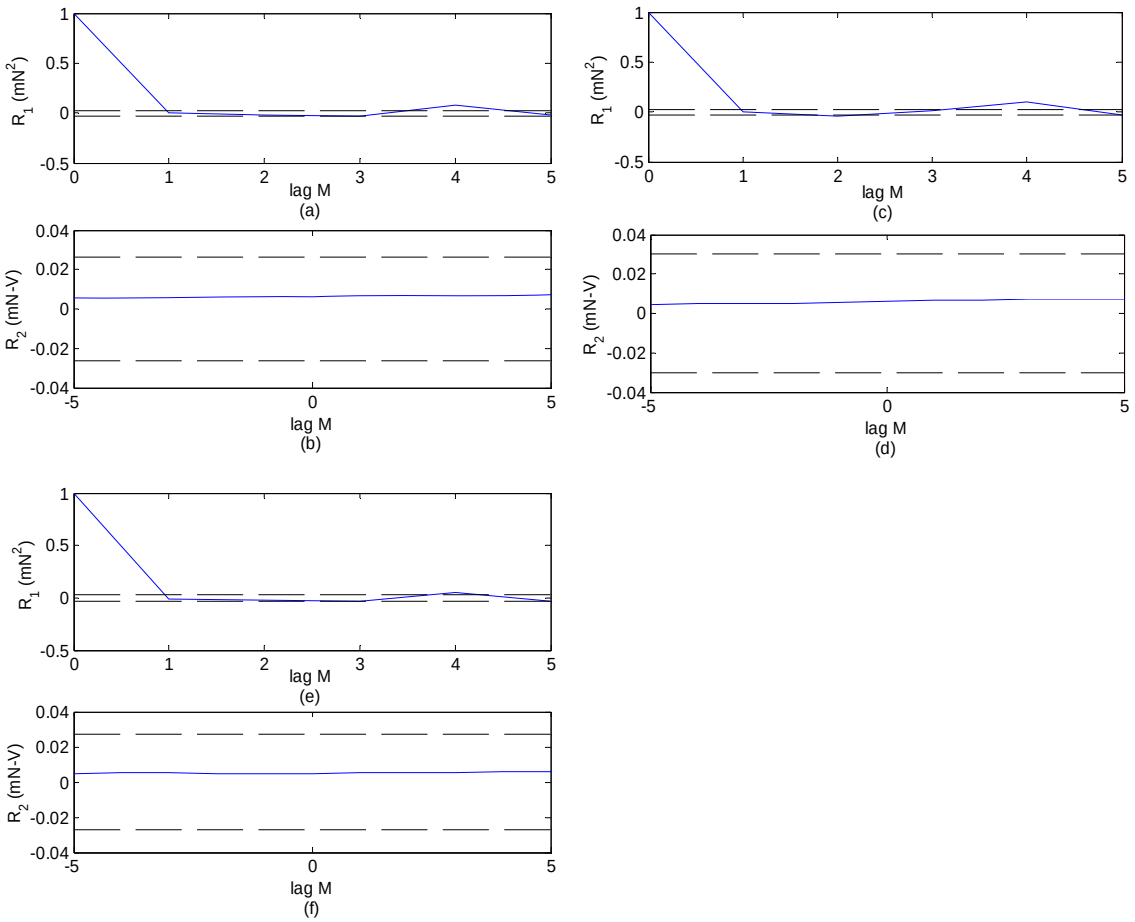

Fig. 4-20. Conventional residual analysis correlation functions for the force models of IPMC 1, 2, and 3. (a) Correlation functions of residuals and (b) cross-correlation functions between the input and the residuals from the output of the IPMC model 1. (c) and (d) of IPMC 2. (e) and (f) of IPMC 3.

Fig. 4-20 shows the model validation of the BJ force models for the IPMC Fingers 1, 2, and 3. Although there are small peaks of the auto-correlation R_1 slightly beyond the confidence intervals in the lag M=4, the residual errors do not significantly affect the past residual errors. Therefore, the model error information from validation data is reliable.

Fig. 4-21 shows the fast-Fourier-transform (FFT) magnitudes of the chirp signal inputs and the measured force outputs at the interesting frequency range for IPMC Finger 1. 1, 1.5, and 2V magnitudes of the chirp signal shown in Fig. 4-21 (a) were applied since the load cell has a limited sensing range which can measure only below 6 mN. If we apply more than 2V, the data will be destroyed. This affects the significant reduction on the output magnitude in the FFT plot. The frequency-domain peak magnitudes of the IPMC responses to the 3, 2, and 1 V chirp signal inputs were about 0.5, 0.28, and 0.148 mN-s, respectively at 0.1 Hz. The frequency-domain peak magnitudes decreased by about 0.1 mN-s as the voltage magnitudes decreased by 1 V. After 1 Hz, the magnitudes become similarly smaller due to the fact that water and hydrated ions do not have enough time to emit out of the surface electrodes. At high frequencies above 5Hz, they are rather contained inside the polymer [31]. This phenomenon can also indicate that the IPMC behavior is not highly nonlinear in this frequency range.

Three discrete-time IPMC transfer functions of IPMC Fingers representing open-loop force responses acquired by the third- and the fourth-order BJ models are as followed.

$$G_{1f}(z)=\frac{1.659\times10^{-5}\,z^3-3.906\times10^{-5}\,z^2+2.89\times10^{-5}\,z-6.432\times10^{-6}}{z^4-3.726\,z^3+5.212\,z^2-3.245\,z+0.759}$$

$$G_{2f}(z) = \frac{6.245\times10^{-5}\, z^2 - 1.006\times10^{-4} z + 3.863\times10^{-5}}{z^3 - 2.55\, z^2 + 2.137 z - 0.5873} \tag{4-24}$$

$$G_{3f}(z) = \frac{9.17\times10^{-6}\, z^2 - 4.118\times10^{-6} z - 4.802\times10^{-6}}{z^3 - 2.594\, z^2 + 2.225 z - 0.6308}$$

The reason for the third-order force models for the IPMC finger 2 and 3 is the same as the position model's case. The pole and the zero locations of the system transfer functions are summarized in Table 4-3.

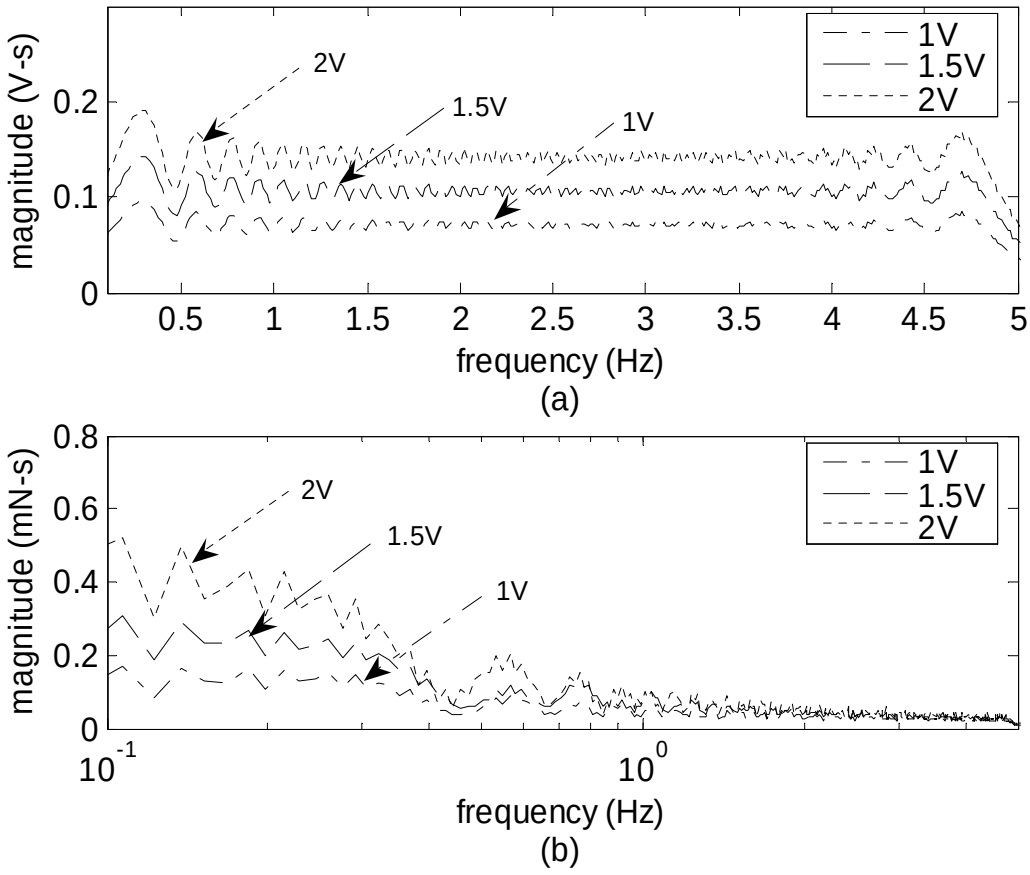

Fig. 4-21 (a) FFT magnitudes of the chirp signal inputs with three different input voltage amplitudes (1, 1.5, and 2 V). (b) FFT magnitudes of the measured forces between the simulated outputs obtained using a BJ model and the experimental outputs.

Table 4-3. Pole-zero locations of the system models of IPMCs.

	IPMC 1	IPMC 2	IPMC 3
Poles	0.9954 0.9718 0.8795 + 0.1053i 0.8795 – 0.1053i	0.9892 0.9031 0.6574	0.9919 0.8780 0.7243
Zeros	0.9912 0.9522 0.4108	0.9782 0.6323	0.9822 –0.5331

The open-loop Bode plots of the force models given in (4-21) are shown in Fig. 4-22. The open-loop Bode plots show infinity phase margins.

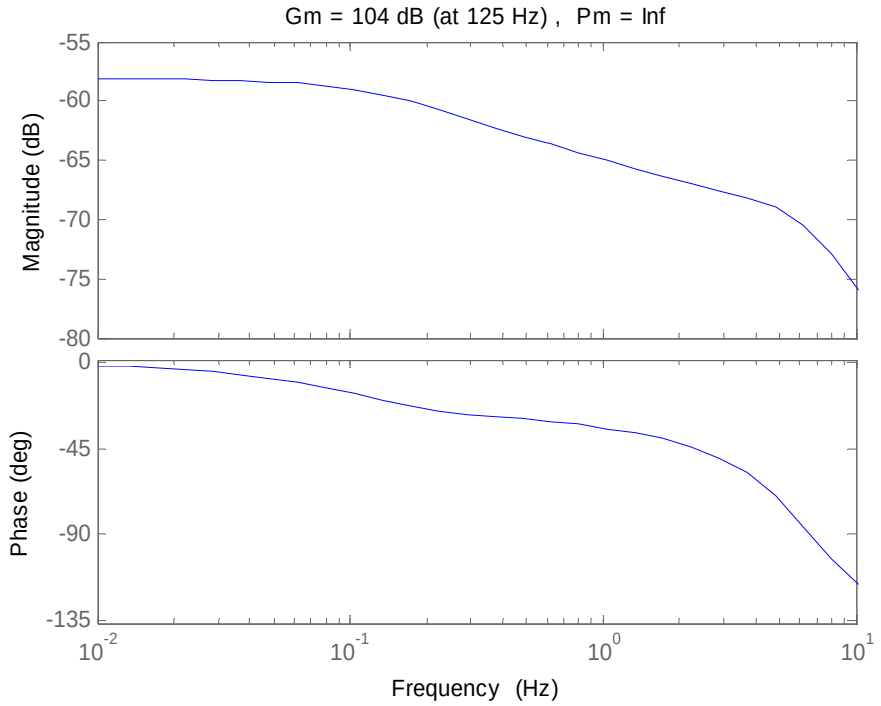

(a)

Fig. 4-22. Open-loop Bode plots of the force models for (a) IPMC 1, (b) IPMC 2, and (c) IPMC 3.

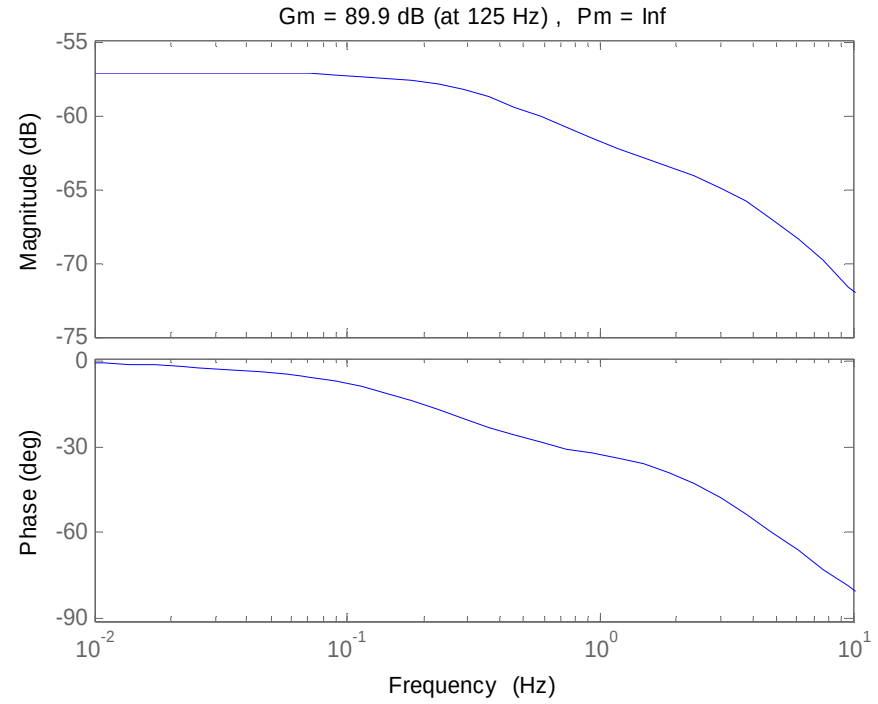

(b)

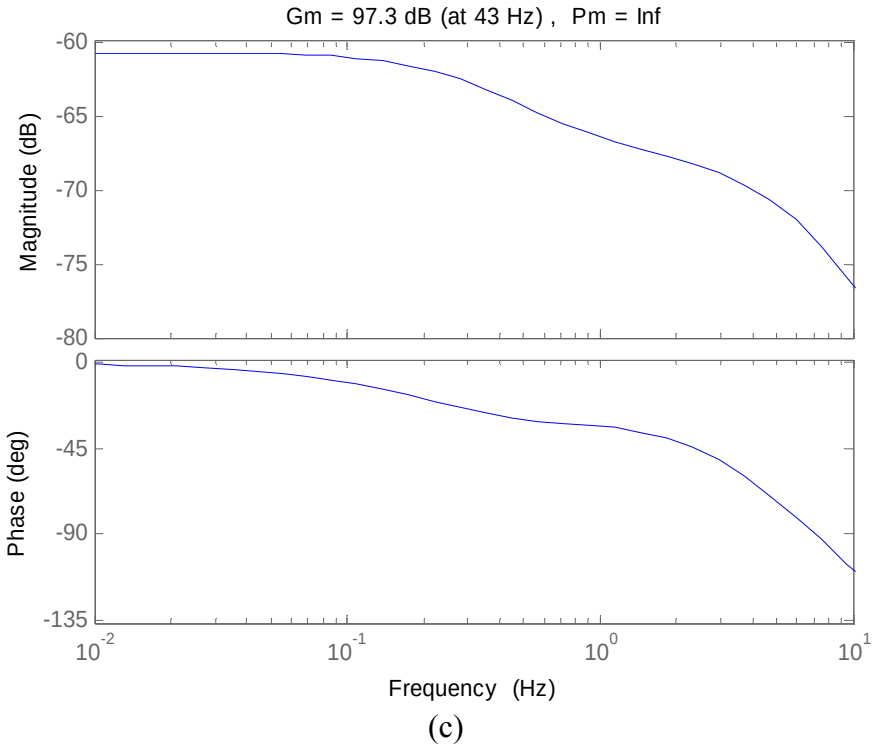

(c)

Fig. 4-22. (Continued).

CHAPTER V

CLASSICAL AND OPTIMAL CONTROL

In this chapter the control system design based on the modeling in chapter IV is presented. Various position and force tests are performed that demonstrate the capabilities of the EAP and IPMC actuators.

5.1 Modified Proportional-Integral-Derivative Controller Design for EAP

The control objectives in this research are (1) to have a 60° phase margin, (2) to follow step position commands with no steady-state error, and (3) to minimize the settling time. To achieve these control objectives, a discrete proportional-integral-derivative (PID) controller was designed for the EAP actuator. The discrete PID compensator with the bilinear (Tustin) transformation can be written as follows [65]:

$$\frac{\left(K_P + \frac{2K_D}{T_S}\right)z^2 + \left(K_I T_S - \frac{4K_D}{T_S}\right)z + \left(-K_P + K_I T_S + \frac{2K_D}{T_S}\right)}{z^2 - 1}, \qquad (5\text{-}1)$$

where T_S, K_P, K_I, and K_D are the sampling period of the discrete-time system, and the proportional, integral, and derivative gains, respectively. The proportional-integral (PI) term is necessary to meet the zero steady-state-error requirement. The proportional-derivative (PD) term is used to reduce the overshoot and to accelerate the system. The PI and PD corner frequencies were calculated with a pole-zero cancellation method. The parameter values were calculated from the comparison of (5-1) with a second-order

transfer function (5-2).

$$C(z) = k_c \frac{(z - p_{d1})(z - p_{d2})}{z^2 - 1}, \tag{5-2}$$

where k_c is calculated to set the 60° phase margin with a crossover frequency of 0.171 Hz, and p_{d1} and p_{d2} are poles of the plant model in (4-17). If poles are close to the origin, the system response will be slower. Therefore, to cancel poles close to the origin will enhance the tracking performance. The values of the matching parameters of the controller from (5-1) and (5-2) are given in Table 5-1.

Table 5-1. List of parameter values used for experiments.

$T_S = 0.004$ s	$p_{d1} = -0.9583$
$K_P = 0.64894$ V/mm	$p_{d2} = 0.9279$
$K_I = 11.68817$ V/mm·s	$K_a = 0$ mm/V (without the anti-windup scheme)
$K_D = 0.00003$ V·s/mm	$K_a = 50$ mm/V (with the anti-windup scheme)
$k_c = 0.66225$ V/mm	

Fig. 5-1 shows a Simulink Real-Time Workshop schematic diagram for closed-loop digital position control of the EAP actuator with an integrator anti-windup scheme. The controller includes an anti-windup term which reduces the degradation in the system

performance due to actuator saturation. The anti-windup gain K_a needs to be large enough that the anti-windup scheme can keep the control effort by the integrator small [65]. The purpose of the saturation block in the Simulink block diagram is to prevent the excessive control voltage from being applied to the EAP actuator. The control voltage was limited to ±7 V to avoid permanently damaging the EAP strip. The actual hardware EAP actuator and sensor is present in the box represented as "Plant".

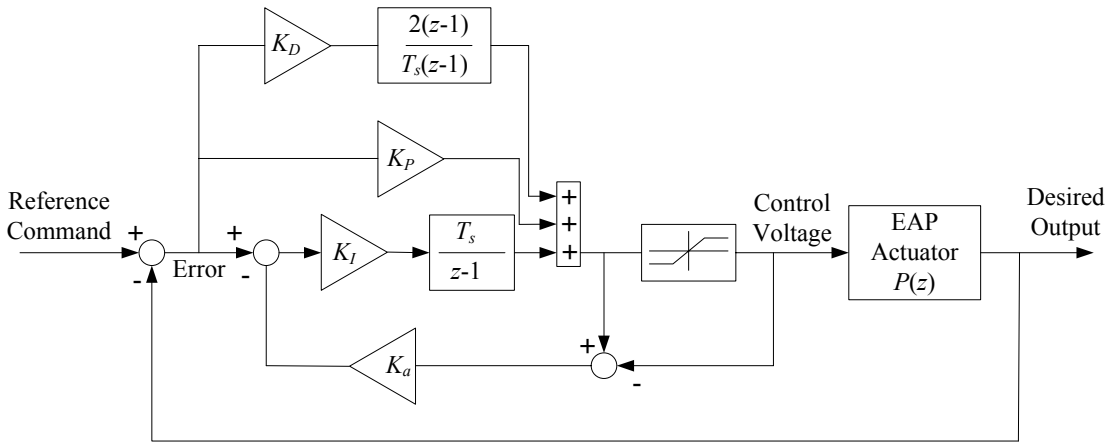

Fig. 5-1. Schematic diagram of the closed-loop position control of the EAP actuator.

5.2 Simulation and Experimental Results of EAP

5.2.1 Simulated 0.8-mm Step Response

Fig. 5.2 shows the anti-windup scheme using a modified PID controller and simulation results of the EAP actuator's closed-loop tracking performance were presented in Fig. 5-3. The dotted line from Fig. 5-3 (a) indicates the system response without the saturation block and Fig. 5-3 (b) shows how much the control voltage was applied to the system. A dash-dotted line demonstrates the effect of the saturation in the step response.

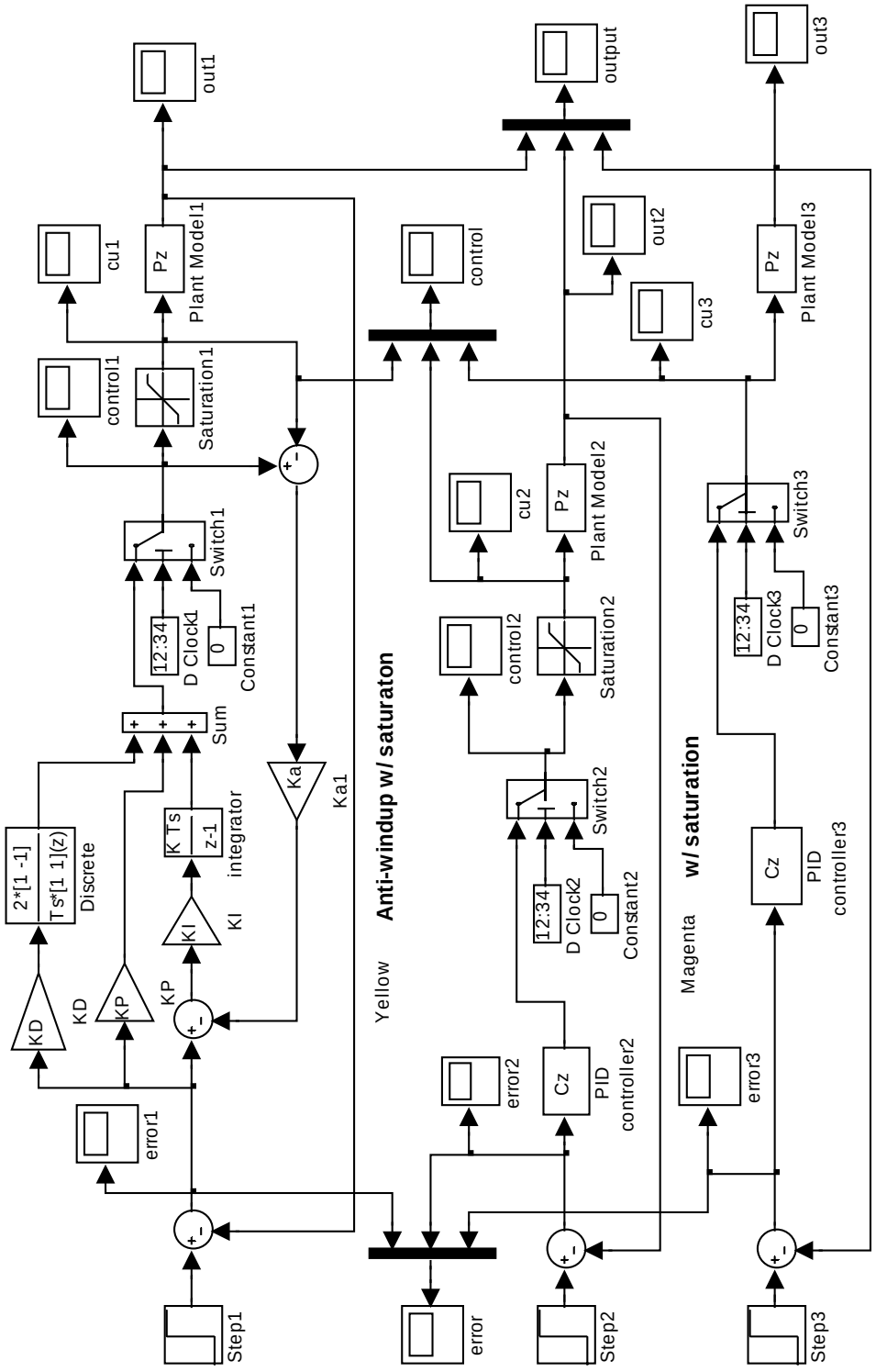

Fig. 5-2. The Simulink® block diagram for a PID controller with the anti-windup scheme.

The simulation result with the full controller including the anti-windup scheme is shown in solid line. Therefore, the effectiveness to limit the actuator saturation with this anti-windup scheme could be anticipated from these simulation results.

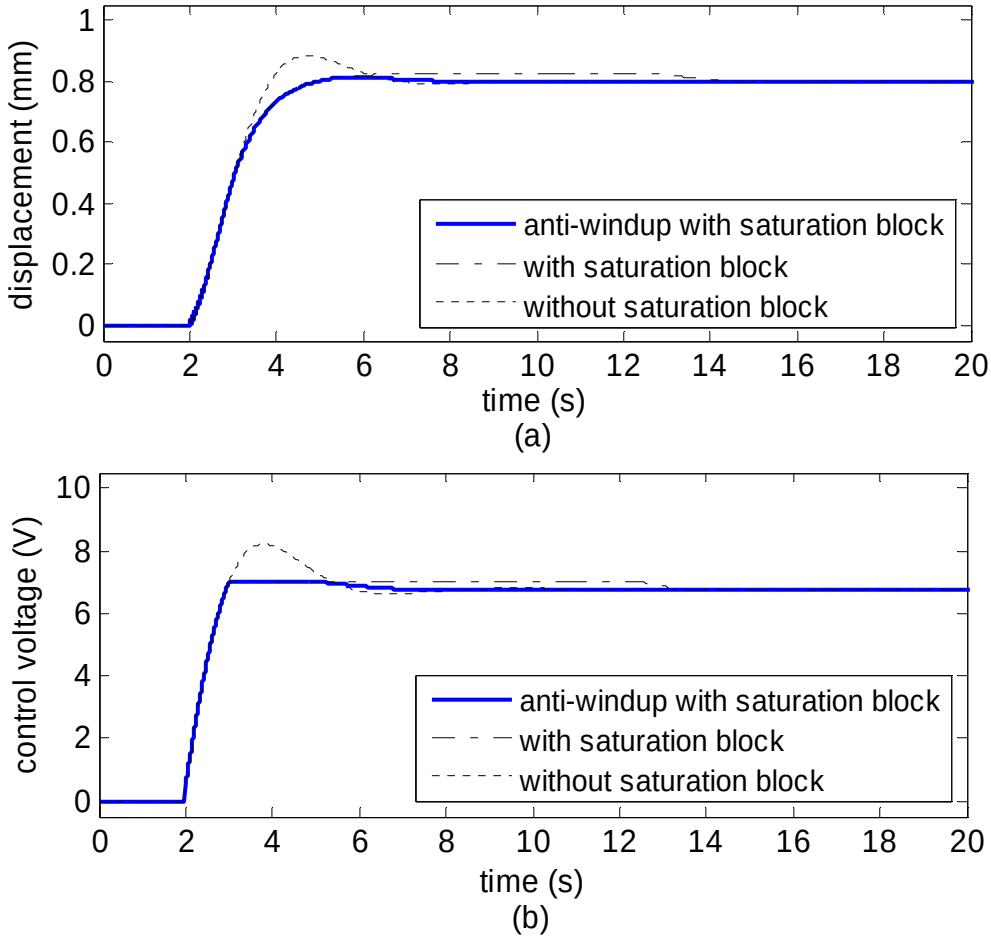

Fig. 5-3. (a) Simulated closed-loop step response to a 0.8-mm step command using the digital PID controller (5-1) without (dotted) and with (dash-dotted) the saturation block, and with the anti-windup scheme along with the saturation block (solid). (b) Corresponding control voltages applied to the plant.

The accomplished time-domain transient responses in Fig..5-3 are summarized in Table 5-2. The setting time was calculated within 5% of the steady state value and the rise time was calculated for the response time from 10% to 90% of the steady state value. The

overshoot (M_p) was decreased to 1.58% from 3.24% and the 2% setting time (t_s) was also decreased to 4.61 s from 13.29 s. As we expected the purpose of using anti-windup scheme, the system with anti-windup has substantially less the overshoot and less the control effort.

Table 5-2. List of Time Domain Transient Responses

	Overshoot (M_p)	Settling time (t_s)	Rise time (t_r)
w/o saturation block	10.33%	6.26 s	1.35 s
w/ saturation block	3.24%	13.29 s	1.69 s
Anti-windup block	1.58%	4.61 s	1.69 s

5.2.2 Experimental 0.8-mm Step Response

Fig. 5-4 shows a 0.8-mm closed-loop position response of the EAP actuator demonstrating the effectiveness of the anti-windup scheme very well. As shown in Fig. 5-4, the settling time decreased to 1.61 s from 1.78 s, and the overshoot decreased to 37.1% from 79.7%. As we verified the effect of the anti-windup effect in Fig. 5.3, the voltage difference is about 1 V as shown in Fig.5-3 (b). Since the EAP position modeling has 74.01% of the matching rate with the measured output from the laser distance sensor from Fig. 4-7, there is a discrepancy the output difference between the simulation (Fig. 5-3) and the experimental (Fig. 5-4) results, especially the overshoot case.

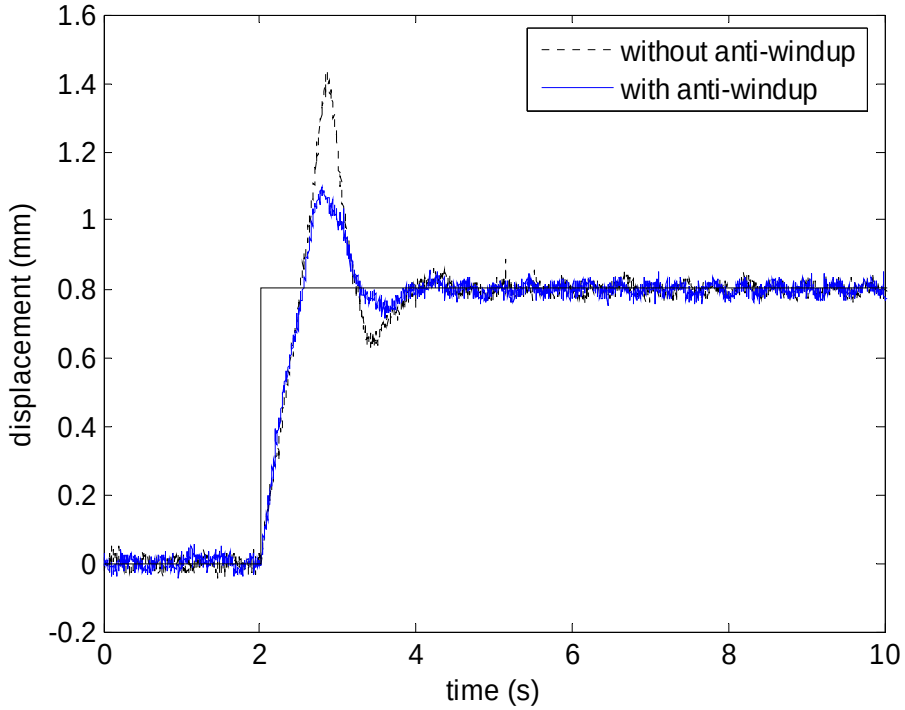

Fig. 5-4. The tracking performances of a 0.8-mm step command using the digital PID controller with and without the anti-windup scheme.

The control voltage significantly decreased in case of implementing the anti-windup scheme shown in Fig. 5-5. The control input was limited to ±3 V for the experimental case to see the effect of the anti-windup scheme. The peak control voltage decreased by 25.7% and the overall control voltage decreased by 16.1% in Fig. 5-5 (a). Note that the spike in the control voltage is caused by the accumulated error due to actuator saturation. Since the laser displacement sensor's conversion factor is 1mm per 1 V, the difference in the two initial control voltage profiles in Fig. 5-5 indicates the difference in the initial sensor readings of the tip position of EAP strip. Moreover, the initialization of the position control was performed under control of voltage about 1.5 V for 2 seconds as shown in Fig. 5.5.

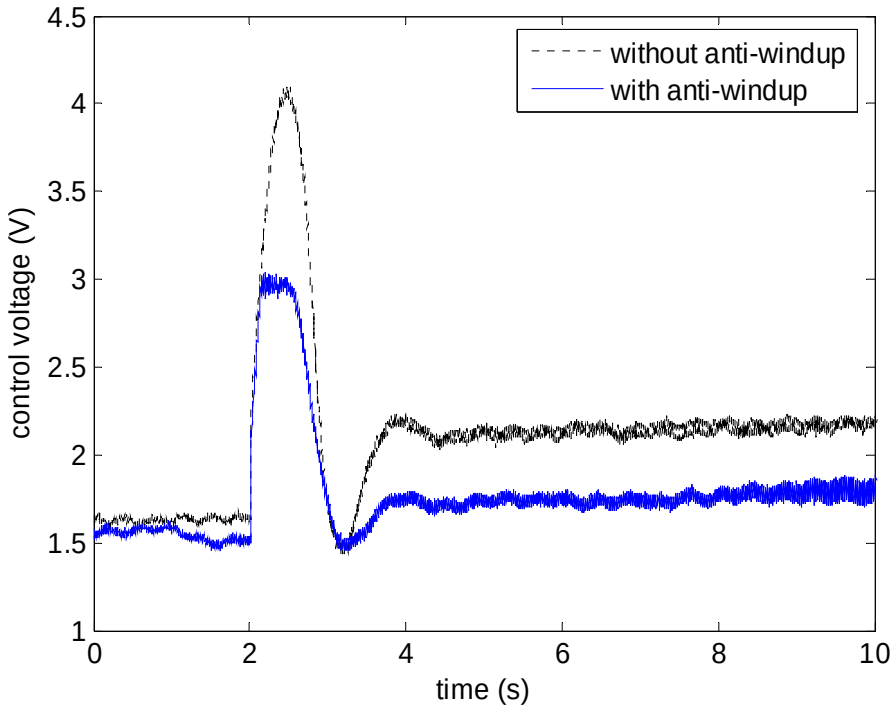

(a)

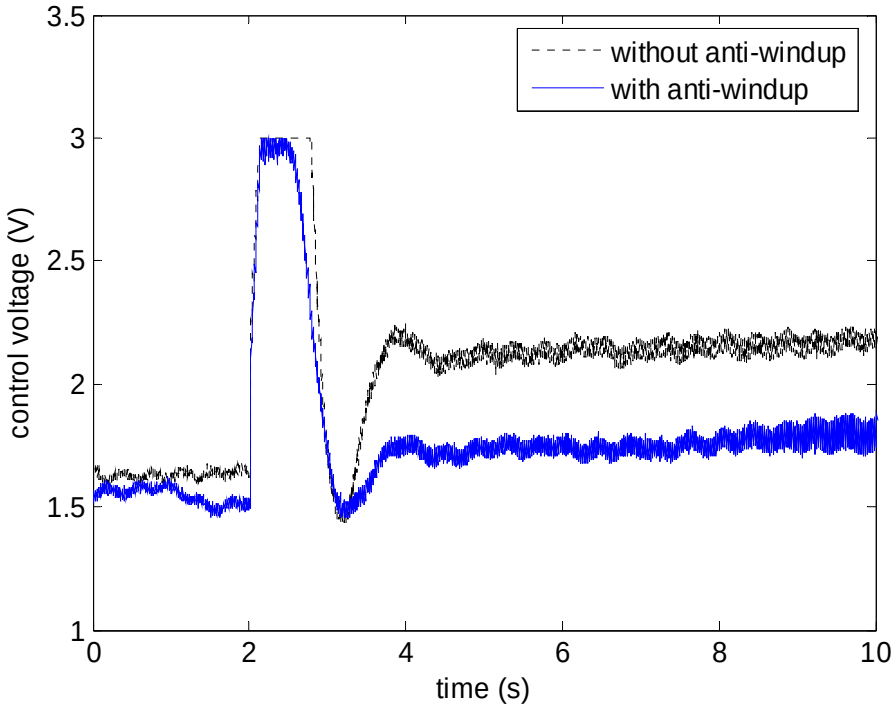

(b)

Fig. 5-5. (a) Control voltage profiles with and without the anti-windup scheme before saturation. (b) Control voltage profiles with and without the anti-windup scheme after the saturation block in Fig. 5-1.

For precision position control, the anti-windup scheme helped to reduce the overshoot and the control voltage only when the actuator was saturated. The steady-state error was also eliminated. This is very important to manipulate a micro-actuator effectively in the 'pick-and-place' operations. The accomplished time-domain transient responses in Fig. 5-4 are summarized in Table 5-3. The 5% criterion was used for the settling time, t_s.

Table 5-3. Summary of time-domain transient responses.

	with the anti-windup scheme	without the anti-windup scheme
Overshoot (M_p)	37.1%	79.7%
Settling time (t_s)	1.61 s	1.79 s
Peak time (t_p)	0.79 s	0.87 s

5.2.3 Micro-Position Control

The EAP actuator has significant potential to be used as a micro- or nano-manipulation device. Figs. 5-6 (a) and (b) show a 50-μm closed-loop step response and the corresponding control voltage. Since the control input is well within the operation range of ±7 V, no integrator windup took place, and the difference between the minimum and the maximum control voltage was only 0.186 V in Fig. 5-6 (b). In Fig. 5-6 (a), conspicuous oscillations in the position data are present. The reason for this might be a linearity error (±15 μm) on the laser distance sensor. The control voltage shown in Fig. 5-6 (b) also fluctuates to attempt to compensate for these position oscillations.

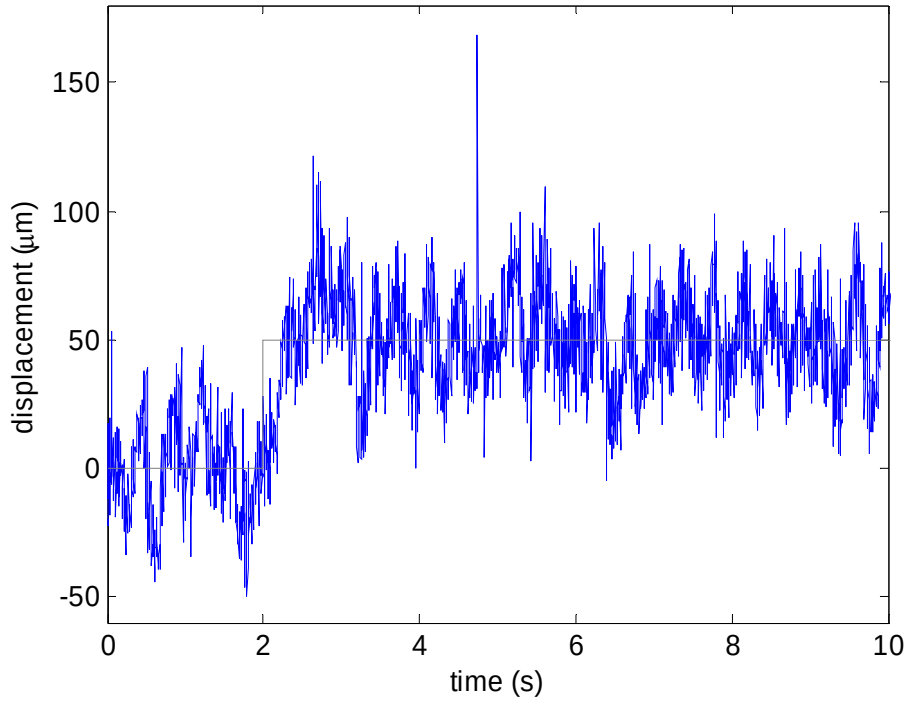

(a)

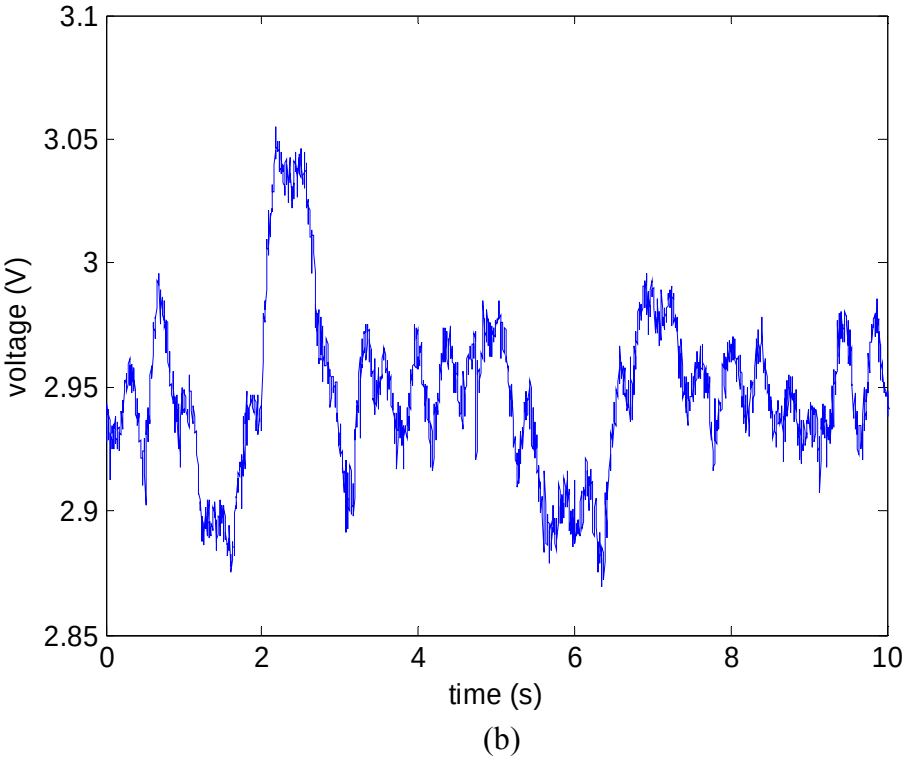

(b)

Fig. 5-6. (a) 50-μm closed-loop step response of the EAP actuator and (b) control voltage profile of the 50-μm closed-loop step response of the EAP actuator.

5.3 Modified Proportional-Integral-Derivative Controller Design for IPMC

As mentioned earlier we use IPMC strips for the fingers in a three-finger gripper. Fig. 5-7 shows the schematic diagram of the closed-loop position control of the three-finger gripper. We made the three-finger gripper be manipulated simultaneously by developing closed-loop controllers.

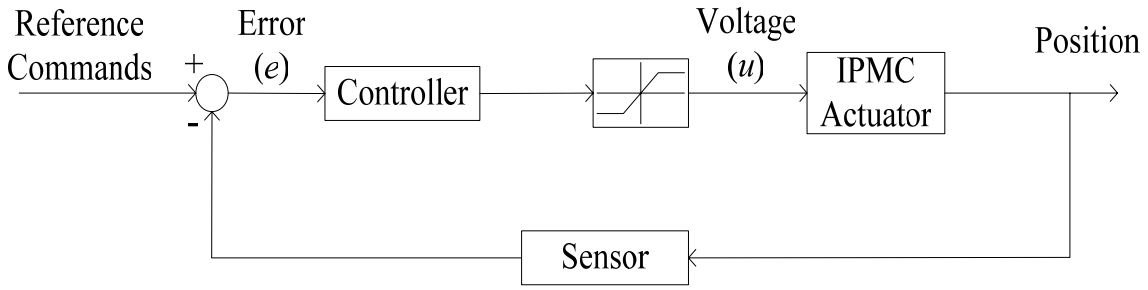

Fig. 5-7. Schematic diagram of the closed-loop position control of the three-finger gripper. The saturation block was inserted between the controller and the IPMC actuator to protect the IPMC strips from high-voltage damage.

The control objectives are as before (1) to have a 60° phase margin, (2) to follow step position commands with no steady-state error, and (3) to minimize the settling time. To achieve these control objectives, a discrete-time proportional-integral-derivative (PID) controller was designed for the IPMC gripper. First, Simulink Response Optimization provides a means to tune parameters, K_P, K_I, and K_D within a Simulink model to meet the time-domain performance requirements [66]. It automatically converts time-domain constraints into a constrained optimization problem and then solves the problem using optimization routines taken from the Optimization Toolbox or the Genetic Algorithm and Direct Search Toolbox [66]. Section 6.2 will show more detail explanation of Simulink Response Optimization.

The time-domain performance requirements we strive to meet are following: the rise time, t_r is less than 2.5 s for the step response to reach 90% from 10% of its final value; the settling time, t_s is less than 7.5 s for the 5% criterion; and the maximum overshoot, M_p is less than 20%. The saturation limit for the control input is set to ±3 V to protect the IPMC strips from high-voltage damage. After tuning the parameters of the discrete-time PID controller, we could achieve a 60° phase margin by adjusting the gain with the Matlab 'rltool'. The rearranged discrete-time PID controller from (5-1) is as follows.

$$C(z) = K_P + \frac{K_I T_s (z+1)}{2(z-1)} + \frac{2K_D (z-1)}{T_s (z+1)(2T(z-1)/(T_s (z+1)+1))}, \tag{5-3}$$

where $T = 0.01$ s, $T_s = 0.004$ s, $K_P \in [0.39653,\ 0.56376]$ V/mm, $K_i \in [1.5094,\ 3.5594]$ V/mm·s, and $K_D \in [-0.0013895,\ 0.013129]$ V·s/mm.

Equation (5-3) was considered the modified pure derivative term from the ideal PID controller. This pure derivative action is undesirable because of two reasons: (1) it can result in the amplification of high frequency sensor noise; and (2) the closed-loop system may not be internally stable, e.g., for a plant with a relative degree of one plant, the transfer function from the command signal to the control input becomes improper. This problem is usually avoided by replacing the pure derivative term $K_d s$ by $K_d s/(1+Ts)$ where T is a small positive constant number typically chosen in the range

from 0.01 to 0.1 [67]. For the discretization method, we chose a zero-order hold with the sampling period T_s.

5.4 Linear Quadratic Regulation with an Observer

A linear time-invariant discrete-time system model for motion control can be represented in state space as

$$\begin{aligned} x(k+1) &= Ax(k) + Bu(k) \\ y(k) &= Cx(k), \end{aligned} \tag{5-4}$$

where $x(k)$ is the state vector, $u(k)$ is the control input vector, $y(k)$is the output vector, and A, B, C are constant matrices. For the purpose of eliminating the steady-state error, integral states need to be augmented in the controller as shown in Fig. 5-8.

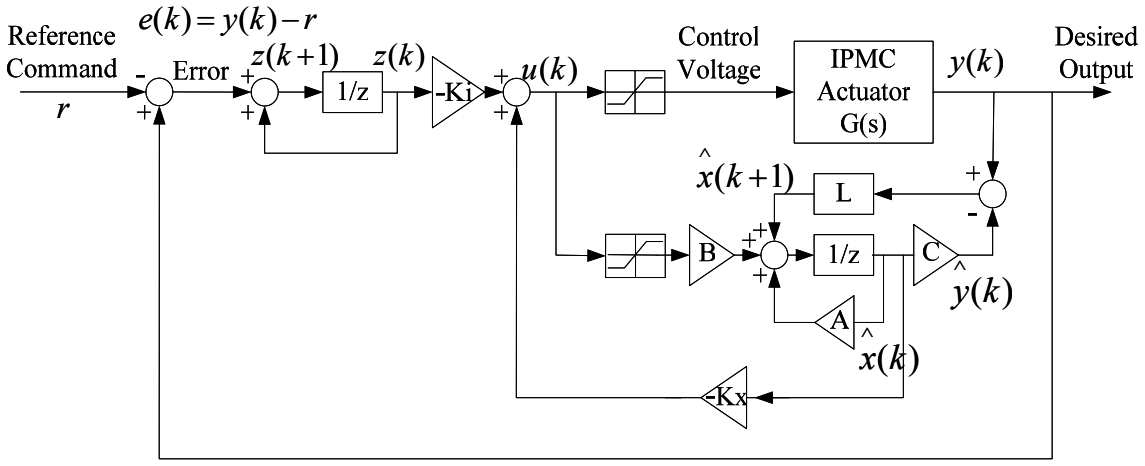

Fig. 5-8. Schematic diagram of the integrator-augmented closed-loop position control using an LQR with an observer.

The augmented system becomes

$$\begin{bmatrix} x(k+1) \\ z(k+1) \end{bmatrix} = \begin{bmatrix} A & 0 \\ CA & 1 \end{bmatrix} \begin{bmatrix} x(k) \\ z(k) \end{bmatrix} + \begin{bmatrix} B \\ CB \end{bmatrix} u(k) + \begin{bmatrix} 0 \\ -1 \end{bmatrix} r(k) \tag{5-5}$$

where the state-variable description matrices of the system are

$$\overline{A} = \begin{bmatrix} A & 0 \\ CA & 1 \end{bmatrix} = \left[\begin{array}{cccc:c} 0.0585 & 0.1133 & 0.7234 & -1.8350 & 0 \\ 2.0000 & 0 & 0 & 0 & 0 \\ 0 & 0.5000 & 0 & 0 & 0 \\ 0 & 0 & 0.0156 & 0 & 0 \\ \cdots & \cdots & \cdots & \cdots & \cdots \\ 0 & 0 & 0 & 0 & 1 \end{array}\right], \qquad \overline{B} = \begin{bmatrix} B \\ \cdots \\ CB \end{bmatrix} = \begin{bmatrix} 0.5 \\ 0 \\ 0 \\ 0 \\ \cdots \\ 0 \end{bmatrix},$$

and $\overline{C} = \begin{bmatrix} C & \vdots & 0 \end{bmatrix} = \begin{bmatrix} 0.3715 & -0.2733 & 0.1896 & -0.0001 & \vdots & 0 \end{bmatrix}$.

A new set of variables is

$$z(k) = z(k-1) + y(k) - r(k-1),$$

where $r(k)$ is a reference command and $z(k)$ is the integral of the plant output $y(k)$ [68].

Let J denote the performance index for the augmented system defined as

$$J = \int_0^\infty \left(x^T Q x + u^T R u \right) dt. \tag{5-6}$$

The optimal gain matrix K for a linear discrete-time system with this quadratic cost function was derived from the solution to the algebraic Riccati equation with $Q = qC^T C = 0.001 \cdot \mathrm{diag}\begin{pmatrix}1 & 1 & 1 & 1\end{pmatrix}$ and $R = 1$. The control law in Fig. 5-7 can also be expressed as

$$u(k) = -K_i z(k) - K_x \hat{x}(k), \tag{5-7}$$

where $K = \begin{bmatrix} K_i \vdots K_x \end{bmatrix} = \begin{bmatrix} 0.031286 \vdots 0.010873 & 0.019098 & 0.014851 & -0.0048572 \end{bmatrix}$. To calculate the optimal gain matrix K such that the state-feedback law (5-7) minimizes the cost function J. The feedback gain K consists of constant K_i for the integration and K_x with the dimension of 1 by 4 for state feedback and $\hat{x}(k)$ indicates the state estimate.

To estimate unavailable velocity states and keep the closed-loop system stable, the eigenvalues of the matrix $(\bar{A} - L\bar{C})$ must also be placed inside the unit circle using the observer gain matrix L. The observer eigenvalues should also be faster than the closed-loop system's eigenvalues of the matrix $(\bar{A} + \bar{B}K)$. Faster eigenvalues imply a smaller magnitude for these eigenvalues, i.e., closer to the origin of the z-plane. We selected the observer poles to be 10 times faster than the controller poles and calculate L to be $\begin{bmatrix} 25.993373 & 53.205025 & 25.566189 & 0.014851 \vdots 0.419645 \end{bmatrix}^T$.

Fig. 5-9 shows 1-mm closed-loop position responses of the IPMC actuator demonstrating the performance comparison of the PID controller and the modified LQR. Although there were uncertainties in the approximated linear model, the 1-mm step response using the modified LQR matched well in both the simulation and experiment as shown in Fig. 5-9. Since the control input voltage was below the saturation limit, ±3 V,

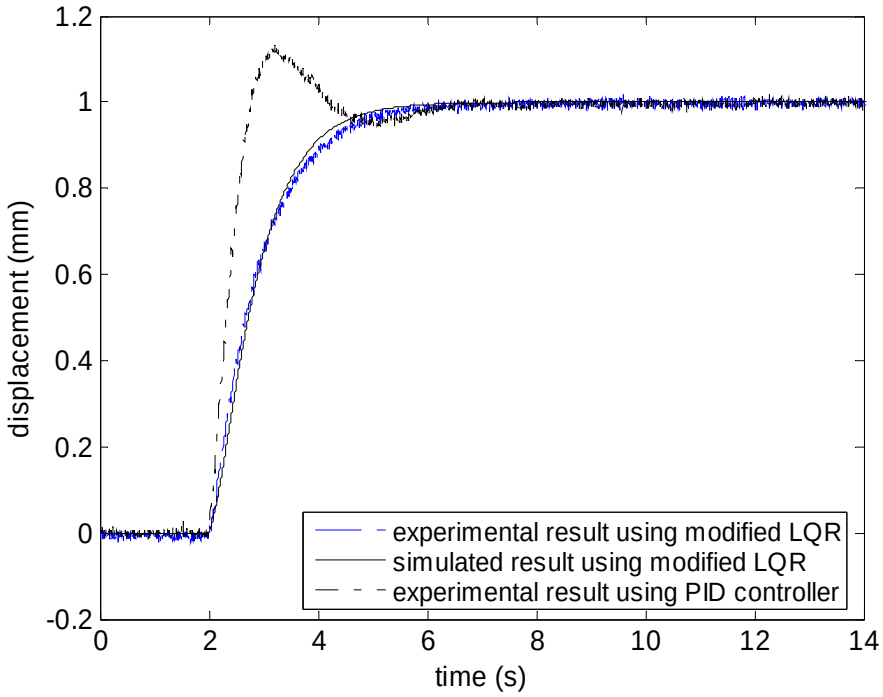

(a)

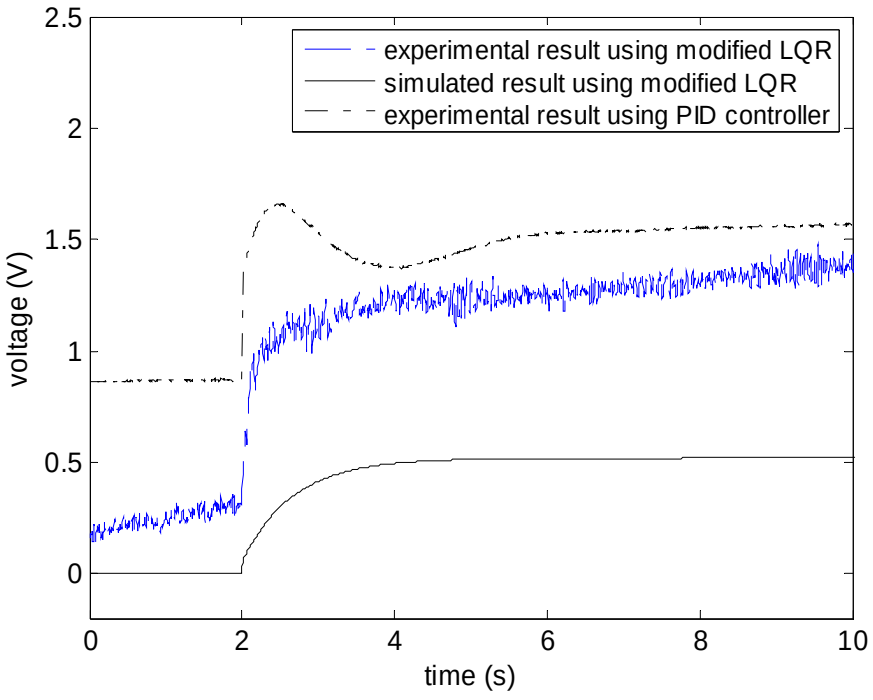

(b)

Fig. 5-9. (a) 1-mm step responses and (b) control voltage inputs with a simulated result (solid line), an experimental result (dashed line) with the modified LQR, and an experimental result (dash-dotted line) with the PID controller.

the IPMC actuator can track the desired position without causing instability due to actuator saturation. As shown in Fig. 5-9, the settling time decreased to 2.85 s from 2.98 s, and the overshoot decreased to 1.96% from 14.06%. The steady-state error was eliminated in both cases, which is very important to manipulate the micro-actuator effectively in the 'pick-and-place' operations. The achieved time-domain transient responses shown in Fig. 5-9 are summarized in Table 5-4.

Table 5-4. Achieved time-domain transient responses.

	PID controller	LQR with observer
Maximum overshoot (M_p)	14.06%	1.96%
Settling time (t_s)	2.98 s	2.85 s
Rising time (t_r)	0.56 s	1.87 s

CHAPTER VI

PRECISION POSITION AND FORCE CONTROL WITH THREE-FINGER GRIPPER

In this chapter the control system design based on the modeling in Chapter IV is explained. Various position and force tests were performed that demonstrate the capabilities of the EAP and the IPMC actuator.

6.1 Position Control of Three-Finger Gripper

Manipulation tasks require the precise position information of the end-effector in the reference frame. With advanced fabrication techniques it might be possible to fabricate micro-tips build onto the fingers of the microgripper.

Although EAP can be a candidate of the gripper, but we used IPMC for the gripper due to a limited sample provided by Dr. Rediniotis's group. The gripper fingers are made of IPMCs, which along with the position feedback of the actuator will help in developing a force feedback mechanism for a human-machine interface device. In the rest of this chapter, we present key simulation and experimental results with the developed microgripper.

6.1.1 Macroscale Motion Control

Fig. 6-1 shows the tracking performance of the three IPMC fingers with respect to the given position-command profiles. The IPMC gripper was initialized in the first 10

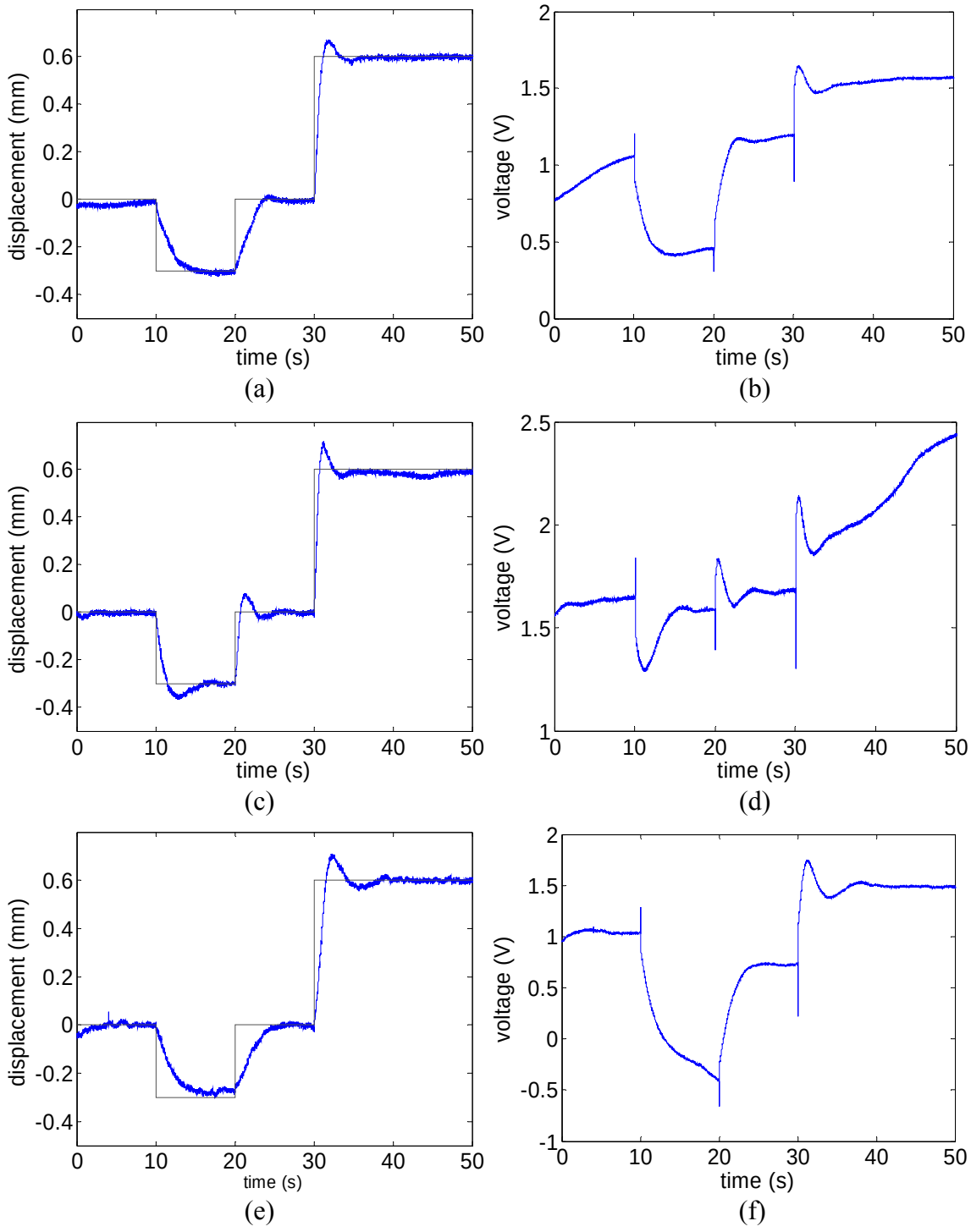

Fig. 6-1. (a) –0.3-mm and 0.6-mm step responses and (b) the control input voltage of IPMC Finger 1. (c) and (d) of IPMC Finger 2. (e) and (f) of IPMC Finger 3.

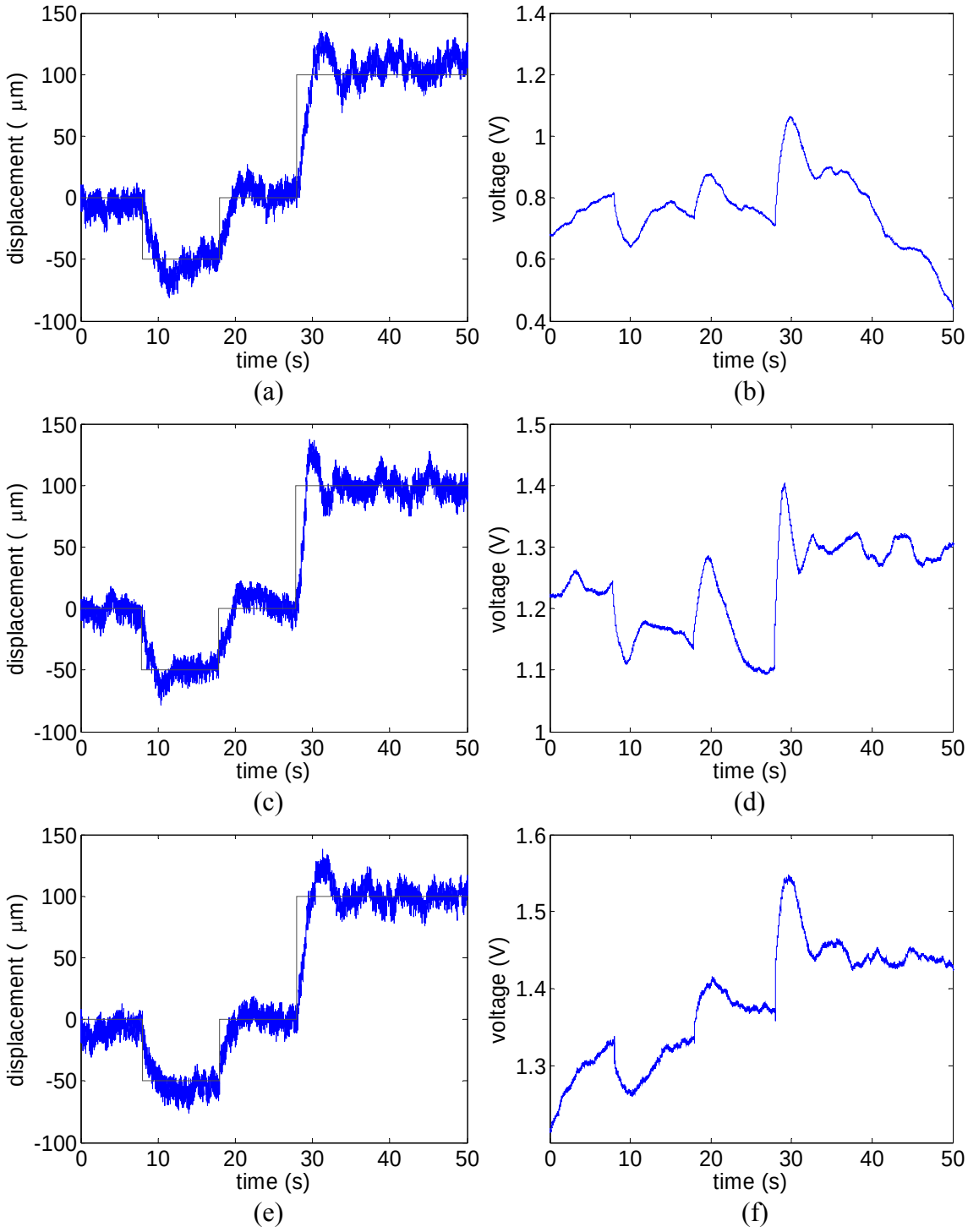

Fig. 6-2. (a) –50-μm and 100-μm step responses and (b) the control input voltage of IPMC Finger 1. (c) and (d) of IPMC Finger 2. (e) and (f) of IPMC Finger 3.

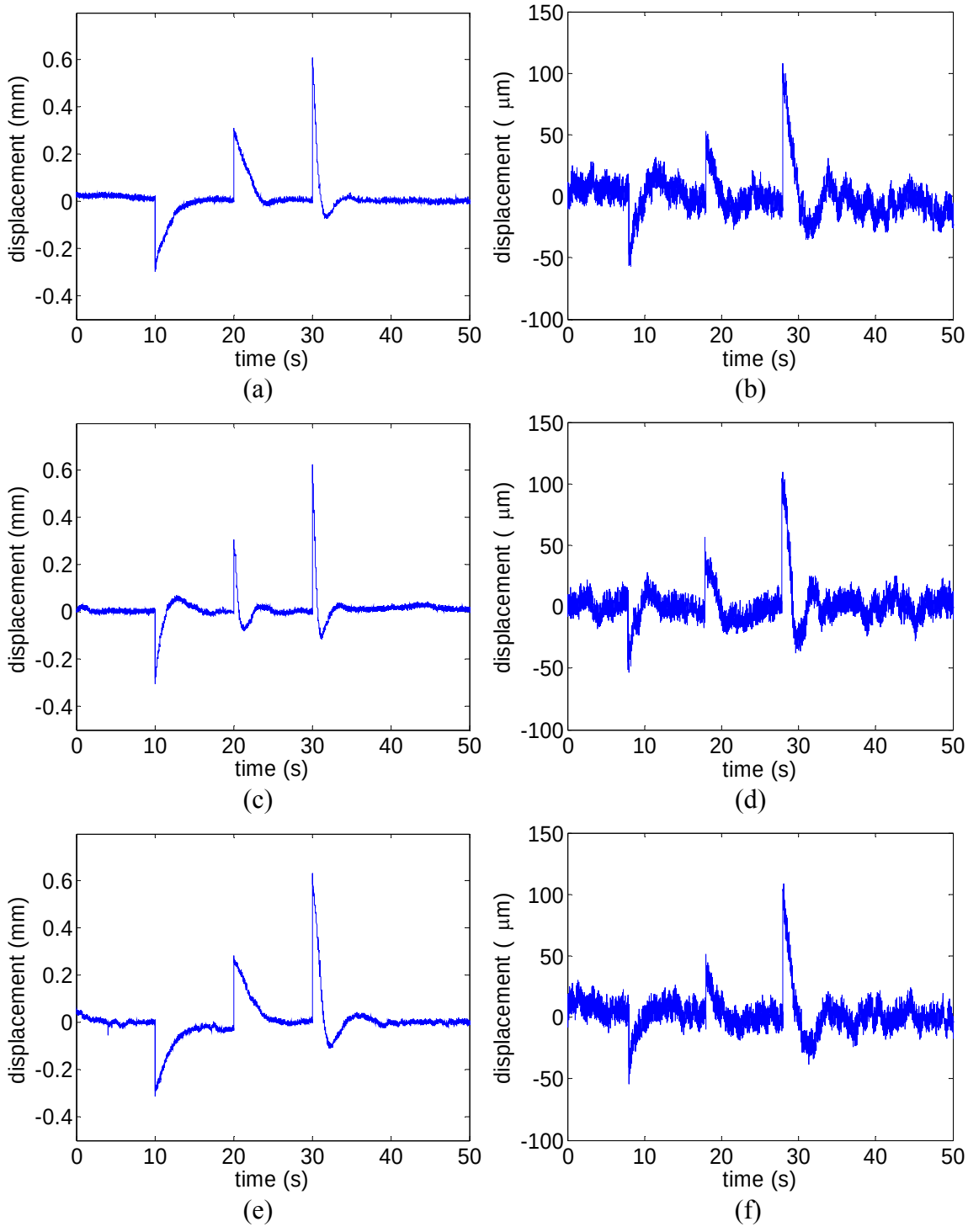

Fig. 6-3 (a), (c), and (e) –0.3-mm and 0.6-mm errors of IPMC Finger 1, 2, and 3, respectively and (b), (d), and (f) –50-μm and 100-μm errors of IPMC Finger 1, 2, and 3, respectively.

seconds. After that the control voltage generated bending motion to reach the first commanded position profile that simulated picking up a small object until the gripper moved to the target place. When the object reached the target place, the gripper started to release the object. Fig. 6-1 (a) and (b) indicate the closed-loop position response and the control input voltage of IPMC Finger 1, respectively. Fig. 6-1 (c) and (d) are of IPMC Finger 2, and Fig. 6-1 (e) and (f) are of IPMC Finger 3 in the same order.

6.1.2 Microscale Motion Control

The developed three-finger gripper has significant potential to be used as a micro- and nano-manipulation device. Fig. 6-2 shows –50-μm and 100-μm closed-loop step responses and the corresponding control voltage inputs. Since the control inputs were well within the safe operation range of ±3 V, no integrator anti-windup was necessary [62]. The difference between the minimum and maximum control voltages was only about 0.7 V in Fig. 6-2 (b), (d), and (f). For the errors corresponding to the given position-command profiles, Fig. 6-3 (a), (c), and (e) show –0.3-mm and 0.6-mm errors of IPMC Finger 1, 2, and 3 respectively and Fig. 6-3 (b), (d), and (f) show –50-μm and 100-μm errors of IPMC Finger 1, 2, and 3 respectively. Each peak occurs due to sudden changes from different step inputs.

6.1.3 Additional Motion Responses

The gripper's time-domain performance in response to another standard test signal, a ramp input, was provided in Fig. 6-4. The tracking error approaches to zero even if the output follows a non-decaying command. As shown in Fig. 6-4, the IPMC gripper

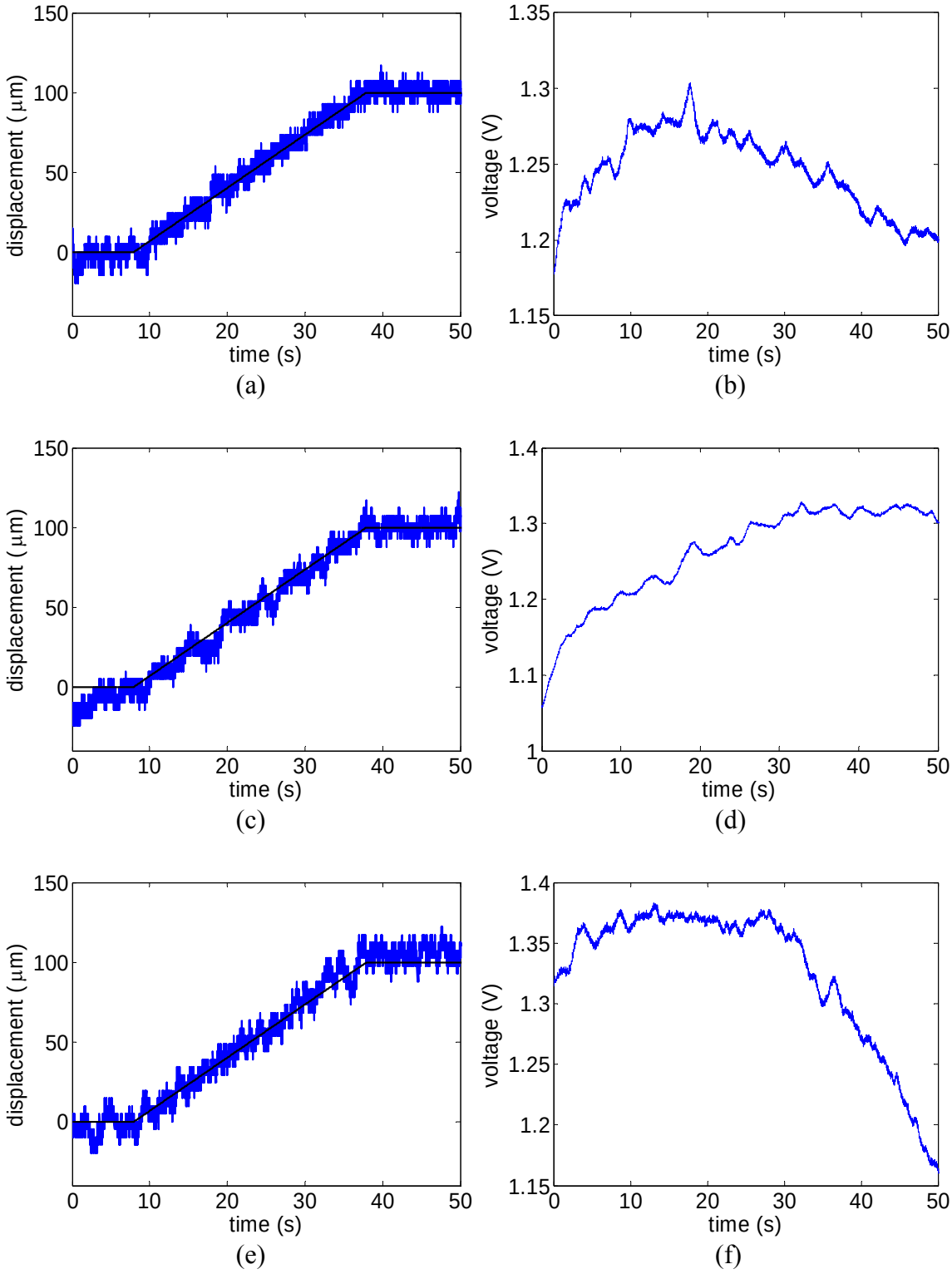

Fig. 6-4. (a) 3.33-μm/s ramp response and (b) the control of IPMC Finger 1. (c) and (d) of IPMC Finger 2. (e) and (f) of IPMC Finger 3.

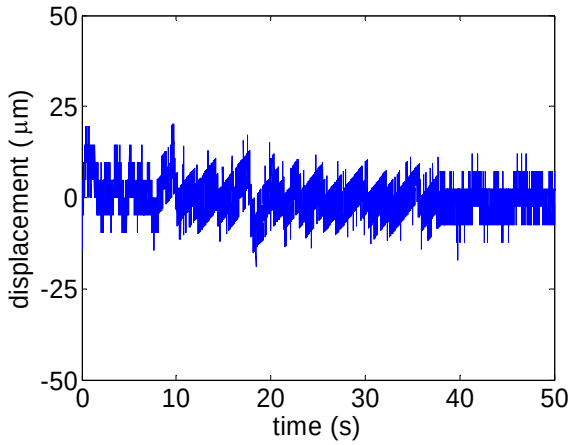

(a)

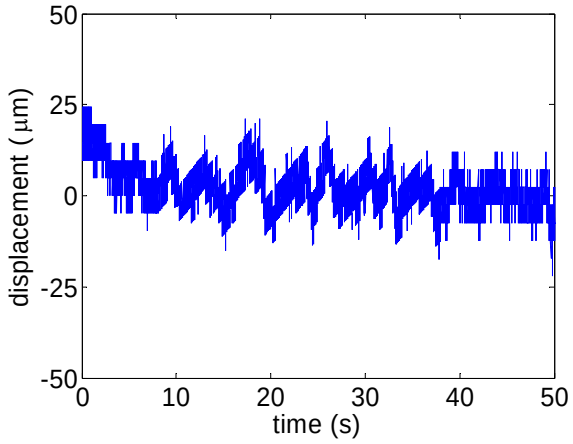

(b)

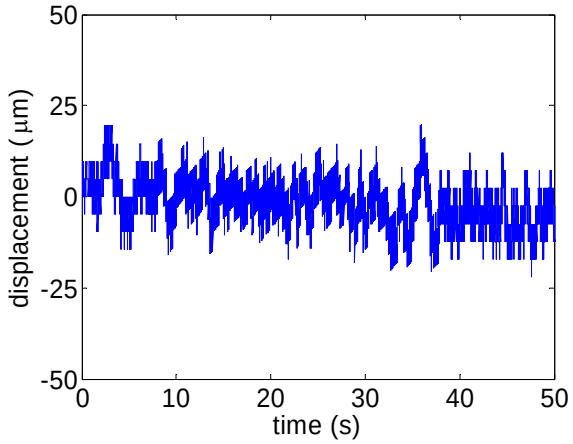

(c)

Fig. 6-5. (a), (b), and (c) 3.33-μm/s errors of IPMC Finger 1, 2, and 3, respectively.

was regulated for initialization in the first 8 seconds. After the ramp signal was applied, appropriate control voltages were generated to follow the command trajectory. The ramp command trajectory went from 0 μm to 100 μm in 30 seconds. Fig. 6-4 (a) and (b) represent the closed-loop response to the ramp command profile with the slope of 3.33 μm/s and the tracking error of IPMC Finger 1, respectively. Fig. 6-4 (c) and (d) are of IPMC Finger 2, and Fig. 6-4 (e) and (f) are of IPMC Finger 3 in the same order. The mean values of the errors are –0.1281, 2.7979, and –4.7891 μm with the standard deviations of 5.2788, 8.3575, and 8.4697 μm in the order of IPMC Finger 1, 2, and 3. Fig. 6-5 shows the errors of the ramp inputs. As we expected, the order of the errors in Fig. 6-5 are similar to those in Figs. 6-3 (b), (d), and (f).

6.2 Force Control of Three-Finger Gripper

For the application of micro-manipulation devices such as a microgripper, delicate force control becomes of primary importance. To develop force control, the parameters of a modified PID gains may be tuned manually. After initial tuning is accomplished, the parameters in the optimal process taken from the Optimization Toolbox, Genetic Algorithm and Direct Search Toolbox can be used to refine the gains further. Simulink® Response Optimization provides a graphical user interface (GUI) to assist in tuning and optimization of control systems and physical systems. Without the initial tuning procedure, the optimal algorithm may not find the values of the modified PID gains which the system output requires to meet the desired reference input. Therefore, we need to adjust the tuned parameters to better meet the objectives. Fig. 6-6 shows the GUI that helps to find the gains of the modified PID controller.

'Pz' indicates the system model obtained from the system identification and 'PID controller' block contains 3 parameters shown in Fig. 6-6 (b) for tuning under two constraints. The actuator constraint is similar to the saturation block. It was limited within ±3 V for the IPMCs and ±7 V for the EAP. The output constraint in Fig. 6-6 (a) contains the specifications for the response of the force control with the maximum overshoot of 20%, the rise time of 2.5 s, and the settling time to within the 5% of the final value of 7.5 s. The lower and upper constraint bounds define a channel within which the signal response should lie. After adjusting the constraint bounds in the constraint block and specifying the tuned parameters using the tuned Parameters dialog, we are ready to begin

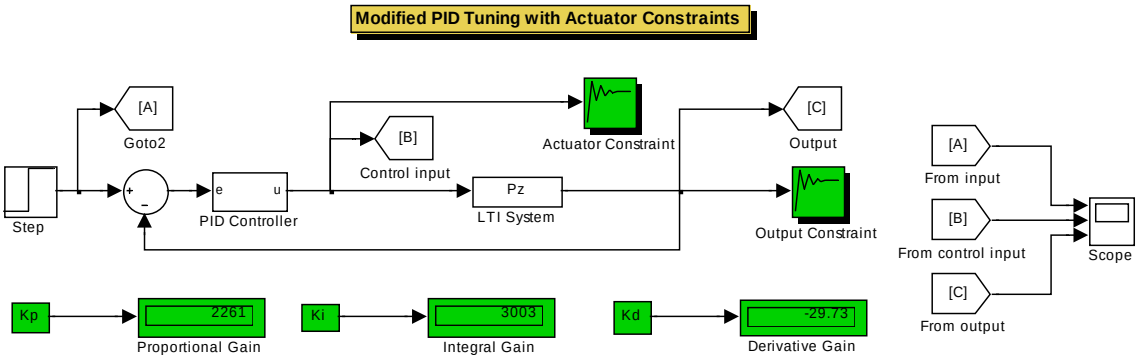

(a)

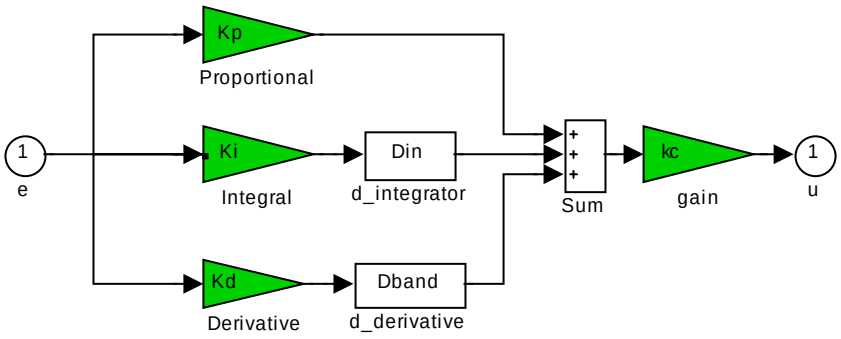

(b)

Fig. 6-6. (a) Schematic diagrams of the Simulink® Response Optimization and (b) the modified PID controller.

the optimization. The number of iterations necessary for the optimization to converge or terminate will depend on the initial guess for the tuned parameters, the specific positioning of the constraints, and the optimization settings [66].

As shown in Fig. 6-6 (b), the discrete modified PID controller consists of the following equation.

$$D_{in}(z)=\frac{T_s}{(z-1)},$$

$$D_{band}(z)=\frac{(z-1)}{T(z-\exp(-T_s/T)},$$

$$C(z)=K_c\left(K_P+K_I D_{in}(z)+K_D D_{band}(z)\right), \qquad (6\text{-}1)$$

where

$T=0.01\text{s}$, $T_s=0.004\text{s}$, $K_c=\{1.6667,\ 3.3217,\ 2.1314\}$, $K_p=\{2261,\ 3925.4,\ 312.6\}$ V/N,

$K_i=\{3002.5,\ 6768.4,\ 5810.9\}$ V/N·s, and $K_d=\{-43.5732,\ -42.3919,\ -41.7766\}$ V·s/N.

$D_{in}(z)$ and $D_{band}(z)$ are the discrete-time form of the integrator $1/s$ and the modified derivative term $s/(Ts+1)$, respectively with the zero-order hold with the sampling period T_s. K_c was used to satisfy the phase margin requirement. K_c parameter can be calculated by the Matlab 'margin' command or read from a table. K_c is obtained from the margin command, 'kc=margin(mag,phase-60,w)' which intentionally shifts the phase margin by 60° and finds the gain margin at this frequency. 'mag', 'phase', and 'w' were obtained from using the Matlab script '[mag,phase,w]=bode(Lz)' where Lz is the loop transfer function. In addition, we can also make a table including the magnitude, the phase, and

the frequency of the loop transfer function, Lz. From this table, we can see the phase shift of about -120° required by the specification of $\mathrm{PM} = 60^\circ$ is achieved at a certain magnitude. Consequently, gain by the inverse of this magnitude defines the proper gain K_c. This Matlab code was added in Appendix B. Therefore, the final z-domain controllers are given below.

$$C_{1f}(z) = \frac{-2632z^2 + 6195z - 3566}{z^2 - 1.67z + 0.6703}$$

$$C_{2f}(z) = \frac{-331z^2 + 2056z - 1715}{z^2 - 1.67z + 0.6703} \tag{6-2}$$

$$C_{3f}(z) = \frac{-1408z^2 + 4234z - 2815}{z^2 - 1.67z + 0.6703}$$

From (4-21) and (6-2), the pole and the zero location of the closed-loop transfer function were summarized in Table 6-1.

Table 6-1. Pole-zero locations of closed-loop transfer functions.

	IPMC 1	IPMC 2	IPMC 3
Poles of the closed-loop transfer function	0.9440 + 0.1937i 0.9440 – 0.1937i 0.9944 + 0.0009i 0.9944 – 0.0009i 0.9602 0.6029	0.8154 + 0.2794i 0.8154 – 0.2794i 0.9814 0.9938 0.6347	0.9106 + 0.2190i 0.9106 – 0.2190i 0.9871 0.9932 0.4760
Zeros of the closed-loop transfer function	1.3665 0.9948 0.9912 0.9522 0.4108	5.2172 0.9933 0.9782 0.6323	2.0138 –0.5331 0.9928 0.9822

Fig. 6-7 shows Bode plots of the loop transfer functions with three force models. The phase margins were 58.3° at a crossover frequency of 5.4 Hz in Fig. 6-7 (a), 59.8° at a crossover frequency of 9.29.4 Hz in Fig. 6-7 (b), 60.3° at a crossover frequency of 6.16 Hz in Fig. 6-7 (c).

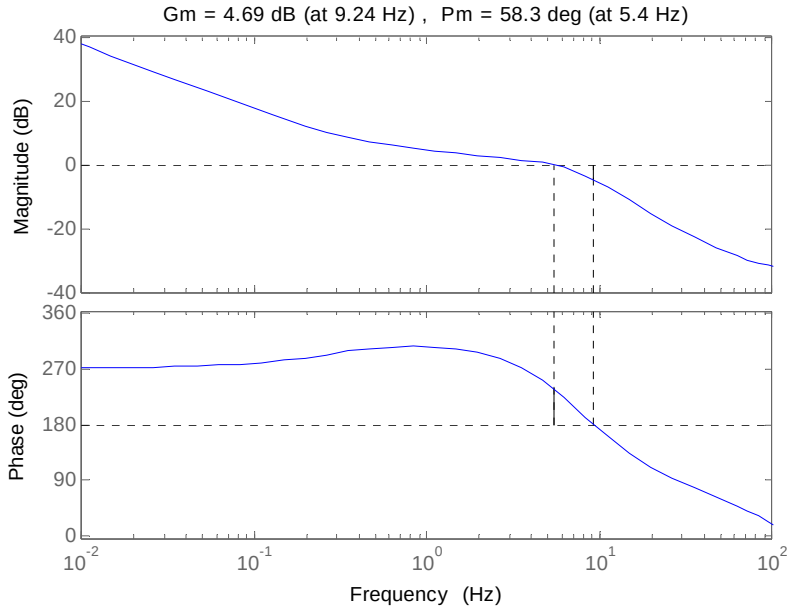

(a)

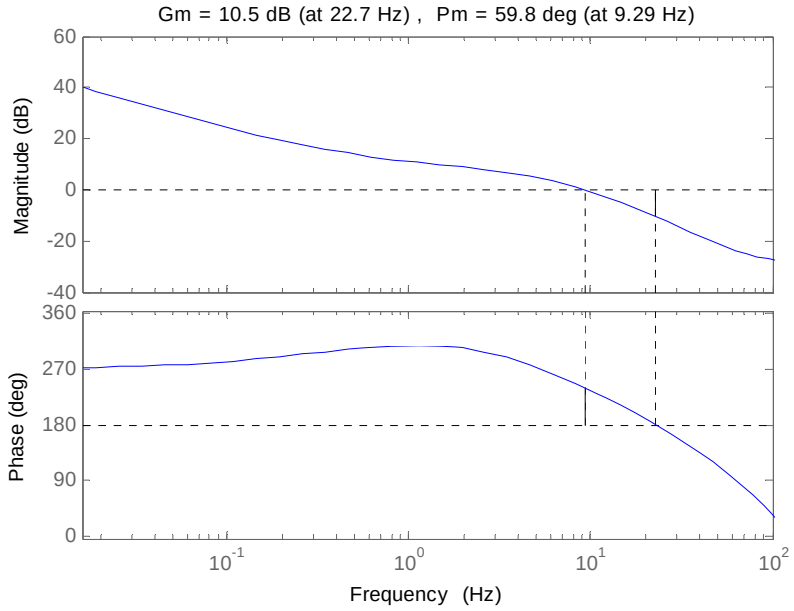

(b)

Fig. 6-7. Bode magnitude and phase plots for the loop systems with the modified PID controllers for (a) IPMC Finger 1, (b) IPMC Finger 2, and (c) IPMC Finger 3.

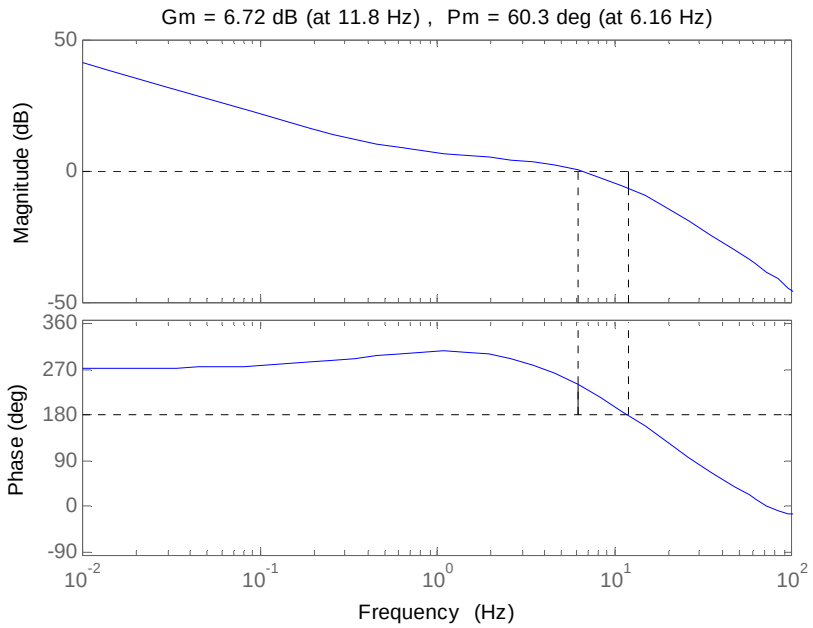

(c)

Fig. 6-7. (Continued).

6.2.1 Macroscale Force Control

Fig. 6-8 (a) shows the tracking performance of the IPMC finger 1 with respect to a 1-mN step input. The force input was applied at t = 18 s. The overshoot is 0.59%, and the rise time is 0.69 s, and the 2% settling time is 2.6764 s. The rise time is assumed to be the time for the response to initially travel from 10% to 90% of the final value. Fig. 6.8 (b) shows the control input profile which is less than the saturation limit. Therefore this tracking performance does not require the integrator anti-windup scheme. Fig. 6-8 (c) presents the frequency response of this tracking case. Fig. 6-8 (c) shows a 1-mN step response of the IPMC finger 2. The overshoot is 1.55%, the rise time is 0.1045 s, and the 2% settling time is 1.8447 s. Fig. 6-8 (e) shows a 1-mN step response of the IPMC finger 3. The overshoot is 0.83%, the rise time is 0.3552 s, and the 2% settling time is 4.6087 s.

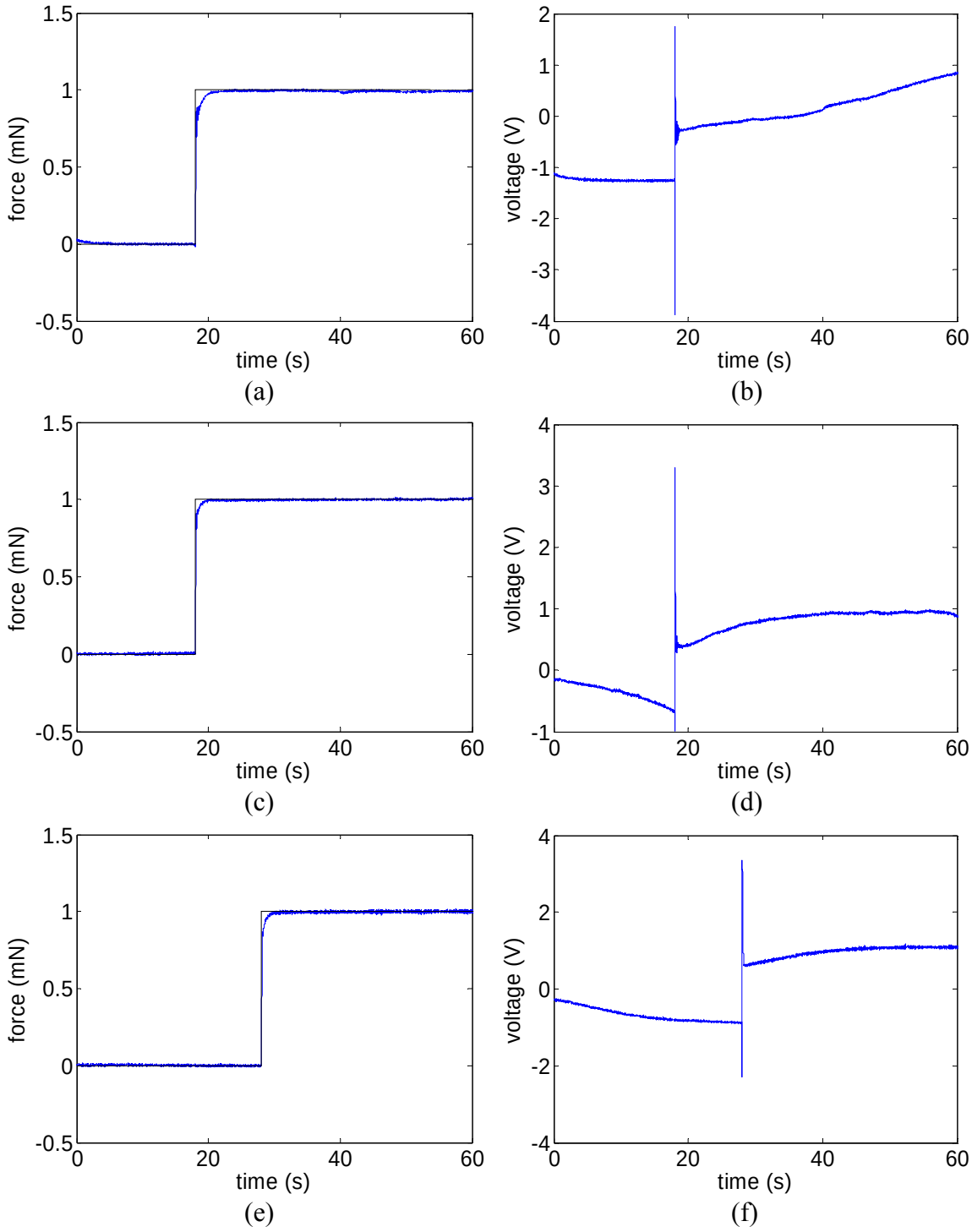

Fig. 6-8. (a) Closed-loop response to a 1-mN step input and (b) controller output for the 1-mN closed-loop step response for IPMC Finger 1. (c) Closed-loop response to a 1-mN step input and (d) controller output for the 1-mN closed-loop step response for IPMC Finger 2. (a) Closed-loop response to a 1-mN step input and (b) controller output for the 1-mN closed-loop step response for IPMC Finger 3.

The experimental results show that all time performance specifications such as the rise time, the settling time, and the overshoot are within the specification of controller design. For the actuator constraint as shown in Fig. 6-6 (a), the IPMC Fingers 1, 2, and 3 can track very well for the 1-mN step input within ±3 V control input. Each voltage spikes shown in Figs. 6-8 (b), (d), and (f) are natural phenomena occurring at sudden changes like a step input, but these last only momentarily.

6.2.2 Microscale Force Control

Fig. 6-9 (a) shows a 100-μN step response of the IPMC Finger 1. The overshoot was 22.15%, the rise time is 0.69 s, and the 2% settling time is 11.9868 s. The control voltage profile shown in Fig. 6-9 (b) was less then 1 V since the tracking force is small. Fig. 6-9 (c) shows a 100-μN step response of the IPMC Finger 2. The overshoot is 46.0962%, the rise time is 0.0248 s, and the 2% settling time is 11.9776 s. Fig. 6-9 (e) shows a 100-μN step response of the IPMC Finger 3. The overshoot is 12.57%, the rise time is 4.6534 s, and the 2% settling time is 11.99 s. Only the settling time for all IPMC fingers is better than the design of control specification, 7.5 s since the noise effect dominates in the tracking response. This might be coming from the sensor noise or the uncertainty of the model, etc.

6.2.3 Micro-Macroscale Force Control

Fig. 6-10 shows the tracking performance of 100-μN, 1-mN, and 500-μN closed-loop step responses and the corresponding control voltage inputs in the IPMC Finger 1.The gripper was initialized in the first 18 seconds, which was required to regulate the

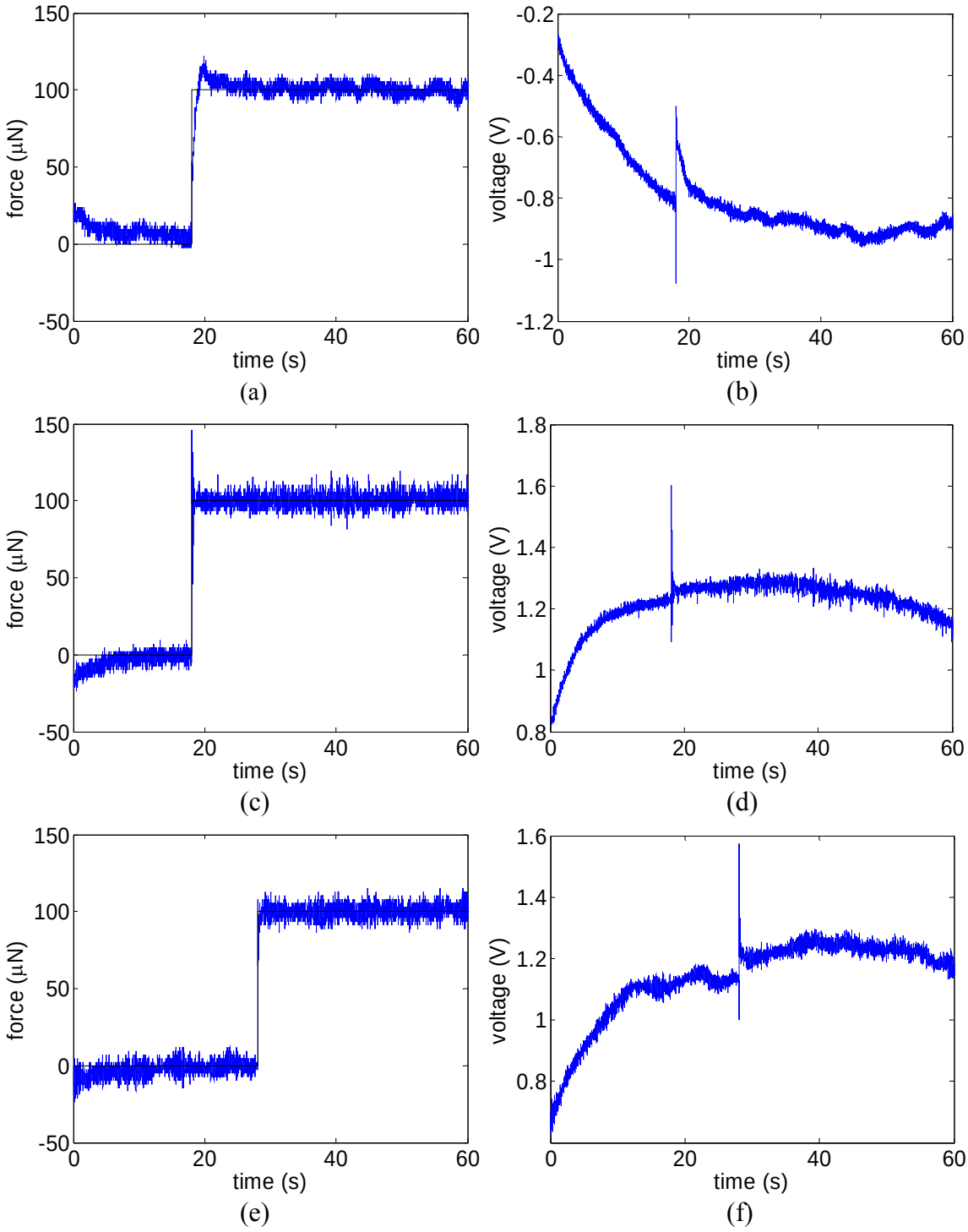

Fig.6 -9. (a) Closed-loop response to a 100-μN step input and (b) controller output for the 100-μN closed-loop step response for IPMC Finger 1. (c) Closed-loop response to a 100-μN step input and (d) controller output for the 100-μN closed-loop step response for IPMC Finger 2. (e) Closed-loop response to a 100-μN step input and (f) controller output for the 100-μN closed-loop step response for IPMC Finger 3.

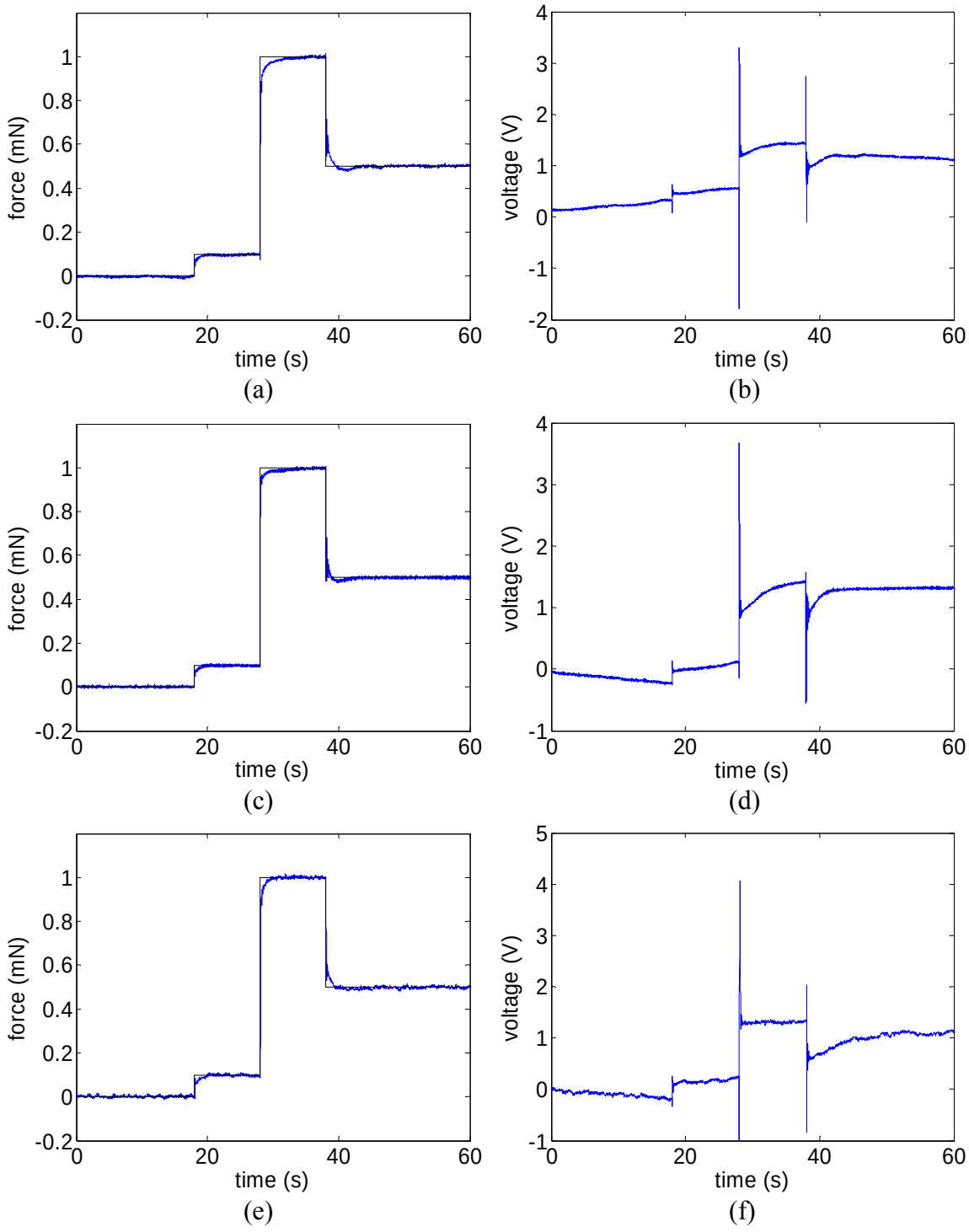

Fig. 6-10. (a) 100-μN, 1-mN, and 500-μN step responses and (b) the control input voltage for IPMC Finger 1. (c) 100-μN, 1-mN, and 500-μN step responses and (d) the control input voltage for IPMC Finger 2. (e) 100-μN, 1-mN, and 500-μN step responses and (f) the control input voltage for IPMC Finger 3.

residual force to be zero. After that the control voltage generated the force to follow the first commanded step at t = 18 s that simulated the smooth approach stage right before grabbing the object. When the object was touched tenderly at t = 18 s, the control voltage generated more voltages to grab the object without any drop as long as the generated force does not give any damage on the object. This grabbing stage was continued for 10 s from t = 28 s to 38 s. The last step at t = 38 s was demonstrated for releasing the object. The three-finger gripper is available in 3 motions independently. This gripper can control of the gripping force between 100 μN and 1 mN. The spikes shown in Fig. 6-10 (b) again were the transient phenomena when the reference force commands changed rapidly. Figs. 6-10 (c) and (e) show the same tracking responses with the IPMC Finger 2 and the IPMC Finger 3, respectively. All control input profiles were less than the saturation voltage limit.

6.2.3 Additional Force Control for EAP

For the force control of EAP actuator, the modified PID controller gain was calculated with the same design specification as the IPMC Fingers and followed as:

$K_c = 1.2634$, $K_p = 3.4151 \times 10^3$ V/N, $K_i = 1.4084 \times 10^4$ V/N·s, and $K_d = -28.6826$ V·s/N.

$$C(z) = \frac{690.9\,z^2 + 111.9\,z - 779.3}{z^2 - 1.67\,z + 0.6703}. \tag{6-3}$$

Fig. 6-11 shows a 100-μN step response of the EAP actuator. The overshoot was 9.15%, the rise time is 0.0212 s, and the 2% settling time is 10.5383 s. The phenomenon

of a microscale force step input of the EAP actuator turned out to be the same behavior as the IPMC Fingers had in Fig. 6-9.

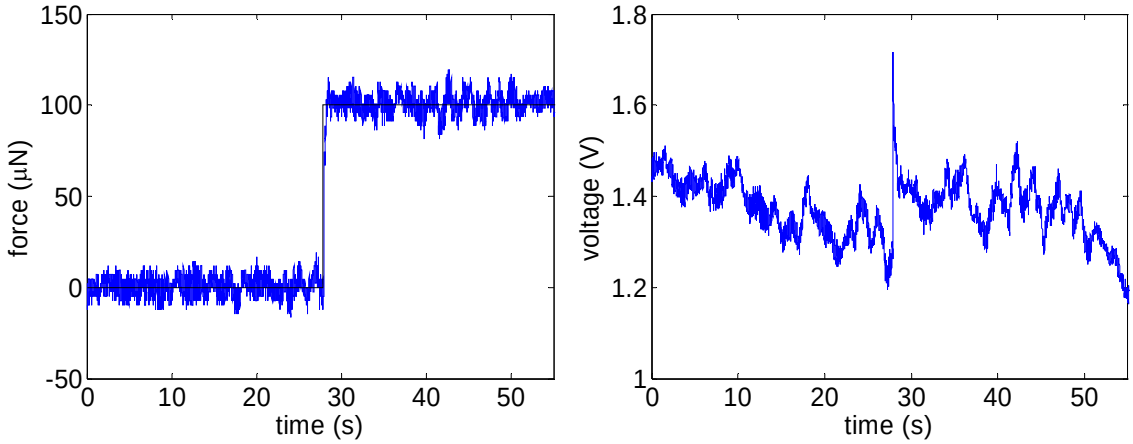

Fig. 6-11. (a) Closed-loop response to a 100-μN step input. (b) Controller output for the 100-μN closed-loop step response of EAP.

Fig. 6-12 (a) shows the tracking performance of the EAP actuator with respect to a 1-mN step input. The force input was applied at t = 28 s. The overshoot is 2.89%, and the rise time is 0.72 s, and the 2% settling time is 1.4264 s. The control voltage was even within ±3 V in order to follow the reference force command. To compare with IPMC Fingers in Fig. 6-10, the similar tracking response was performed in Fig. 6-13 except the overshoot. It shows about 10% overshoot in EAP actuator. Based on the results shown in Figs. 6-11, 6-12, and 6-13, the EAP actuator can be used as a substitute for the three-finger gripper design.

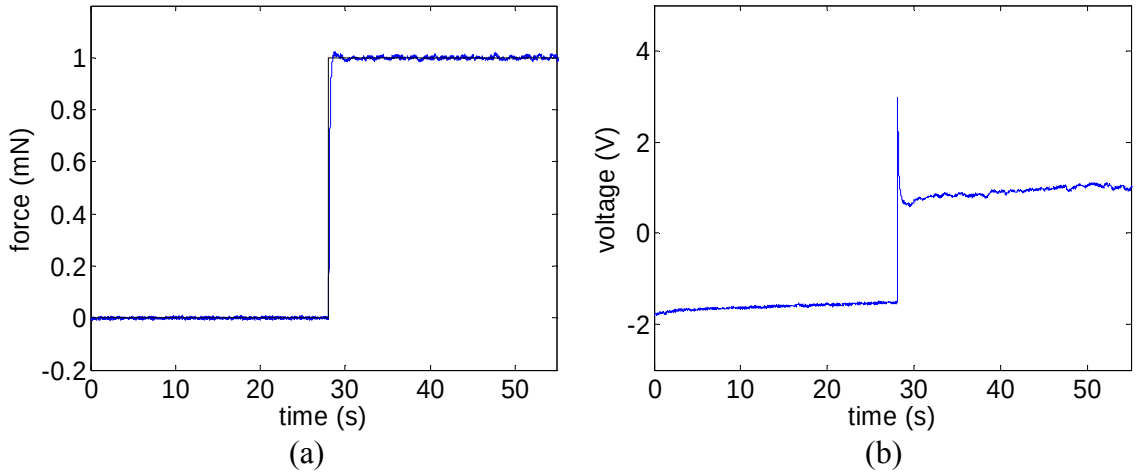

Fig. 6-12. (a) Closed-loop response to a 1-mN step input. (b) Controller output for the 1-mN closed-loop step response of EAP.

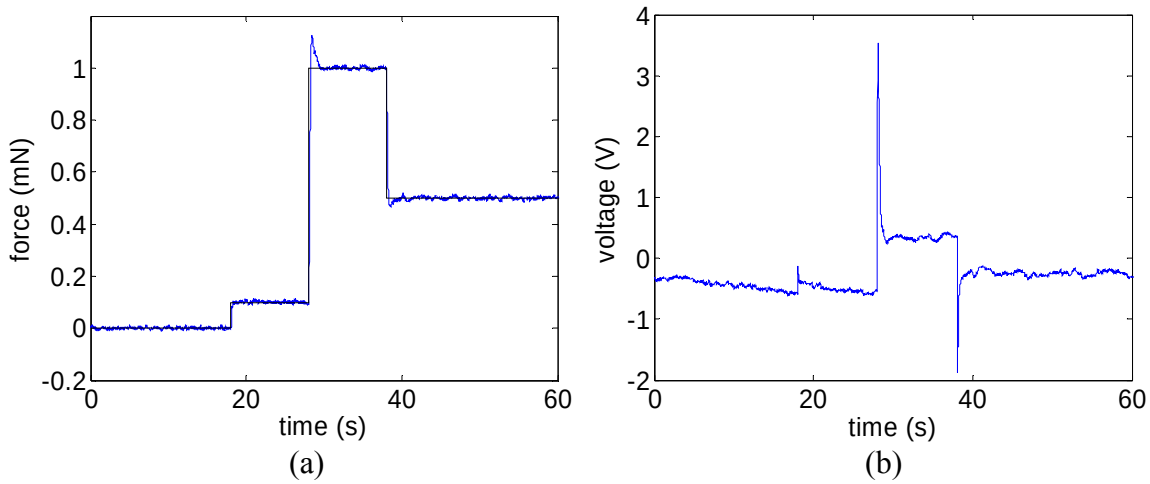

Fig. 6-13. (a) 100-μN, 1-mN, and 500-μN step responses and (b) the control input voltage of EAP.

6.3 Demonstration of Three-Finger Gripper

The demonstration of grabbing an object with the three-finger gripper was performed. The IPMC finger tips were modified by attaching small plastic spoons made

from a commercial folder-label case. Since the mass of the IPMC Fingers were changed due to adding the plastic spoons, the system identifications for the modified IPMC Fingers were necessary to be produced again. Three discrete-time IPMC transfer functions representing open-loop position responses acquired by the fourth-order BJ models are as followed.

$$G_{1p}(z)=\frac{385z^3-1205z^2+1258z-437.6}{z^4-2.076z^3+1.702z^2-0.5304z+0.04236}$$

$$G_{2p}(z)=\frac{-90.53z^3+270.1z^2-268.7z+89.17}{z^4-2.202z^3+1.994z^2-0.9434z+0.1611} \quad (6\text{-}4)$$

$$G_{3p}(z)=\frac{451.1z^3-1340z^2+1327z+437.8}{z^4-1.045z^3-0.2556z^2+0.8711z-0.5366}$$

The chirp signal from 0.01 to 1 Hz with 1 V amplitude was applied as an input voltage signal. The matching percentages of the measured position outputs with the BJ models are 88.49%, 87.39%, and 74.11%. Based on these models, the position controllers in (6-5) were calculated by the same procedures as shown in Section 6.2.

$$C_{1p}(z)=\frac{0.00057z+0.001049}{z-1}$$

$$C_{2p}(z)=\frac{0.001114z+0.00205}{z-1} \quad (6\text{-}5)$$

$$C_{3p}(z)=\frac{0.0009667z+0.001779}{z-1}$$

A 0.2-g lead mass was used as the object to be held by the three-finger gripper. This lead mass was supported by the flexible clamp initially as shown in Fig. 6-14. Fig. 6-14 shows the gripper was initialized in the first 20 s, which was required to regulate the position to be zero. After that, control voltages generated the movement of the gripper to follow the first commanded step at t = 20 s for a smooth approach before grabbing the object shown in Fig 6-15. The third step as shown in Fig. 6-16 depicts the grabbing stage which was continued from 20 s to 40 s. The last step motion at 40 s was generated to release the object.

Fig. 6-14. First step of the pick-hold-drop operation.

Three-finger gripper gives more flexibility to the design compared with two-finger gripper. Since three-finger gripper moves independently, the grasping configuration may be any triangle with vertices on the approach trajectory segments. This

flexibility allows to grasp irregular objects, even if not positioned in a central configuration with respect to the workspace of the gripper itself.

Fig. 6-15. Second step of the pick-hold-drop operation.

Fig. 6-16. Third step of the pick-hold-drop operation.

CHAPTER VII

CONCLUSIONS AND SUGGESTIONS FOR FUTURE WORK

This chapter describes the achievements made in this research and suggests future work for the improvement of IPMC actuators.

7.1 Conclusions

Precision in macro- and micro-manipulation has become the key to the development of the next-generation technology. The demand of new type of actuators and sensors continuously increase for precision manipulation applications.

EAP and IPMC, in a cantilever configuration, can be modeled reasonably accurately using linear system identification approaches. Position and force feedback using laser distance sensors and precision load cell was used to identify the system model, and blocked force with a voltage input was used to manipulate three fingers of the gripper. In the process of experimentally identifying the model parameters and validating the model, it was observed that the EAP and the IPMC actuators behaved consistently below approximately 5 Hz.

An EAP actuator's dynamic behavior was discussed, and its system identification and precision control were performed by simulation and experimental implementation. The digital PID controller based on the identified model improved the system performance. The phase margin was 60° with a crossover frequency of 0.171 Hz. The proposed anti-windup scheme along with the controller proved that an excellent tracking performance could be achieved. The 0.8-mm and 50-μm step responses demonstrated significant improvements in transient dynamic behaviors. The settling time was reduced

by 0.18 s, the control voltage was reduced by 16.3%, and the percent overshoot decreased to 37.1%. Performance degradation due to actuator saturation could also be reduced significantly with an integrator anti-windup scheme.

A three-finger IPMC gripper's dynamic behavior was discussed. A linear model for the IPMC using a chirp signal with 1, 2, and 3 V amplitudes in the interesting frequency range of [0.01 Hz, 5 Hz] was identified. The Bode plots of the system transfer functions obtained from a PSD analysis and a BJ model matched well within the interesting frequency range. It was observed that the FFT magnitudes of the peak measured displacements obtained from the experimental outputs were linearly decreased by about 0.0035 mm-s with respect to decreasing the voltage amplitude by 1 V from 3 V.

A classical PID controller and a modified LQR controller to enhance the system dynamics and their transient-response performance were designed, implemented, and verified by simulation and experiment. In an experimental case of a 1-mm step response in the closed-loop system, the maximum overshoot was reduced from 14.06% to 1.96% without increasing the settling time using a modified LQR controller compared with the performance using a PID controller. The accomplished zero steady-state error was crucial to manipulate the IPMC actuator effectively in 'pick-and-place' operations.

7.2 Suggestions for Future Work

The research reported in this document represents significant advancements in the areas of modeling and characterization of IPMC material. Currently many researchers involved in EAP or IPMC applications, and several issues deserve further investigation. Some suggestions for future work are listed below.

- Modeling Part — Analytical modeling of IPMC, still requires a unified governing equation like that for piezoelectric material [69–71]. The non-linear behavior of IPMC should be addressed with a nonlinear modeling method, i.e., NARMAX (Nonlinear AutoRegressive Moving Average model with eXogeneous inputs) method.

- Enhanced Fabrication — IPMC is fully dependent upon the water, therefore new type of IPMC, i.e., encapsulated IPMC should be investigated for reducing any limitations occurring from the environmental condition. Design of the end-effector or micro-tips will be helpful to manipulate the gripper. This is critical for 'pick-and-place' operation. The gripper can be made a modular, which can be easily interfaced with other manipulation systems.

- Control Part — Feedback control systems based on nonlinear or adaptive control strategies might help to manipulate the gripper. Small gain theorem would also help to find out the robustness of the system for the input since the modeling has uncertainties. Gain scheduling would handle the non-linear behavior of IPMC or EAP better.

- Microscale Force Analysis — An analysis of adhesion forces (Val der Waals force, electrostatic force, and surface tension force) is also required to manipulate microscale objects properly.

- Unified System — After identifying a reliable process technique including the modeling and the controller is fully developed, no uses of the position and the force sensors are desirable as a module with a portable battery or a fuel cell.

REFERENCES

[1] M. Sadeghipour, R. Salomon, and S. Neogi, "Development of a novel electrochemically active membrane and 'smart' material based vibration sensor/damper," *Smart Materials and Structures*, vol. 1, no. 1, pp. 172–179, May 1992.

[2] M. Shahinpoor, "Conceptual design, kinematics and dynamics of swimming robotic structures using ionic polymer gel muscles," *Smart Materials and Structures*, vol. 1, no. 1, pp. 91–94, May 1992.

[3] K. Oguru, Y. Kawami, and H. Takenaka, "Bending of an ion-conducing polymer film-electrode composite by an electric stimulus at low voltage," *Trans. Journal of Micromachine Society*, vol. 5, pp. 27–30, September 1992.

[4] S. Tadokoro, S. Yamagami, T. Takamori, and K. Oguro, "Modeling of Nafion-Pt composite actuators (ICPF) by ionic motion," in *Proceedings of SPIE*, *Smart Structures and Materials*, vol. 3987, pp. 92–102, March 2000.

[5] Y. Bar-Cohen, S. Sherrit, and S. Lih, "Characterization of the electromechanical properties of EAP materials," in *Proceedings of EAPAD, SPIE's 8th Annual International Symposium on Smart Structures and Materials*, pp. 4326–4343, March 2001.

[6] R. Kanno, S. Tadokoro, M. Hattori, T. Takamori, M. Costaftis, and K. Oguro, "Dynamic model of ICPF (Ionic Conducting Polymer Film) actuator," in *Proceedings of IEEE International Conference on Systems, Man, and*

Cybernetics: Intelligent Systems for the 21st Century, vol. 1, pp. 177–182, October 1995.

[7] R. Kanno, S. Tadokoro, M. Hattori, T. Takamori, M. Costaftis, and K. Oguro, "Modeling of ICPF (Ionic Conducting Polymer Film) actuator," in *Proceedings of the 1995 IEEE 21st International Conference on Industrial Electronics, Control, and Instrumentation*, vol. 2, pp. 913–918, November 1995.

[8] R. Kanno, S. Tadokoro, and T. Takamori, "Linear approximate dynamic model of ICPF," in *Proceedings of the IEEE International Conference on Robotics and Automation*, vol. 1, pp. 219–225, April 1996.

[9] N. Bhat and W. -J. Kim, "Precision force and position control of ionic polymer metal composite," *Journal of Systems and Control Engineering*, vol. 218, no. 6, pp. 421–432, June 2004.

[10] N. Bhat, *Modeling and Precision Control of Ionic Polymer Metal Composite*, Master's Thesis, Texas A&M University, August 2003.

[11] N. Bhat and W. -J. Kim, "System identification and control of ionic polymer metal composite," in *Proceedings of SPIE*, *Smart Structures and Materials*, vol. 5049, pp. 526–535, March 2003.

[12] K. Newbury and D. J. Leo, "Modeling of electromechanical transduction in ionic polymer materials," in *Proceedings of ASME International Mechanical Engineering Congress & Exposition*, pp. 47–57, November 2002.

[13] K. Mallavarapu and D. J. Leo, "Feedback control of the bending response of ionic polymer actuators," *Journal of Intelligent Material Systems and Structures*, vol. 12, no. 03, pp. 143–155, March 2001.

[14] R. J. Alvarez and M. Shahinpoor, "Simulation and control of iono-elastic beam dynamic deflection model," in *Proceedings of SPIE, Smart Structure and Material: EAPAD*, vol. 4695, pp. 335–344, March 2002.

[15] *Biomimetic Products Datasheet*, Sterling, VA, Biomimetic Products Inc., 2002

[16] R. C. Richardson, M. C. Levesley, M. D. Brown, J. A. Hawkes, K. Watterson, and P. G. Walker, "Control of ionic polymer metal composites," *IEEE/ASME Transactions of Mechatronics*, vol. 8, no. 2, pp. 245–253, June 2003.

[17] Y. Bar-Cohen, *Electroactive Polymer (EAP) Actuators as Artificial Muscles*, 2nd Edition, Bellingham, WA, SPIE Press, 2001.

[18] Y. Bar-Cohen and S. Leary, "Electroactive Polymer (EAP) Characterization Methods," in *Proceedings of SPIE*, *Smart Structures and Materials*, 2000, vol. 3987, pp. 12–16, March 2000.

[19] R. Lumia and M. Shahinpoor, "Microgripper design using electro-active polymers," in *Proceedings of SPIE*, *Smart Structures and Materials*, vol. 3669, pp. 322–329, May 1999.

[20] J. Su, C. Robert, J. Harrison, K. M. Newbury, and D. J. Leo, "Performance evaluation of bending actuators made from electrostrictive graft elastomers," in *Proceedings of SPIE*, *Smart Structures and Materials*, vol. 4695, pp. 104–110, July 2002.

[21] A. D. Dimarogonas and S. D. Haddad, *Vibration for Engineers*, Englewood Cliffs, NJ, Prentice Hall, 1992.

[22] S. Nemat-Nasser and J. Y. Li, "Electromechanical response of ionic polymer metal Composites," *Journal of Applied Physics*, vol. 87, pp. 3321–3331, April 2000.

[23] S. Tadokoro, M. Fujuhara, and Y. Bar-Cohen, "A CAE approach in application of Nafion-Pt Composite (IPCF) actuators – Analysis for surface wipers of NASA MUSES-CN nanorovers," in *Proceedings of SPIE*, *Smart Structures and Materials*, vol. 3987, pp. 262–272, March 2000.

[24] X. Bao, Y. Bar-Cohen, and S. –S. Lih, "Measurement and macro models of ionomeric polymer-metal composites (IPMC)," in *Proceedings of SPIE*, *Smart Structures and Materials*, vol. 4695, pp. 220–227, July 2002.

[25] K. M. Jung and S. M. Ryew, "Experimental investigations on behavior of IPMC polymer actuator and artificial muscle-like linear actuator," in *Proceedings of SPIE*, *Smart Structures and Materials*, vol. 4329, pp. 449–457, March 2001.

[26] K. Mallavarapu, K. M. Newbury, and D. J. Leo, "Feedback control of the bending response of ionic polymer-metal composite actuator," in *Proceedings of SPIE*, *Smart Structures and Materials*, vol. 4329, pp. 301–310, March 2001.

[27] C. S. Kothera, *Micro-Manipulation and Bandwidth Characterization of Ionic Polymer Actuator*, Master's Thesis, Virginia Polytechnic Institute and State University, December 2002.

[28] Y. Bar-Cohen, "Electroactive polymer as artificial muscles – reality and challenges," in *Proceedings of the 42nd AIAA*, *Structure Dynamics and Materials*, vol. 1492, pp. 1–9, April 1992.

[29] S. Nemat-Nasser and J. Li, "Electromechanical response of ionic polymer-metal composites," *Journal of Applied Physics*, vol. 87, no. 7, pp. 3321−3331, April 2000.

[30] R. Kanno, A. Kurata, M. Hattori, S. Tadokoro, T. Takamori, and K. Oguro, "Characteristics and modeling of ICPF actuator," in *Proceedings of Japan-USA Symposium on Flexible Automation*, vol. 2, pp. 691−698, July 1994.

[31] M. Shahinpoor and K. J. Kim, "Ionic polymer-metal composite: I. Fundamentals," *Smart Materials and Structures*, vol. 10, no. 4, pp. 819–833, Aug. 2001.

[32] D. Ewins, *Modal Testing: Theory and Practice*, Hertfordshire, England, Brüel & Kjær, 1986.

[33] Center of Excellence for Advanced Materials group UCSD website. "Key Attributes of Living Organisms" [Online]. Available: http://www-ceam.ucsd.edu/ipmc/sld001.htm, (accessed on November 20, 2005).

[34] Y. Bar-Cohen, "Transition of EAP material from novelty to practice applications – Are we there yet?," in *Proceedings of SPIE Symposium*, *Smart Structures and Materials*, vol. 4329, pp. 1–9, March 2001.

[35] I. W. Hunter and S. Lafontaine, "A Comparison of muscle with artificial actuators," in *5th Technical Digest., IEEE Solid-State Sensor and Actuator Workshop*, pp. 178–185, June 1992.

[36] R. Kornbluh, R. Pelrine, Q. Pei, S. Oh, and J. Joseph, "Ultrahigh strain response of field-actuated elastomeric polymers," in *Proceedings of SPIE Symposium*, *Smart Structures and Materials*, vol. 3987, pp. 51–64, March 2000.

[37] R. Pelrine, P. Sommer-larsen, R. Kornbluh, R. Heydt, G. Kofod, and Q. Pei, "Applications of dielectric elastomer actuators," in *Proceedings of SPIE Symposium*, *Smart Structures and Materials*, vol. 4329, pp. 335–349, March 2001.

[38] Y. Bar-Cohen, S. Leary, A. Yavrouian, K. Oguro, S. Tadokoro, J. Harrison, J. Smith, and J. Su, "Challenges to the application of IPMC as actuators of planetary mechanisms," in *Proceedings of SPIE Symposium*, *Smart Structures and Materials*, vol. 3987, pp. 140–146, March 2000.

[39] R. Lumia and M. Shahinpoor, "Microgripper design using electro-active polymers," in *Proceedings of SPIE Symposium*, *Smart Structures and Materials*, vol. 3669, pp. 322–329, March 1999.

[40] D. Hanson, G. Pioggia, Y. Bar-cohen, and D. D. Rossi, "Androids: Application of EAP as artificial muscles to entertainment industry," in *Proceedings of SPIE Symposium*, *Smart Structures and Materials*, vol. 4329, pp. 375–379, March 2001.

[41] S. Guo, K. Sugimoto, S. Hata, J. Su, and K. Oguro, "A new type of underwater fish-like microrobot", in *Proceedings of the 2000 IEEE/RSJ International Conference on Intelligent Robots and Systems*, vol. 2, pp. 867−872, October 2000.

[42] S. Guo, T. Fukuda, K. Kosuge, F. Arai, K. Oguro, and M. Negoro, "Micro catheter system with active guide wire", in *Proceedings of the 1995 International Conference on Robotics and Automation*, vol. 1, pp. 79−84, October 1995.

[43] S. Guo, T. Fukuda, K. Kosuge, F. Arai, K. Oguro, and M. Negoro, "Micro catheter system with active guide wire - structure, experimental results and

characteristic equation of active guide wire catheter using ICPF actuator," in *Proceedings of the 1994 5th International Symposium on Micro Machine and Human Science*, pp. 191−197, October 1994.

[44] K. Onishi, S. Sewa, K. Asaka, N. Fujiwara, and K. Oguro, "Biomimetic micro actuators based on polymer electrolyte / gold composite driven by low voltage", in *Proceedings of 13th Annual International Conference on Robotics and Automation*, pp. 386−390, January 2000.

[45] S. Sewa, K. Onishi, K. Asaka, N. Fujiwara, and K. Oguro, "Polymer actuator briven by ion current at low voltage, applied to catheter system", in *Proceedings of the 1998 Micro Electro Mechanical Systems Robotics and Automation*, pp. 148−153, January 1998.

[46] M. Shahinpoor and K. J. Kim, "Design, development and testing of a multi-fingered heart compression / assist device equipped with IPMC artificial muscles", in *Proceedings of SPIE Symposium*, *Smart Structures and Materials*, vol. 4329, pp. 411−420, March 2001.

[47] A. Keshavarzi, M. Shahinpoor, K. J. Kim, and J. Lantz, "Blood pressure, pulse rate, and rhythm measurement using ionic polymer metal composite sensors", in *Proceedings of SPIE Symposium*, *Smart Structures and Materials*, vol. 3669, pp. 369−376, March 1999.

[48] M. Konyo, S. Tadokoro, T. Takamori, and K. Oguro, "EAP application to artificial tactile fell display of virtual reality," in *Proceedings of SPIE Symposium*, *Smart Structures and Materials*, vol. 4329, pp. 389−400, March 2001.

[49] S. Lee, K. J. Kim, and H. C. Park, "Design and performance analysis of a novel IPMC-driven micropump," in *Proceedings of SPIE Symposium*, *Smart Structures and Materials*, vol. 5759, pp. 439−446, March 2005.

[50] S.Guo, T. Nakamura, T. Fukuda, and K. Oguro, "Development of the micro pump using ICPF actuator", in *Proceedings of the 1997 International Conference on Robotics and Automation*, vol. 1, pp. 266−271, April 1997.

[51] S. Guo, S. Hata, K. Sugumoto, T. Fukuda, and K. Oguro, "Development of a new type of capsule micropump", in *Proceedings of the 1999 International Conference on Robotics and Automation*, vol. 1, pp. 2171−2176, May 1999.

[52] S. Hattori, T. Fukuda, R. Kishi, H. Ichijo, Y. Katsurayama, H. Katayama, H. Matsuura, T. Watarai, S. Nagamori, and T. Hiramatsu, "Structure and mechanism of two types of micro-pump using polymer gel", in *Proceedings of the 1992 Micro Electro Mechanical Systems*, pp. 110−115, February 1992.

[53] K. J. Kim, M. Shahinpoor, and A. Razani, "Preparation of IPMC for use in fuel cells, electrolysis, and hydrogen sensors," in *Proceedings of SPIE Symposium*, *Smart Structures and Materials*, vol. 3987, pp. 311−320, March 2000.

[54] Baumer Electric, *Measuring at an Angle with the OADM20I44xx and OADM20I45xx*, Soutington, CT, 2003.

[55] L. Ljung, *System Identification*: *Theory for the User*, 2nd Edition, Upper Saddle River, NJ, Prentice Hall, 1999.

[56] *System Identification Toolbox*. Natick, MA, The Mathworks, Inc., 2005.

[57] T. Söderström, P. Stoica, *System Identification*, Englewood Cliffs, NJ, Prentice Hall, 1989.

[58] G. Tao and P. A. Ioannou, "Persistency of excitation and overparameterization in model reference adaptive control," in *Proceeding of the 27th Conference on Decision and Control*, pp. 757–758, December 1988.

[59] C. Harris, *Shock and Vibration Handbook*, New York, NY, McGraw-Hill, 1995.

[60] J. W. Paquette, K. J. Kim, J.-D. Nam and Y. S. Tak, "An equivalent circuit model for ionic polymer – Metal composites and their performance improvement by a clay-based polymer nano-composite technique," *Journal of Intelligent Material Systems and Structures*, vol. 14, pp. 633–641, October 2003.

[61] C. S. Kothera, S. L. Lacy, R. S. Erwin, and D. J. Leo, "Nonlinear identification of ionic polymer actuator systems," in *Proceedings of SPIE, Smart Structures and Material*, vol. 5383, pp. 144–154, March 2004.

[62] N. Bhat and W. -J. Kim, "System identification and control of ionic polymer metal composite," in *Proceedings of SPIE*, *Smart Structures and Materials*, vol. 5049, pp. 526–535, March 2003.

[63] K. Yun and W. -J. Kim, "Microscale position control of electroactive polymer using anti-windup scheme," revised and resubmitted to *Smart Materials and Structures*, October 2004.

[64] A. Gelb, *Applied Optimal Estimation*, Cambridge, MA, The M.I.T. Press, 1974.

[65] G. F. Franklin, J. D. Powell, and A. Emami-Naeini, *Feedback Control of Dynamic Systems*, 4th Edition, Upper Saddle River, NJ, Prentice Hall, 2002.

[66] *Simulink Response Optimization Toolbox*, Natick, MA, The Mathworks, Inc., 2005.

[67] S. P. Bhattacharyya, H. Chapellat, and L. H. Keel, *Robust Control: The Parametric Approach*, Upper Saddle River, NJ, Prentice Hall, 1995.

[68] M. Gopal, *Digital Control and State Variable Methods*, New Delhi, India, Tata McGraw-Hill, 2003.

[69] E. F. Crawley and J. de Luis, "Use of Piezo-ceramics as distributed actuators in large space structures," in *Proceeding of the 26th Structures, Structural Dynamics, and Materials*, vol. 626, pp. 126–133, April 1985.

[70] W. –S. Hwang and H. Park, "Finite element modeling of piezoelectric sensors and actuators," *Journal of American Institute of Aeronautics and Astronautics*, vol. 31, pp. 930–937, May 1993.

[71] B. T. Wang and C. A. Rogers, "Modeling of finite-length spatially-distributed induced strain actuators for laminate beams and plates," *Journal of Intelligent Material Systems and Structures*, vol. 2, pp. 38–58, January 1991.

APPENDIX A

SIMULINK® CODES

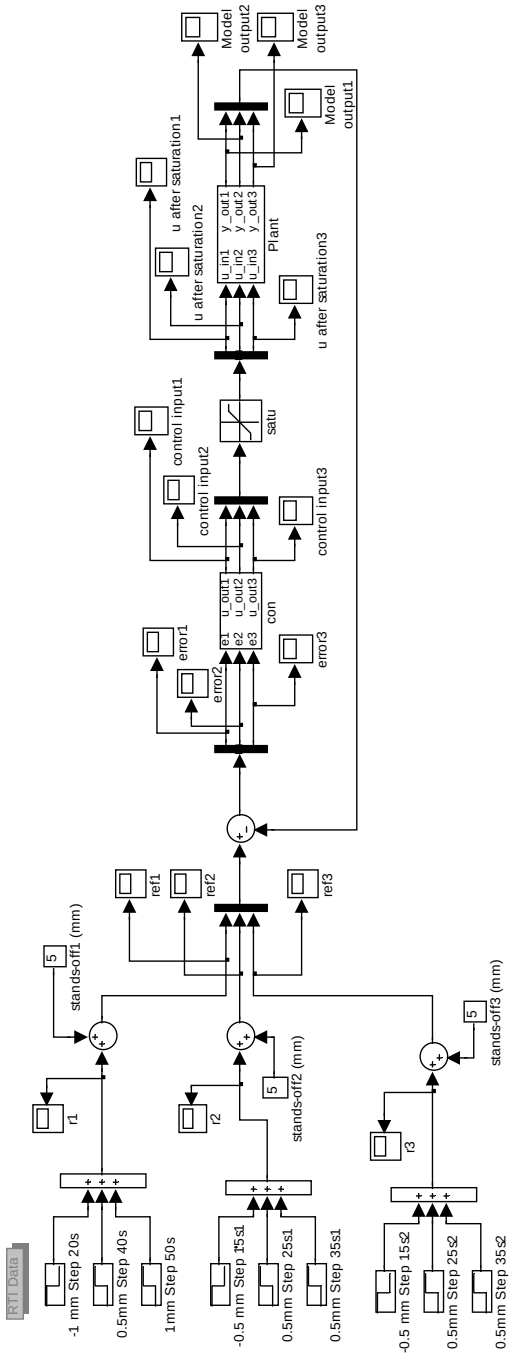

Fig. A-1. The Simulink® block diagram for real-time position control in three-finger gripper motion.

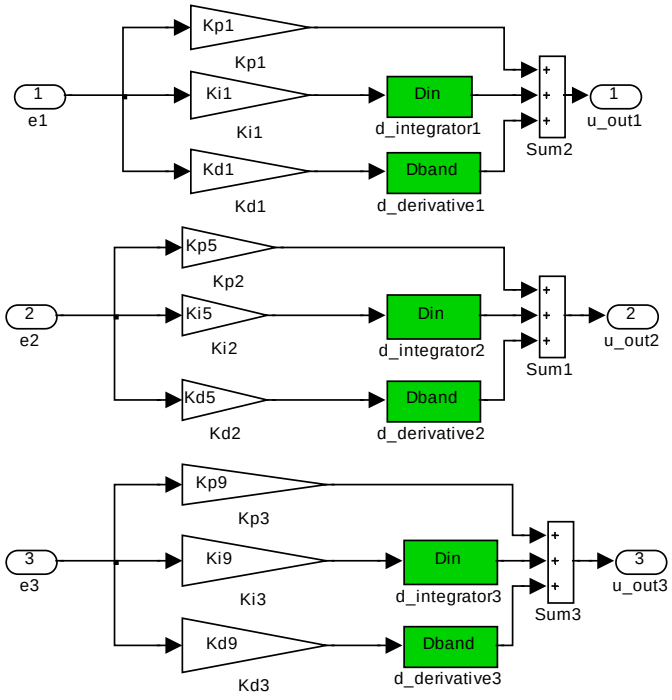

Fig. A-2. A detailed diagram of PID controller.

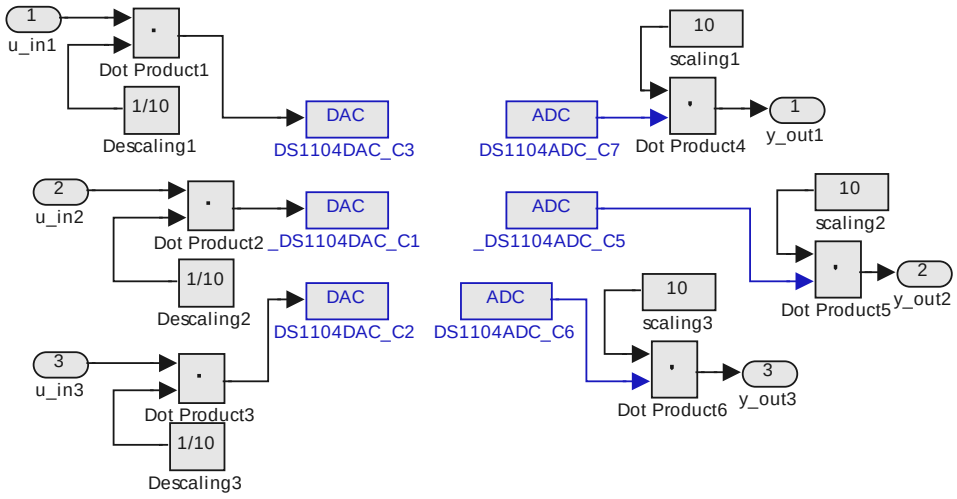

Fig. A-3. Schematic I/O connections for the three-finger plant.

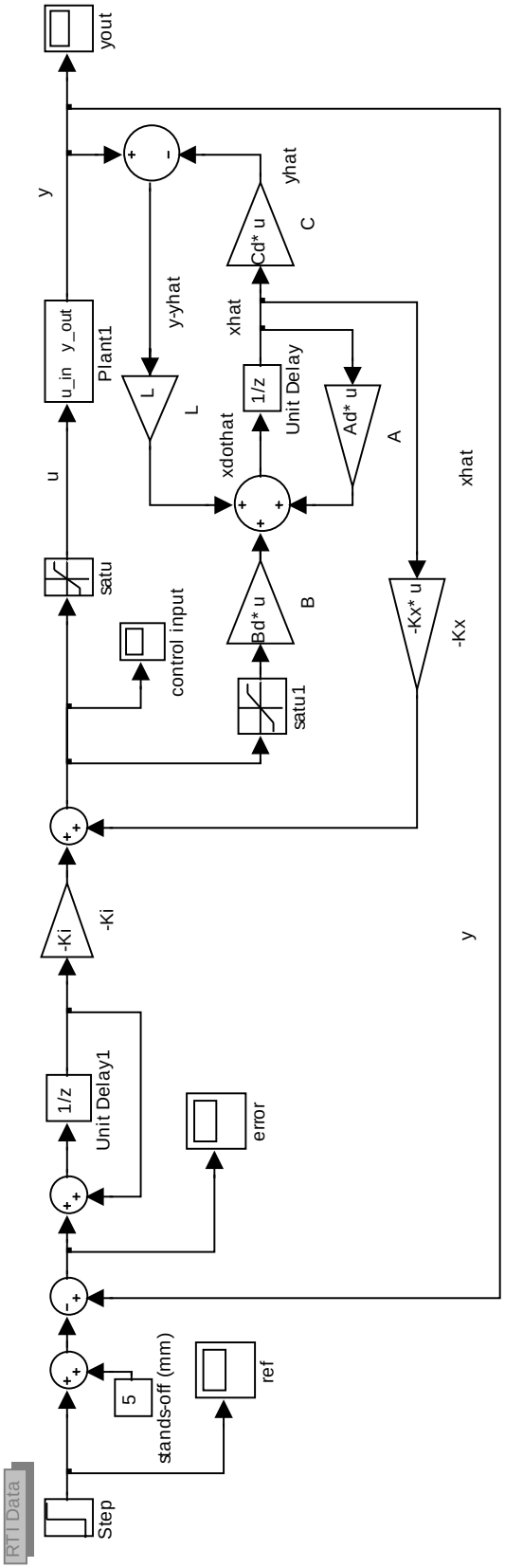

Fig. A-4. The Simulink® block diagram for LQR with the observer.

APPENDIX B

MATLAB® CODES

```
%STEPSPECS System Step Response Specifications.
function [os,ts,tr]=stepspecs(t,y,yss,sp)
% [OS,Ts,Tr]=STEPSPECS(T,Y,Yss,Sp) returns the percent overshoot OS,
% settling time Ts, and rise time Tr from the step response data contained
% in T and Y.
% Y is a vector containing the system response at the associated time
% points in the vector T. Yss is the steady state or final value of the
% response.
% If Yss is not given, Yss=Y(end) is assumed. Sp is the settling time
% percentage.
% If Sp is not given, Sp = 2% is assumed. The settling time is the time it
% takes the response to converge within +-Sp percent of Yss.
% The rise time is assumed to be the time for the response to initially
% travel from 10% to 90% of the final value Yss.
%------------------------------------------------------------------------
if nargin<2
  error('At Least Two Input Arguments are Required.')
end
if numel(t)~=length(t) || numel(y)~=length(y)
  error('T and Y Must be Vectors.')
```

```
end
if nargin==2
  yss=y(end);   sp=2;
elseif nargin==3
  sp=2;
end
if isempty(yss)
  yss=y(end);
end
if yss==0,   error('Yss Must be Nonzero.')
end
if yss<0 % handle case where step response may be negative
  y=-y;   yss=-yss;
end
t=t(:);   y=y(:);
% find rise time using linear interpolation
idx1=find(y>=yss/10,1);
idx2=find(y>=9*yss/10,1);
if isempty(idx1) || idx1==1 || isempty(idx2)
  error('Not Enough Data to Find Rise Time.')
end
alpha=(yss/10-y(idx1-1))/(y(idx1)-y(idx1-1));
t1=t(idx1-1)+alpha*(t(idx1)-t(idx1-1));
```

```
alpha=(9*yss/10-y(idx2-1))/(y(idx2)-y(idx2-1));
t2=t(idx2-1)+alpha*(t(idx2)-t(idx2-1));
tr=t2-t1;

% find settling time using linear interpolation
idx1=find(abs(y-yss)>abs(yss*sp/100),1,'last');
if isempty(idx1) || idx1(1)==length(y)
  error('Not Enough Data to Find Settling Time.')
end
if y(idx1)>yss
  alpha=(y(idx1)-(1+sp/100)*yss)/(y(idx1)-y(idx1+1));
  ts=t(idx1)+alpha*(t(idx1+1)-t(idx1));
else
  alpha=((1-sp/100)*yss-y(idx1))/(y(idx1+1)-y(idx1));
  ts=t(idx1)+alpha*(t(idx1+1)-t(idx1));
end
% find percent overshoot based on peak data value
os=max(0,(max(y)-yss)/yss)*100;
```

```
% LQR with Observer
clear all;close all;clc;
format short g;
% plant model  (Gtf5_0c    1 Hz )
n1=[0       97.931        93870  8.6441e+006  1.6758e+008];
d1=[1       887.96  3.5973e+005  2.4088e+008   4.677e+008];
sys1=tf(n1,d1);z1=zero(sys1);p1=pole(sys1);dcgain(sys1);
Ts=0.004;sysd=c2d(sys1,Ts);
[Ad,Bd,Cd,Dd]=ssdata(sysd);
% plant model with integral state
Ai=[Ad(1,:) 0;Ad(2,:) 0;Ad(3,:) 0;Ad(4,:) 0;Cd*Ad 1];
Bi=[Bd(1);Bd(2);Bd(3);Bd(4);Cd*Bd];
Ci=[Cd 0];
cu=ctrb(Ai,Bi);rankcu=rank(cu)

q=linspace(1e-3,1e+3,5);color='bgrcm';
for i=1:5,
   R=1;
   Q=q(i)*eye(5);   % define weights
   [K,P,E]=dlqr(Ai,Bi,Q,R);   % compute LQR gain, r is fixed.
   cle(:,i)=E;  % cle=E_cl
   k(i,:)=K;        % row order
   Kx=K(1:length(K)-1);Ki=K(5);
```

```
Ai_CL=Ai-Bi*K;
sysCL=ss(Ai_CL,[0;0;0;0;-1],Ci,0,'Ts',Ts);
t=[0:Ts:40-Ts];
[y,t,x]=step(sysCL,t);yq(:,i)=y;

% select observer poles to be 10 times faster than controller
desiredpoles=E(1:length(Kx))';
%desiredpoles=eig(Ad-Bd*Kxq)';
dp_q(i,:)=desiredpoles;   % column order
observerpoles=0.1*desiredpoles;  obvp_q(i,:)=observerpoles;  % column order
% compute observer gain L
L=acker(Ad',Cd',observerpoles);    Lq(i,:)=L;

%    [OSq,Tsq,Trq]=stepspecs(t,yq(:,i));
%    Mpq(i)=OSq; trq(i)=Trq; tsq(i)=Tsq;
%    specs_q=[Mpq' trq' tsq'];
figure(1),
subplot(211),plot(t,yq(:,i),color(i));set(gca,'fontsize',12);
title('The closed-loop step response');ylabel('displacement (mm)');
legend('q=100','q=200','q=300','q=400','q=500','Location','SouthEast');hold on;
control_inputq=-(Kx*x(:,1:4)'+Ki*x(:,5)')';
ci_q(:,i)=control_inputq;
subplot(212),plot(t,ci_q(:,i),color(i));set(gca,'fontsize',12);
```

```
   title('The control input');xlabel('time (t)');ylabel('voltage (V)');
   legend('q=100','q=200','q=300','q=400','q=500');hold on;
end


K1=k(1,:);
Kx=K1(1:4)
Ki=K1(5)
%--------------------------------------------------------------------------
format long g
load ipmc5_0_0501
% Take the data
time =  ipmc5_0_0501.X.Data;                % Change
tnew=time(790:53.16/Ts)-time(790);
% output
y3=double(ipmc5_0_0501.Y(3).Data);          % experiment
yout=y3(790:53.16/Ts);                      % rearrange
%ymean=mean(yout(1250:10/Ts));
yout=yout-5;
t0=0:Ts:10-Ts;t0=t0';
t1=t+10;
t2=[t0; t1];
yq0=zeros(10/Ts,1);
yq=[yq0;yq(:,1)];
```

```
figure(2),
%subplot(211),plot(t,yq(:,1),tnew,yout);set(gca,'fontsize',12);
subplot(211),plot(tnew,yout,'b',t2,yq,'r');set(gca,'fontsize',12);
title('The closed-loop step response');ylabel('displacement (mm)');
%legend('q=100, simulation','Location','SouthEast');hold on;
% control input
y1 =double(ipmc5_0_0501.Y(1).Data);            % experiment
cinew=y1(790:53.16/Ts);                        % rearrange
control_in=zeros(10/Ts,1);                     % simulation
control_inputq=-(Kx*x(:,1:4)'+Ki*x(:,5)')';
ci_q=[control_in; control_inputq];
subplot(212),plot(tnew,cinew,'b',t2,ci_q,'r');set(gca,'fontsize',12);
title('The control input');xlabel('time (t)');ylabel('voltage (V)');
%legend('q=100, simulation');hold on;
% output
figure(3),plot(tnew-8,yout,'b',t2-8,yq,'r');set(gca,'fontsize',12);
xlabel('time (t)');xlim([0,10]);ylabel('displacement (mm)');
% control input
figure(4),plot(tnew-8,cinew,'b',t2-8,ci_q,'r');set(gca,'fontsize',12);
xlabel('time (t)');xlim([0,10]);ylabel('voltage (V)');ylim([-0.2,1.5]);
```

```
% system identification
load ipmc01_1vchirp5hz0830;    % 1V
font=14;
% change the voltage amplitude
Vmag1=1;    % 1 volt
%--------------------------------------------------------------------------
input1=double(eap07_chirp5hzdelay0112.Y(1).Data)';
output1=double(eap07_chirp5hzdelay0112.Y(2).Data)';
time1=eap07_chirp5hzdelay0112.X.Data';  % Change
chirp_input1=double(eap07_chirp5hzdelay0112.Y(3).Data)';
%--------------------------------------------------------------------------
Fs=1/eap07_chirp5hzdelay0112.X.Data(2)';
Fn=Fs/2;                    % Nyquist frequency
Ts=1/Fs;                    % sampling period
%--------------------------------------------------------------------------
i1=1:length(input1); i1=i1';
cu1=chirp_input1(i1);
u1=input1(i1);                  % input1
out1=output1(i1);                % measured output1
y1=-(out1-mean(out1(1:3/Ts)));
t1=time1(i1);                   % sampled time1 step
%--------------------------------------------------------------------------
% find out the exactly starting point of linear chirp signal
f_start=0.001;                % initial freq.
f_finish=5;                   % target freq.
```

```
T=40;                    % target time1
%-------------------------------------------------------------------------
t_final1=time1(length(t1));
tt1=0:Ts:t_final1;
beta=(f_finish-f_start)/T;            % the rate of freq. increase
%-------------------------------------------------------------------------
% % change the voltage amplitude
% Vmag1=1;    % 1 volt
%-------------------------------------------------------------------------
uu1=Vmag1*sin(2*pi*(f_start*tt1+beta/2*tt1.^2));
%-------------------------------------------------------------------------
% Find the actually applied time1 to DS1102
% delayed by step function
for m1=1:length(t1),
   limit=10e-5;
   if abs(u1(m1)-u1(m1+1))>limit,
  % if u1(1)-limit < uu1(m1) & uu1(m1) < u1(1)+limit,
disp('Magnitude of LCS at the right before applied step function');
       u_mag1=u1(m1)                % magnitude of LCS
       count1=m1                  %
disp('The time1 at the right before applied step function');
       tx1=(count1-1)*Ts              % actual time1 of LCS
disp('The starting frequency');
       fx1=f_finish-beta*(T-tx1)       % initial freq.
       ty1=T;                % defined target time1
disp('Target frequency at target time1');
```

```
        fy1=beta*(ty1-tx1)+fx1       % defined target freq.
        break
    end
end
% dSpace inherited delay in Simulink
for n1=1:4*Fs,
    limit=10e-5;
    if cu1(1)-limit < uu1(n1) & uu1(n1) < cu1(1)+limit,
disp('The intial magnitude of LCS from DS1102');
        ui_mag1=uu1(n1)                  % magnitude of LCS
        counti1=n1                       %
disp('Inherited time1 in DS1102 comparing to an ideal LCS');
        ttx1=counti1*Ts                  % inherited time1 from DS1102
        ffx1=f_finish-beta*(T-ttx1)              % inherited starting freq.of LCS
        tty1=T;                          % defined target time1
        ffy1=beta*(tty1-ttx1)+ffx1           % defined target freq.
        break
    end
end
tnew1=t1(tx1/Ts:length(t1))-(tx1+Ts);
unew1=u1(tx1/Ts:length(u1));
%-------------------------------------------------------------------------
% finding the starting point
for j1=1:length(u1);
    limit=10e-5;
    if  abs(u1(j1)-u1(j1+1))>limit;
```

```
        u_start1=u1(j1);
        k1=j1
        u_k1=u1(k1);
disp('The initial magnitude of applied LCS');
        u_k11=u1(k1+1)
        break
    end
end
%--------------------------------------------------------------------------
t_t1=tx1+ttx1;                  % totally compensated starting time1
% (dSpace inherited delay in Simulink + delayed by step function)
disp('The same as u_k1')
uu1(t_t1*Fs)
disp('The actual starting freq.');
f_x1=f_finish-beta*(T-t_t1)            % actual initial freq.
tty1=T;                         % defined target time1
f_y1=f_x1+beta*(tty1-t_t1)         % defined target freq.
%--------------------------------------------------------------------------
% input1 & output1
in_data1=input1(k1+1:40*Fs-counti1); out_data1=y1(k1+1:40*Fs-counti1);
t_data1=t1(k1+1:40*Fs-counti1)-t1(k1+1);
%--------------------------------------------------------------------------
figure(1),
plot(tnew1,unew1);set(gca,'fontsize',20);xlim([0 20]);
title('Chirp signal input with 1V amplitude','fontsize',font);
ylabel('voltage (V)');ylim([-1.1 1.1]);
```

```
set(gca,'Ytick',[-1 0 1]);set(gca,'Xtick',[0 10 20]);
%------------------------------------------------------------------------
% DFT of the signals
X1 = in_data1;
NFFT1=2.^(ceil(log(length(X1))/log(2)));     % Next highest power of 2 greater than length(X1) or equal to length(X1).
FFTX1=fft(X1,NFFT1);               % Take FFT, padding with zeros. length(FFTX1)==NFFT1
NumUniquePts1 = ceil((NFFT1+1)/2); % number of unique points
FFTX1=FFTX1(1:NumUniquePts1);      % FFT is symmetric, throw away second half
MX1=abs(FFTX1);                    % Take magnitude of X1
MX1=MX1*2;                         % Multiply by 2 to take into account the fact that we threw out second half of FFTX1 above
MX1(1)=MX1(1)/2;                   % Account for endpoint uniqueness
MX1(length(MX1))=MX1(length(MX1))/2; % We know NFFT1 is even
MX1=MX1/length(X1);                % Scale the FFT so that it is not a function of the length of X1.
f1=(0:NumUniquePts1-1)*2/NFFT1;        % This is an evenly spaced frequency vector with NumUniquePts1 points.
f1=f1*Fn;                          % Multiply this by the Nyquist frequency (Fn==1/s sample freq.)
%------------------------------------------------------------------------
figure(2),
plot(f1,MX1);set(gca,'fontsize',20);
title('FFT of linear chirp signals','fontsize',font);xlim([0.626 5]);
xlabel('frequency (Hz)');ylabel('magnitude (V-s)');
%------------------------------------------------------------------------
% Y1 = y1;
Y1=out_data1;
```

```
FFTY1=fft(Y1,NFFT1);              % Take FFT, padding with zeros. length(FFTY1)==NFFT1
FFTY1=FFTY1(1:NumUniquePts1);     % FFT is symmetric, throw away second half
MY1=abs(FFTY1);                   % Take magnitude of Y
MY1=MY1*2;      % Multiply by 2 to take into account the fact that we threw out second half of
FFTX1 above
MY1(1)=MY1(1)/2;                  % Account for endpoint uniqueness
MY1(length(MY1))=MY1(length(MY1))/2; % We know NFFT1 is even
MY1=MY1/length(Y1);               % Scale the FFT so that it is not a function of the length of x.
%-------------------------------------------------------------------------
figure(3),plot(f1,MY1);set(gca,'fontsize',font);xlim([0.626 5]);
title('FFT magnitudes of the measured outputs','fontsize',font);
xlabel('frequency (Hz)');ylabel('magnitude (mm-s)');
%-------------------------------------------------------------------------
% Power Spectrum Density1 analysis
N1 = NFFT1; % N = length(t1);
% The power spectrum, a measurement of the power at various frequencies,
Pxx1=MX1.*conj(MX1)/N1;
Pyy1=MY1.*conj(MY1)/N1;
Wxy1=sqrt(abs(Pyy1./Pxx1));
%-------------------------------------------------------------------------
% compare the power spectrum tf with the tf estimate
% Transfer Function Estimate
u1=X1;y1=Y1;
[txy1,fxy1]=tfe(u1,y1,2*length(X1),Fs,2*length(X1));
%-------------------------------------------------------------------------
% construct data sets
```

```
ksy1=iddata(out_data1,in_data1,Ts);
zm1=dtrend(ksy1);                % remove linear drift
%--------------------------------------------------------------------------
m34_1=bj(zm1,[4 4 4 4 1]);
B34_1=m34_1.b; C34_1=m34_1.c; D34_1=m34_1.d; F34_1=m34_1.f;
tfm34_1=tf(m34_1);
%--------------------------------------------------------------------------
figure(4),
subplot(313),plot(time1, input1);set(gca,'fontsize',font);xlim([0 10]);ylim([-1.1 1.1]);
title('The real applied chirp signal input (1 V)','fontsize',font);
xlabel('time (s)');ylabel('voltage (V)');
subplot(312),plot(time1, cu1);set(gca,'fontsize',font);xlim([0 10]);ylim([-1.1 1.1]);
title('The applied chirp signal input without adding the step input','fontsize',font);
ylabel('voltage (V)');
subplot(311),plot(tt1, uu1);set(gca,'fontsize',font);xlim([0 10]);ylim([-1.1 1.1]);
title('The theoretical chirp signal input','fontsize',font);
ylabel('voltage (V)');
%--------------------------------------------------------------------------
% k1*Ts is delayed by Step function
% counti1*Ts is delayed inherently by chirp signal Simulink compared w/ the original chirp
signal
% (counti1+k1+1)*Ts*beta is the real starting frequency
%--------------------------------------------------------------------------
figure(7),compare(zm1,m34_1);set(gca,'fontsize',font);
XT1=(40*Fs-counti1)*Ts-(k1+1)*Ts;  % time1 for the chirp signal range
title('BJ (1V)','fontsize',font);xlabel('time (s)');ylabel('output displacement (mm)');xlim([0 XT1]);
```

```
legend('measured output','BJ Fit: 34.32%');
%------------------------------------------------------------------------
% discrete system
Gd34_1s=minreal(tfm34_1(1));
[zd34_1s,pd34_1s,kd34_1s]=zpkdata(Gd34_1s,'v');

[numd34_1s,dend34_1s]=tfdata(Gd34_1s);
numd34_1s=numd34_1s{1};     % numerator
dend34_1s=dend34_1s{1};     % denominator

% continuous system tf and noise tf
Gc34_1s=d2c(Gd34_1s,'tustin');zc34_1s=zero(Gc34_1s);pc34_1s=pole(Gc34_1s);                %
continuous system tf
%  Gc34_1n=d2c(Gd34_1n,'tustin');zc34_1n=zero(Gc34_1n);pc34_1n=pole(Gc34_1n);          %
continuous noise tf
%------------------------------------------------------------------------
figure(10),
[mag34_1,phase34_1,w34_1]=dbode(numd34_1s,dend34_1s,Ts);                                 %
T=[mag34_1,phase34_1,w34_1];
semilogx(f1,20*log10(Wxy1(1:N1/2+1)),'b:',w34_1/(2*pi),20*log10(mag34_1),'k');
set(gca,'fontsize',font);xlim([0.626 5]);
title('Comparison of Bode plots of BJ method with PSD analysis','fontsize',font);
xlabel('frequency (Hz)');
ylabel('magnitude (dB)');legend('PSD TF (1V)','Bode (BJ)');
%------------------------------------------------------------------------
figure(11),
```

```
plot(f1,20*log10(Wxy1(1:N1/2+1)));
set(gca,'fontsize',font);xlim([0.626 5]);title('PSD TF','fontsize',font);
xlabel('frequency (Hz)');ylabel('magnitude (dB)');
%--------------------------------------------------------------------------
% DFT of the signals
% simulation output
[ysim1,tsim1]=lsim(Gd34_1s,in_data1,t_data1);
FFTYsim1=fft(ysim1,NFFT1);                    % Take FFT, padding with zeros. length(FFTYsim)==NFFT
FFTYsim1=FFTYsim1(1:NumUniquePts1);       % FFT is symmetric, throw away second half
MYsim1=abs(FFTYsim1);                  % Take magnitude of Ysim
MYsim1=MYsim1*2;      % Multiply by 2 to take into account the fact that we threw out second half of FFTX above
MYsim1(1)=MYsim1(1)/2;                 % Account for endpoint uniqueness
MYsim1(length(MYsim1))=MYsim1(length(MYsim1))/2; % We know NFFT is even
MYsim1=MYsim1/length(ysim1);                % Scale the FFT so that it is not a function of the length of x.
%--------------------------------------------------------------------------
figure(14),
plot(f1,MYsim1,'b:',f1,MY1,'r-.');set(gca,'fontsize',font);
title('The comparison of the experimental results to the simulated results in the frequecy domain','fontsize',font);
xlabel('frequency (Hz)');ylabel('magnitude (mm-s)');xlim([0.626 5]);
%set(gca,'fontsize',12);
legend('1V simulated output (BJ)','1V experimental output');
% set(gca,'fontsize',20);
```

```
% set(gca,'Xtick',[0 0.1 0.2 0.3 0.4 0.5 0.6 0.7 0.8 0.9 1]);


figure(15),
error1=abs(MY1-MYsim1);
plot(f1,error1);set(gca,'fontsize',font);
title('Errors','fontsize',font);xlabel('frequency (Hz)');ylabel('magnitude (mm-s)');
xlim([0.626 5]);%ylim([-0.01 0.2]);



% Design the position controller
clear all;close all;clc;
% format long e;
Ts=0.004;
z=tf('z',Ts);
Cz=pid
Lz=Cz*Pz
Lz=minreal(Lz,0.001)
w={0.01,10}
[mag,phase,w]=bode(Lz);
% 1st method with the margin command
kc=margin(mag,phase-60,w)
[numz,denz]=tfdata(Lz,'v')
[mag,phase,w]=dbode(numz,denz,Ts,w)
% 2nd method with a table
T=[mag,phase,w/(2*pi)]
%
```

```
kc
% Removing the disturbance effect
Cz=kc*pid;      % bode1_ipmc01%
% Cz=(25/15)*kc*pid     % bode2_ipmc01
Cz=minreal(Cz)
Lz=Cz*Pz
Lz=minreal(Lz)

% figure(1),margin(Lz)
% figure(2),bode(Lz_cl)
% [numz_cl,denz_cl]=tfdata(Lz_cl,'v')
% [mag_cl,phase_cl,w_cl]=dbode(numz_cl,denz_cl,Ts,w);
% T_cl=[mag_cl,phase_cl,w_cl]

Lz_cl=feedback(Lz,1,-1);
pole_Lz_cl=pole(Lz_cl);zero_Lz_cl=zero(Lz_cl);
Pc=minreal(d2c(Pz,'zoh'));
pole_Pc=pole(Pc);zero_Pc=zero(Pc);
Cc=minreal(d2c(Cz,'zoh'));
pole_Cc=pole(Cc);zero_Cc=zero(Cc);
Lc=minreal(d2c(Lz,'zoh'));
pole_Lc=pole(Lc);zero_Lc=zero(Lc);

w_Lc=linspace(0.01,10,100)
[mag_Lc,phase_Lc]=bode(Lc,w_Lc);
newphase=squeeze(phase_Lc)-360;
```

```
% figure(3),
% subplot(211),semilogx(squeeze(w_Lc),20*log10(squeeze(mag_Lc)));
% xlim([0.1 10]);ylim([-40 20]);
% subplot(212),semilogx(squeeze(w_Lc),newphase+720);
% xlim([0.1 10]);ylim([170 280]);
figure(2),margin(Lc)

Lc_cl=feedback(Lc,1,-1);        % closed-loop tranfer function
pole_Lc_cl=pole(Lc_cl);zero_Lc_cl=zero(Lc_cl);
w_range=logspace(-1,1);
figure(3),bodemag(Lc_cl,w_range)

[mag_cl,phase_cl,w_cl]=bode(Lc_cl);
format short g;
% T_cl=[squeeze(mag_cl),squeeze(phase_cl),squeeze(w_cl)]
T_cl=[squeeze(mag_cl),squeeze(w_cl)]
% 0.70174       1.3524                  % 0.7095       1.2187
% Wbw=1.3524                                %rad/sec
% fbw=Wbw/(2*pi) %= 0.21524                          %=0.19396

figure(4),step(Lz_cl)
[yout,tout]=step(Lz_cl);
figure(3),plot(tout,yout)
```

VITA

Name	Kwan Soo Yun
Address	Department of Mechanical Engineering, Mailstop 3123, Texas A&M University, College Station, TX 77843-3123
Email	yunkwansoo@tamu.edu
Education	B.S., Mechanical Engineering A-jou University, Suwon, Korea, February 1999 M.S., Mechanical Engineering Texas A&M University, College Station, May 2002

The typist for this dissertation was Kwan Soo Yun.